A new coupled modelling framework for turbine inflow generation: mesoscale-synthetic turbulence

Adithya Vemuri

Technische Universiteit Delft

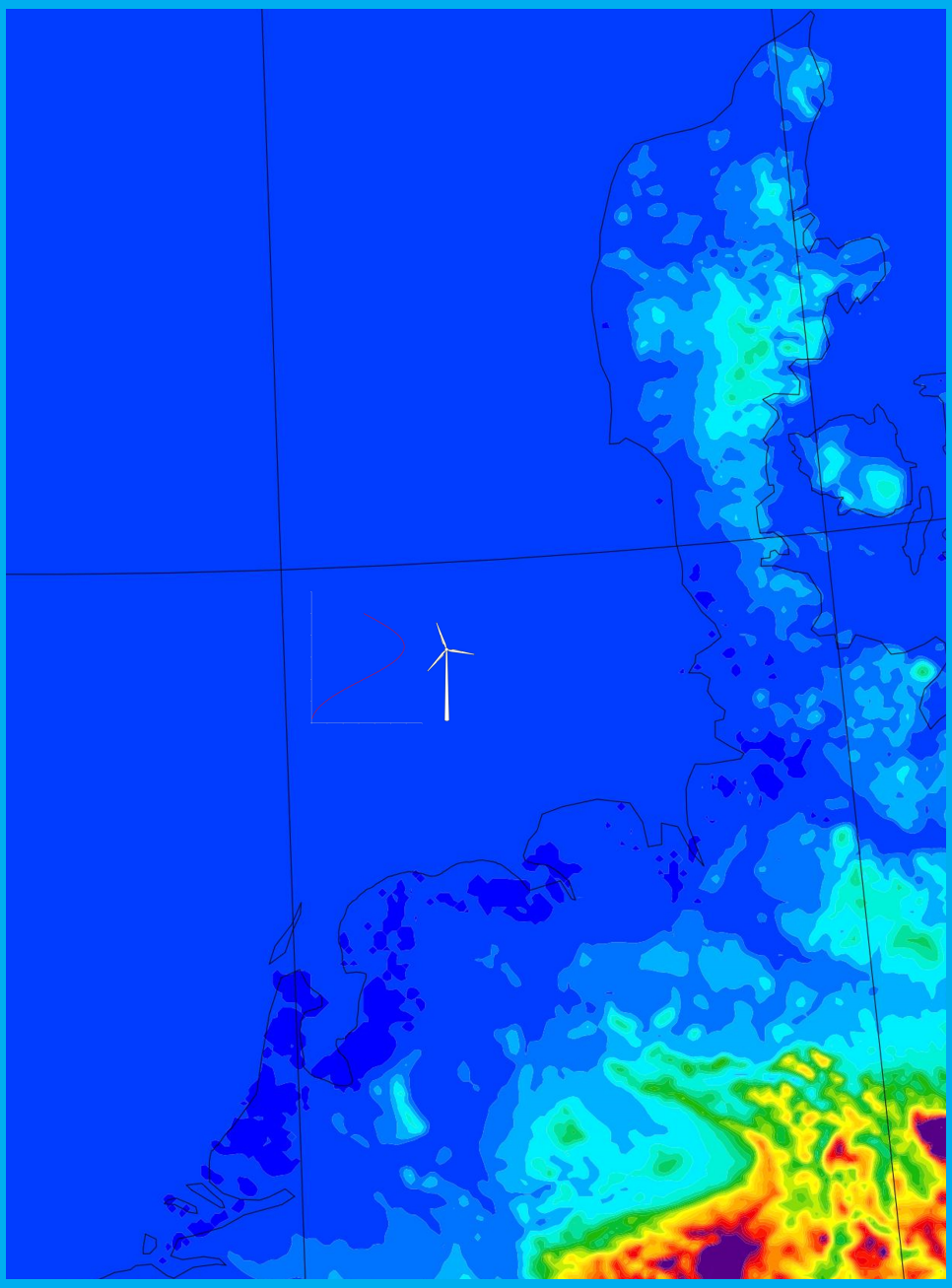

A new coupled modelling framework for turbine inflow generation: mesoscale-synthetic turbulence

by

Adithya Vemuri

to obtain the degree of Master of Science in the field of Sustainable Energy Technology
at the Delft University of Technology.

Student number:	4617576	
Project duration:	September 19, 2018 – August 15, 2019	
Thesis committee:	Prof. dr. Simon J. Watson	Supervisor
	Dr. Sukanta Basu	Supervisor
	Dr. ir. Wim Bierbooms	Thesis committee

An electronic version of this thesis is available at http://repository.tudelft.nl/.

TU Delft

Abstract

At the mercy of strong winds, high wind shear, unstable boundary layer and anomalous atmospheric conditions, stands a wind turbine designed to produce sustainable power under harsh conditions. The field of wind energy is a promising prospect for a sustainable future. Diverse research towards the improvement of a wind turbine's capability and cost is currently the focus of the wind energy industry. With higher wind turbines being designed every day, various challenges and limitations of the current state-of-the-art surface; anomalous atmospheric conditions, structural integrity and cost.

The goal of this thesis is to extend the approach to design a site-specific wind turbine considering an anomalous atmospheric condition. By coupling a mesoscale model with a stochastic turbulence function, a wind field capable of depicting a particular atmospheric condition is created. Using an aeroelastic solver the resulting loads on a wind turbine can be simulated. The methodology uses Weather, Research and Forecasting (WRF) model to re-create an event of low-level jet identified at the met mast of FINO-1, off coast Germany. The wind profile is coupled with a stochastic turbulence function designed at FINO-1 to be used as wind field for the aeroelastic solver, FAST.

A literature survey identified a multitude of approaches used for simulating a low-level jet and analyse the loads on a wind turbine, the majority of which indicate high computational costs and contrived re-creations of the event. Thus, the challenge was to identify a near-realistic event creation with low computational costs. Therefore, coupling a low-resolution mesoscale model to create the event with a site-specific stochastic turbulence function is used to analyse loads on a wind turbine.

Meteorological data analysis at FINO-1 led to the identification of three case studies of low-level jets under varied stability conditions of the atmosphere. The case studies are compared with the International Electrotechnical Commission (IEC) standard's, IEC – 61400 – Ed3; IEC Kaimal and IEC Great Planes Low Level Jet (GPLLJ) spectrum. For cases with high stability, on an average proposed model predicts 21% higher stress on blade root and 27% higher at the tower top and base in comparison to IEC GPLLJ and 15% and 30% lower in comparison to IEC Kaimal, respectively. Similarly, under unstable conditions, proposed model predicts similar loads on the blade root, 7% lower loads at the tower top and base in comparison to IEC GPLLJ and 30% higher loads for blade root and tower top and base in comparison to IEC Kaimal. Comparing these results with literature on high stability loading higher loads are expected under these conditions.

Concluding, this project developed a model framework to analyse anomalous atmospheric phenomena on a wind turbine specific to a site with low computational costs. While the capabilities of the model have been successfully showcased, only a partial validation on a benchmark case has been carried out. Therefore, going forward a full physical validation of the model for its accuracy for its target applications is recommended.

Preface

Presented here is the dissertation "A new coupled modelling framework for turbine inflow generation: mesoscale - synthetic turbulence", the basis of which is to propose a modelling framework to simulate atmospheric phenomena realistically on a wind turbine to access the effective loading. This thesis is written to fulfill the graduation requirement of the master's program: Sustainable energy technology at Delft University of technology.

Under the supervision of dr. Simon Watson and dr. Sukanta Basu the research question was formulated to challenge the need for such a modelling framework. The research was challenging and exciting with minimal available literature. This dissertation aims to present a comparison between traditional wind turbine loading and one considering a near-realistic site-specific loading analysis. The validation of which is encouraged to explore via site measurements.

To my supervisors, thank you for generously sharing your time and expertise on the subject matter. To, dr. Etienne Cheynet for sharing the coefficients required in the definition of the model proposed for this thesis dissertation. I would like to thank Bedessa Cheneka and Bowen Li for their encouragement, critical feedback and help in teaching me weather research and forecast model. To my friends and the wind-meteorology group, started passionately by dr. Sukanta Basu, for sharing their critical feedback on the progression of my thesis. Weekly presentations of which established a platform of knowledge sharing and critical learning, the experience has been very insightful. I would also like to acknowledge dr. Carlos Simao Ferreira for his help and guidance in my search for a thesis topic in the field of my interest.

Finally, Ashwin Vijay for helping me manage a challenging thesis, Mihir Mehta and Neel Nagda for their time, help and discussions on visualizing statistics, spectral equations and FAST simulations.

My parents and my sister deserve a particular note of thanks: your wise counsel, motivation and kind words have, as always, served me well.

Hoping you would find this read interesting and thoughtful.

Adithya Vemuri
Delft, August 2019

Contents

List of Figures ix

List of Tables xiii

Nomenclature xv

1 Introduction 1

2 Literature review 3
- 2.1 Wind turbine standards . . . 3
- 2.2 Atmospheric phenomena . . . 5
- 2.3 Search for a universal spectral equation . . . 9
- 2.4 Basics of a spectral form . . . 9
- 2.5 Wind field modelling - Kaimal spectrum . . . 11
  - 2.5.1 Step: 1 - Spectral equation: IEC-Kaimal Spectrum . . . 11
  - 2.5.2 Step: 2 - Coherence function . . . 12
  - 2.5.3 Step: 3 - Wind field generation . . . 13
- 2.6 CJR model . . . 13

3 Data analysis 15
- 3.1 FINO 1 met-mast . . . 15
- 3.2 Methodology . . . 16
- 3.3 Results and discussion . . . 18

4 Model framework 21
- 4.1 Model chain . . . 21
- 4.2 Weather, Research and Forecast . . . 22
  - 4.2.1 WRF-ARW software framework . . . 23
  - 4.2.2 WRF implementation . . . 25
- 4.3 Synthetic turbulence model . . . 26
- 4.4 NREL - FAST . . . 26
  - 4.4.1 FAST model framework . . . 27
  - 4.4.2 FAST Implementation . . . 28

5 Case studies and Discussion 29
- 5.1 Case study 1 - 2 July 2006 . . . 30
  - 5.1.1 WRF results . . . 30
  - 5.1.2 FAST results . . . 31
- 5.2 Case study 2 - 23 May 2012 . . . 33
  - 5.2.1 WRF results . . . 33
  - 5.2.2 FAST results . . . 34
- 5.3 Case study 3 - 14 April 2004 . . . 37
  - 5.3.1 WRF results . . . 37
  - 5.3.2 FAST results . . . 38
- 5.4 Discussion . . . 40

A Appendix 43
- A.1 Data analysis - wind ramp, trend plots . . . 43

B Appendix **45**
B.1 WPS-setup . . . 45
B.2 WRF-setup . . . 47
B.3 .bts format conversion . . . 51
B.4 Code validation . . . 52
B.5 Coefficients for CJR model . . . 53

C Appendix **57**
C.1 WRF contours and hodographs . . . 57
C.2 Case study 1 - 02-July-2006 . . . 57
C.3 Case study 2 - 23-May-2012 . . . 59
C.4 Case study 3 - 14-April-2004 . . . 60

Bibliography **63**

List of Figures

2.1 Depicting diurnal cycle of the atmosphere using potential temperature 5
2.2 Wind speed profiles for stable, unstable and neutral conditions using MOST, equation: 2.8 for an arbitrary value of mean wind velocity, friction velocity, surface roughness and height. 6
2.3 Formation of LLJ over time. 8
2.4 A Venn diagram depicting the correlation between the 95^{th} percentile data of LLJ with shear and veer, the numbers represent the percentage of data from the met mast Ijmuiden. 8
2.5 A schematic of Fourier transformation 9
2.6 Schematic of energy spectrum in the atmospheric boundary layer showing distinct regions of energy production (A) and dissipation (C) and the inertial subrange (B), where both energy production and dissipation are negligible. A is the integral scale of turbulence and η is the Kolmogorov microscale[30] 10
2.7 Kaimal spectrum for an arbitrary frequency range 12
2.8 Plotted the u-component CJR spectral model for an arbitrary stability value of 1.8. 13

3.1 FINO-1 platform north sea 15
3.2 Histogram depicting the distribution of shear exponent α, 95^{th} and 5^{th} percentile thresholds and median of α (=0.066). 95^{th} and 5^{th} percentile for shear coefficient are $[0.33, -0.12]$. 16
3.3 Histogram depicting the distribution of wind veer, β, 95^{th} and 5^{th} percentile thresholds. 16
3.4 Histogram of threshold wind shear events for days of years from 2004 to 2012 filtered based on 95^{th} percentile value of the shear coefficient. 17
3.5 Example of a kinked profiles at FINO 1, presented data is an example of ignored dates. Here wind speeds are normalized with respect to the maximum wind speed for the day to understand the profiles over the time of 24 hours. 18
3.6 Starting from the left, plot of observed data at FINO 1 for the date 23^{rd} May 2012 and plot of wind speed profiles normalized over the day. 19
3.7 Starting from the left, plot of observed data at FINO 1 for the date 2^{nd} July 2006 and plot of wind speed profiles normalized over the day. 19
3.8 Starting from the left, plot of observed data at FINO 1 for the date 14^{th} April 2004 and plot of wind speed profiles normalized over the day. 20

4.1 Proposed model chain. 21
4.2 Comparison between conventional weather prediction and numerical weather prediction. 22
4.3 WRF modelling framework 23
4.4 A representation of nested domains used for the assessment of low level jets over FINO1 25
4.5 FAST - NREL model framework for bottom-fixed offshore wind turbine. 27

5.1 Comparison of observed and simulated wind fields for the case 2^{nd} July 2006, starting from the left, time vs height plot of observed data at FINO 1 and time vs height plot of WRF simulation. . 30
5.2 Wind shear comparison between WRF and observations for the day: 2^{nd} July 2006 at 17:00. Similar wind profile is simulated. 31
5.3 Comparison of out of plane bending moment and generator power for IEC Kaimal - NTM model, CJR model and IEC GPLLJ model. 31
5.4 Comparison of tower base fore-aft moment and magnitude of wind speeds for IEC Kaimal - NTM model, CJR model and IEC GPLLJ model. 32
5.5 Comparison of u and v component of wind speeds for IEC Kaimal - NTM model, CJR model and IEC GPLLJ model. 32
5.6 Starting from left, comparison of spectra for w-component of wind speeds. Right, comparison of tower top yaw moment for IEC Kaimal - NTM model, CJR model and IEC GPLLJ model. 33

5.7 Comparison of observed and simulated wind fields for the case 23^{rd} May 2012, starting from the left, time vs height plot of observed data at FINO 1 and time vs height plot of WRF simulation. 34
5.8 Wind shear comparison between WRF and observations for the day: 23^{rd} May 2006 at 18:00. Similar wind profile is simulated. . . . 34
5.9 Comparison of out of plane bending moment and generator power for IEC Kaimal - NTM model, CJR model and IEC GPLLJ model. . . . 35
5.10 Comparison of tower base fore-aft moment and magnitude of wind speeds for IEC Kaimal - NTM model, CJR model and IEC GPLLJ model. . . . 35
5.11 Comparison of wind spectra for components of wind field as input to FAST for spectral models, IEC Kaimal, GP_LLJ and CJR model. . . . 36
5.12 Starting from left, w-component wind spectra for IEC Kaimal, CJR and GP_LLJ model as input wind fields to FAST. Right, comparison of tower top yaw moment for IEC Kaimal - NTM model, CJR model and IEC GPLLJ model. . . . 36
5.13 Comparison of observed and simulated wind fields for the case 14^{th} April 2004, starting from the left, time vs height plot of observed data at FINO 1 and time vs height plot of WRF simulation. 37
5.14 Wind shear comparison between WRF and observations for the day: 14^{th} April 2004 at 20:20. Similar wind profile is simulated. . . . 38
5.15 Comparison of out of plane bending moment and generator power for IEC Kaimal - NTM model, CJR model and IEC GPLLJ model. . . . 38
5.16 Comparison of tower base fore-aft moment and magnitude of wind speeds for IEC Kaimal - NTM model, CJR model and IEC GPLLJ model. . . . 39
5.17 Comparison of wind spectra for IEC Kaimal, GP_LLJ and CJR model as input to FAST simulations. 39
5.18 Starting from right, comparison of wind spectra for w-component of CJR, IEC Kaimal and GP_LLJ model. Right, comparison of tower top yaw moment for IEC Kaimal - NTM model, CJR model and IEC GPLLJ model. . . . 39
5.19 Comparison of stress at cylinder 2 for presented case studies for IEC Kaimal - NTM model, CJR model and IEC GPLLJ model. . . . 40
5.20 Comparison of tip deflection for presented case studies for IEC Kaimal - NTM model, CJR model and IEC GPLLJ model. . . . 41
5.21 Comparison of stress at tower top and base for presented case studies for IEC Kaimal - NTM model, CJR model and IEC GPLLJ model. . . . 41

A.1 Wind ramp for the day of 2^{nd} July 2006. . . . 43
A.2 Wind ramp for the day of 14^{th} April 2004. . . . 43
A.3 Wind ramp for the day of 23^{rd} May 2012. . . . 44
A.4 Histogram plotting occurrences of 95^{th} percentile threshold of shear exponent for the wind range of 5m/s to 30m/s. . . . 44

B.1 Spectral comparison between Etienne Cheynet's mathworks code and TurbSim - NREL, using IEC Kaimal spectrum. . . . 52

C.1 Comparison of re-analysis archives and simulated WRF for the case 2^{nd} July 2006, starting from the left, re-analysis archives plot, and WRF simulations plots for the same time(right), barbs represent magnitude of wind speeds. Each line on the plot represents isobars with pressure in millibar annotated on the line. . . . 57
C.2 From left, hodograph at near hub height - 100m for the day and hodograph during low level jet occurring between 14:00 and 19:00. . . . 58
C.3 Comparison of re-analysis archives and simulated WRF for the case 23^{rd} May 2012, starting from the left, re-analysis archives plot, right, WRF simulation for domain 1, barbs represent magnitude of wind speeds. Each line on the plot represents isobars with pressure in millibar annotated on the line. Plots presented are for the same time: 00:00 . . . 59
C.4 From left, hodograph at near hub height - 100m for the day and hodograph during low level jet occurring between 16:00 and 20:00. . . . 59
C.5 Comparison of re-analysis archives and simulated WRF for the case 14^{th} April 2004, starting from the left, re-analysis archives plot, right, WRF simulation for domain 1, barbs represent magnitude of wind speeds. Each line on the plot represents isobars with pressure in millibar annotated on the line. Plots presented are for the same time: 00:00 . . . 60

C.6 From left, hodograph at near hub height - 100m for the day and hodograph during low level jet occurring between 20:00 on the 14^{th} and 01:00 on the 15^{th}. 61

List of Tables

2.1 Wind turbine classes defined by IEC-standard edition 3[15] . . . 4
2.2 Design load case 1 - power production, per IEC-61400 - edition 3 . . . 4

3.1 Presents the data-sets explored from eight years of observational data. . . . 17
3.2 Table presenting the final selection of dates and events that will be simulated. . . . 18

4.1 WRF computing time comparison for nested domains. . . . 26
4.2 Specification of NREL-5MW wind turbine used for the study. . . . 27
4.3 A summary of the loads that will be studied. . . . 28

5.1 Material properties and safety factors . . . 29
5.2 Ultimate loads comparison between CJR, IEC Kaimal and IEC GPLLJ models. . . . 33
5.3 Ultimate loads comparison between CJR, IEC Kaimal and IEC GPLLJ models. . . . 36
5.4 Ultimate loads comparison between CJR, IEC Kaimal and IEC GPLLJ models. . . . 40
5.5 Consolidated results of stresses and tip deflection for cases studies identified. . . . 42

B.1 Namelist.wps for one of the case study: 23rd May 2012, similar namelist is used for other case studies, with change in start-date and end-date. . . . 45
B.2 Namelist.wps for one of the case study: 23rd May 2012, similar namelist is used for other case studies, with change in start-date and end-date. . . . 46
B.3 Namelist.Input for one of the case study: 23rd May 2012, same namelist is used for other case studies. . . . 47
B.4 Namelist.Input for one of the case study: 23rd May 2012, same namelist is used for other case studies. . . . 48
B.6 Namelist.Input for one of the case study: 23rd May 2012, same namelist is used for other case studies. . . . 48
B.5 Namelist.Input for one of the case study: 23rd May 2012, same namelist is used for other case studies. . . . 49
B.7 Namelist.Input for one of the case study: 23rd May 2012, same namelist is used for other case studies. . . . 49
B.8 Namelist.Input for one of the case study: 23rd May 2012, same namelist is used for other case studies. . . . 50
B.9 u-component velocity spectrum coefficients, obtained from fitting observations to equation: 2.25 and 2.26 . . . 53
B.10 v-component velocity spectrum coefficients, obtained from fitting observations to equation: 2.25 and 2.26 . . . 54
B.11 w-component velocity spectrum coefficients, obtained from fitting observations to equation 2.25. . . . 55

Nomenclature

Abbreviations

CFD	Computational fluid dynamics
DLC	Design load case
DNS	Direct numerical simulations
ETM	Extreme turbulence model
$FINO$	Forschungsplattformen in nord- und ostsee nr. 1,2,3
$GPLLJ$	Great planes Low level jet
IEC	International electrotechnical commission
$LCOE$	Levelized cost of electricity
LES	Large eddy simulations
LLJ	Low level jet
$MOST$	Monin Obhukov similarity theory
NTM	Normal turbulence model
NWP	Numerical weather prediction
$WASP$	Wind atlas analysis and application program
WRF	Weather, research and forecasting

Physical constants

κ	Von-Karman constant	$0.41\,(-)$
g	Acceleration due to gravity	$9.81\,m/s^2$
R_d	Specific gas constant of dry air	$28.9645\,g/mol$

Symbols

α	Wind shear exponent	$(-)$
β	Wind veer	$degree$
ϵ	Dissipation	m^2/s^3
γ	Coherence	$(-)$
γ_s	Safety factor	$(-)$
ρ	Density	m/s
σ_s	Tensile stress	N/m^2
σ_u^2	Variance along u-component of wind	m^2/s^2
τ	Shear stress	N/m^2

ζ	Stability parameter	(–)
f	Coriolis parameter	rad/s
f	Frequency	Hz
I_{ref}, Ti	Turbulence intensity	(–)
k	Wave number	$m^(-1)$
L_u	Integral length scale parameter	m
M	Molar mass	g/mol
p	Pressure	Pa
q	Specific humidity	(–)
S_u	Wind power spectrum of u-component	W/Hz
$Theta$	Potential temperature	K
$Theta_v$	Virtual potential temperature	K
U_*	Friction velocity	m/s
V_{hub}	Hub height wind velocity	m/s
V_{in}	Cut-in wind velocity	m/s
V_{out}	Cut-out wind velocity	m/s
V_{ref}	Reference wind velocity	m/s
z	Height above ground	m
Z_{hub}	Hub height	m

1 Introduction

The ever-growing field of wind energy has much to offer for a sustainable future. The statistics for wind energy in Europe indicate a growing technology with its milestones and success stories. The year-2018 for wind energy in Europe[1] has been fruitful, with 2.6GW increase in wind energy installed amounting to capacity growth of 18%. A total investment of 10.3 billion euros was observed in the year-2018. 15 new offshore wind farms were installed. The growing market for wind energy opens to vast majorities of academia and research; on a component level through inter-disciplinary system. For example; LCOE-reduction (levelized cost of electricity) considering optimization of wind farms, site specific design of wind turbines considering atmospheric stability and atmospheric phenomena.

Rise in demand for green and clean energy has urged countries and companies alike to increase installed capacity of wind power. In Europe, shallow waters of the North sea have always been an attractive option for offshore Wind energy projects. Offshore wind and floating offshore wind energy are now a promising prospect in the field. Offshore wind is current preferred over floating wind energy primarily due to lower costs of manufacturing, installation, operation and maintenance[2]. The Netherlands has planned to build the world largest wind farm among other wind farms in the coming decades; Tennet's North Sea Wind Power Hub project[3] aims to connect multiple European countries to a common electric grid that is planned to be built on a remote artificially-constructed island. The island would be surrounded by Wind farms with a planned installed capacity of 30GW. A project of this size will demand extensive analysis pertaining to cost, design, operations and maintenance. This growth in the field leads to a high requirement for knowledge in the relevant research subjects. This thesis concentrates on one such specific subject: site specific wind turbines; their wind fields and the resulting loads, done through simulations. Site-specific wind turbine proposes a non-standardized wind turbine designed specifically to the climatology of a location. The thesis aims to propose a modelling framework to consider the atmospheric phenomena into the design of a wind turbine, specifically low level jets. The location of interest is off coast of Borkum, Germany, Fino - 1. The current state-of-the-art model for inflow wind field are based on synthetic turbulence generators or stochastic models considering a neutral boundary layer such as Kaimal spectrum[4], Von Karman spectrum[5] or Mann spectrum[6]. However, these stochatic models lack the specificity of a location and its particular atmospheric phenomena. Various inflow simulators pre-define and use said spectral models for accessing the loads on a wind turbine, for example NREL (National renewable energy laboratory) TurbSim[7]. These models are computationally not expensive and provide reliable results with percentage for uncertainty, as it has been an industry standard. However, fact of the matter is the boundary layer is rarely neutral and is influenced by solar insolation (diurnal cycle[8]). Studies on atmospheric phenomena and stability indicate significant effect on a wind turbine. For example, Sathe *et al*[9] presented the influence of atmospheric stability on wind turbine loading, indicating a variation of up-to 17% in comparison to neutral atmospheric boundary layer. Park *et al.*'s[10] study compared an analysis of the results of loading between a neutral and stable boundary layer, indicating higher loads in case of a stable boundary layer. This uncertainty in boundary layer stability is thus carried forward to the design parameters of a wind turbine, therefore a model capable of incorporating the dynamic effects of the atmospheric boundary layer is much in need. Various literature has been published in the field of computational wind energy in order to "realistically" simulate atmospheric effects on a wind turbine[11], an inflow wind field to incorporate the effects of atmospheric phenomena. One can simulate a particular atmospheric phenomena on weather prediction models; weather research and forecasting model

(WRF). Based on boundary layer schemes and parameterized Reynolds averaged Naiver Stokes equations, similarly large eddy simulations (LES) and direct numerical simulations (DNS) are also capable of recreating an atmospheric phenomena. Ideally DNS will produce the best results for a given atmospheric phenomena for a specific length scale however, computation limitations have limited the usage of DNS in wind energy simulations.

Thus, the research scope formulated is to propose a modelling framework to create realistic wind field considering an atmospheric phenomena, low level jet with low computational requirements. This thesis aims to propose a modelling framework to access the impact of low-level jets on wind turbine loads. Using a coupled model chain mesoscale-synthetic turbulence. This thesis also presents a comparison of the proposed model and the relevant IEC (international electrotechnical commission) standards. Wind turbine loading is simulated using an aeroelastic solver FAST-NREL[12]. This thesis aims to incorporate the effect of low level jets combined with a site specific spectral model proposed by Cheynet *et al.*[13] identified from the met-mast FINO-1[14], making this a "near-real" simulation given limited computational power. It is intended that the proposed modelling framework be applied to other atmospheric phenomena in the coming research proposals. Application of this approach can be seen for the design of site specific wind turbines or to estimate/predict the current “life” of a turbine.

Presented herein chapter 2: Literature review, consolidates literature study conducted for this thesis. Chapter 3: Data analysis, presents the data analysis methodology and results to identify low level jets for FINO1. Chapter 4: Model framework, presents overview of the model and detailed explanation of the coupling. Chapter 5: Case studies, presents three case studies chosen to understand the results from the proposed model chain. In aspiration that this approach could be employed for preliminary design and development of site specific Wind turbines upon further validation.

2

Literature review

This chapters consolidates a general literature review followed in order to develop a method of approach for the thesis topic in question. Including a short study on wind turbine standards, a description of atmospheric phenomena studied and the application used to model such phenomena, the basics of spectral equations and how to model them. Lastly, a brief description of models used in this thesis. This chapter aims to be an introductory step in describing the model framework proposed. Following chapter on model framework will cover the models used and the literature study in greater detail.

2.1. Wind turbine standards

The International Electrotechnical Commission (IEC) prepares and publishes standards for wind turbine certification. A critical requirement in the development of a wind turbine. IEC publishes a standard for wind turbine design, called IEC-61400[15]. The standard includes, minimum design requirements for the certification of a wind turbine. The standards are widely used in the industry and form a benchmark for wind turbine producers. Discussed here are the various parameters and their significance in the design of a wind turbine.

Describing the standards, numerous parameters influence the design of a wind turbine such as environmental conditions, mechanical properties, service-life, durability and operational requirements, electrical grid requirements and sea-bed/soil parameters, to name a few. IEC defines various load cases called design load cases (DLCs) based on and derived from the combinations of the aforementioned parameters. The defining part of a DLC are the environmental conditions. They are further divided into; normal and extreme external conditions. Normal conditions are assumed to be the dominant operating conditions effecting the loads on a wind turbine (95% of the time) and extreme conditions are considered a rare and extreme phenomena. Selection of DLC is a site-specific task, basing on observed data recorded from a met-mast installed at the site of discussion. A generalization of wind turbines based on recorded variable from the met-mast can be performed, IEC defines these classes of wind turbines as presented in the figure: 2.1. Class A, B and C are defined based on the turbulence intensity, roman number one, two and three define the 50-year maximum wind speed. It is intended that these parameter be defined from a met-mast installed at the location for a possible wind turbine or wind farm installation. Met-masts are a an expensive affair, therefore scaling using Wind Atlas Analysis and Application Program(WASP) is also preferred in the industry in order to define the "site-parameter"; turbulence intensity and 50-year max wind speeds. It must be noted that S - class from the figure: 2.1 stands for a user defined customized class. Following these definition for the classification of the wind turbines and the IEC standard's design methodology a conservative lifetime of 20 years for a wind turbine is predicted. An example for a DLC is presented in the figure: 2.2. Presented in figure is the DLC 1, the stage of operation of the turbine is power production. Four classes of wind conditions comprising Normal wind and extreme wind conditions represent the DLC. U refers to ultimate load case, F refers to fatigue load case, N is the safety factor defined in the standard, V_{in}, V_{hub}, V_{out} represent velocity of cut-in, rated wind speed and cut-out wind speed.

Wind turbine class		I	II	III	S
V_{ref}	(m/s)	50	42.5	37.5	Values specified by the designer
A	I_{ref} (-)	0.16			
B	I_{ref} (-)	0.14			
C	I_{ref} (-)	0.12			

Table 2.1: Wind turbine classes defined by IEC-standard edition 3[15]

Design situation	DLC	Wind condition		Other conditions	Type of analysis	Partial safety factor
Power production	1.1	NTM	$V_{in} < V_{hub} < V_{out}$	For extrapolation of extreme events	U	N
	1.2	NTM	$V_{in} < V_{hub} < V_{out}$		F	*
	1.3	ETM	$V_{in} < V_{hub} < V_{out}$		U	N

Table 2.2: Design load case 1 - power production, per IEC-61400 - edition 3

Considering the scope of the thesis only the environmental conditions and the modeled wind field for the respective condition are discussed in this dissertation.

Wind field for the certification of wind turbines under the IEC standards are defined by a stochastic wind field model capable of producing turbulence about a mean wind profile considering a constant turbulence intensity measured ideally at the hub height, recalling, two classifications of wind fields (pertaining to environmental conditions) are defined by IEC; Normal turbulence wind field and extreme turbulence wind field. IEC defines the mean wind profile as derived from a power law as described in the equation: 2.1. u_{hub} is the mean velocity at a hub height under. α is the power law exponent, assumed as 2.

$$u(z) = u_{hub}\left(\frac{z}{z_{hub}}\right)^{\alpha} \tag{2.1}$$

It must be noted that a Rayleigh distribution is assumed for wind speed probability at the site of the wind turbine. It must also be noted that the turbulence intensity is assumed a constant over the range(height) of wind turbine.

In order to generate a wind field for load calculations ideally one would require the recorded values of wind field for the range of the wind turbine at the site location, this is a very unrealistic way to measure the wind speeds and the effective loads. Various methodologies are used to generate a wind field, including and not exclusive to LES, CFD (computational fluid dynamics) and spectral models. Discussed here is least computationally expensive model, a spectral model consisting of spectral equations and coherence functions. A spectral equation defines the energy content of the wind component at a particular location. Thus intuitively every location would have a site-specific spectral equation. An example for a spectral equation is as presented in equation: 2.2.

$$\frac{fS_u(f)}{\sigma_u^2} = \frac{4fL_u/V_{hub}}{(1+6fL_u/V_{hub})^{\frac{5}{3}}} \tag{2.2}$$

Presented here is the Kaimal spectral equation for the along wind component, u as used by the IEC standards. Where f is the frequency in Hertz, L_u is the integral length scale parameter, S_u is the u component velocity spectrum and σ_u^2 is the variance. This equation is normalized with respect to the variance, σ_u^2 which depends on turbulence intensity by the relation presented in the equation: 2.3[16]. Further explanation on spectral equations is presented in the following sections.

$$\sigma_u^2 = Ti(\frac{3}{4}U + 5.6) \tag{2.3}$$

IEC assumes spectral models that vary based on the turbulence intensity and wind turbine class. A software such as TurbSim can simulate such a wind field using a such spectral model, such as one presented in the equation: 2.2, and a coherence model. IEC-61400 edition 3 uses Mann model of spectrum for wind field generation. IEC also incorporates Kaimal and von Karman spectrum. Mentioned spectra are derived based considering a neutral atmospheric condition. As mentioned above a neutral atmosphere is a very rare phenomena in the boundary layer.

2.2. Atmospheric phenomena

The dynamics of the atmospheric boundary layer are complex with various parameters influencing its nature. Discussed here are the parameters relevant to low levels jets and the stability of the atmospheric boundary. Stability is primarily influenced by solar insolation. Day and night cycle due the revolution of Earth causes an upward heat flux during the day and a residual heat flux during the night. During the day the heat and the following increase in entropy in the boundary layer are major drivers for turbulence generation, the cooling of the surface during the night causes a stratification. Figure: 2.1[8] presents the cycle in a more intuitive format, it must be noted the height axes in the figure has different scales, intentionally for better visualization.

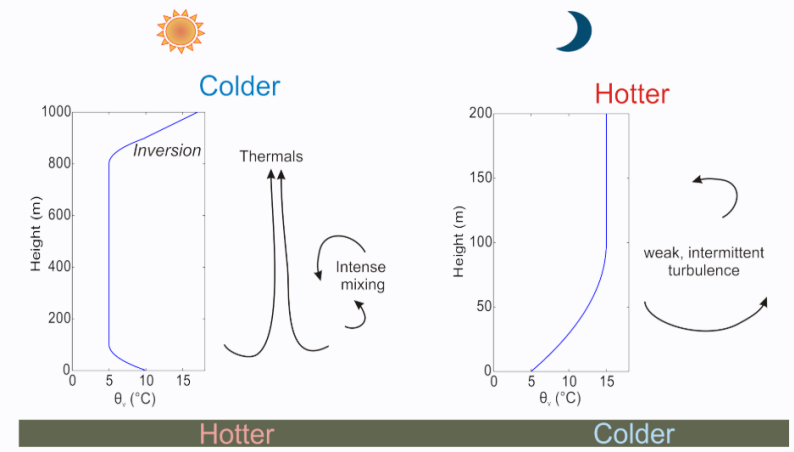

Figure 2.1: Depicting diurnal cycle of the atmosphere using potential temperature

In order to define the virtual potential temperature, θ_v we must first define potential temperature and virtual temperature. The potential temperature, θ of a fluid parcel at pressure is the temperature that the parcel would attain if adiabatically brought to a standard reference pressure. It is assumed that the moisture content in the atmosphere, q, is constant with height. When θ decreases with height the atmosphere is unstable and vice versa. Virtual temperature (of dry air) can be explained through an example; moist air is lighter than dry air (water vapour is lighter than Nitrogen and Oxygen - major constituents of the atmosphere) therefore moist air would have a higher "virtual" temperature than dry air. That is, virtual temperature is the temperature dry air (heavier) should have to achieve the same density as the moist air. Virtual potential temperature is the temperature an air(dry) parcel will have if brought adiabatically to a reference pressure, it is given by the equation: 2.4.

$$\theta_v = (1 + (M_{air}/M_{H_2O-1})q)T(p_0/p)^{\kappa} \tag{2.4}$$

Where, M_{air}/M_{H_2O} is the molar mass of dry air ≈ 0.61, T is the temperature of moist air, p_0 is the reference pressure, p is the pressure (or level of the atmosphere) in question, q is the specific humidity (mass of water vapour per unit mass of moist air) and κ is defined by the equation: 2.5, R_d is the specific gas constant for dry air, C_{pd} is the specific heat capacity of dry air.

$$\kappa = R_d(1 - 0.23q)/C_{pd} \tag{2.5}$$

θ_v is plotted against the height of the atmosphere. We observe θ_v to decrease with height during the day and increases with height during the night, indicating an unstable boundary layer during the day and a stable boundary layer during the night. (Note: the surface has higher heat carrying capacity than the atmosphere, therefore it is colder at the night). The effect of this diurnal cycle causes stratification in the atmospheric boundary layer (at locations where the slope of θ_v changes). This diurnal cycle forces mixing of the layers and generation of turbulence scales via buoyancy and shear. The stability of the atmosphere is quantified by Monin and Obhukov[17] in 1954 in the study published, Monin Obhukov similarity theory (MOST). The study defines a parameter ζ evaluated as z/L indicates the stability of the atmosphere. Here L is called the Obhukov length and z is the height of measurement. The Obhukov length is a function of friction velocity(u_*), virtual potential temperature(θ_v), and vertical heat flux, $w'\theta'_v$ (w' is the vertical velocity turbulent component). It is defined by the equation: 2.6.

$$L = -\frac{u_*^3 \overline{\theta_v}}{\kappa g (\overline{w'\theta'_v})_s} \tag{2.6}$$

The parameters κ and g are constants; von karman constant defined between 0.4 and 0.41 and acceleration due to gravity, respectively. It must be noted that $\overline{w'\theta'}_s$ is derived from the relation specified in the equation: 2.7 between $\overline{w'\theta'}$ and $\overline{w'q'}$.

$$\overline{w'\theta'}_s = \overline{w'\theta'} + 0.61 \cdot \overline{w'q'} \tag{2.7}$$

The stability of the atmosphere boundary changes with time, and is rarely constant. Therefore, wind shear as defined by a power law which does not incorporate the stability of the atmosphere is unrealistic. MOST proposes a velocity profile considering the effects of stability of the atmosphere. MOST theory was derived from extensive field work and observational data, taken from a met-mast of 45m in height. The proposed velocity profile that unlike the power law and log law takes into consideration the effects of stability of the atmosphere as a function of ζ. Equation: 2.8 depicts the MOST equation for a velocity profile.

$$U(z) = \frac{u_*}{\kappa}\left[\ln\left(\frac{z}{z_0}\right) - \psi_m(\zeta)\right] \tag{2.8}$$

ψ_m is a function of the stability parameter ζ and analytical equations for ψ_m are found by field measurements. It is inferred upon ζ as zero the profile collapses to logarithmic law and is called a neutral condition wind profile. With ζ greater than zero the profile adapts to a stable condition wind profile, and a negative ζ adapts an unstable wind profile. Figure: 2.2 presents an example for visualizing these wind profiles. It must be noted that wind shear in a stable profile (or a stable boundary layer) is higher than a neutral or unstable profile.

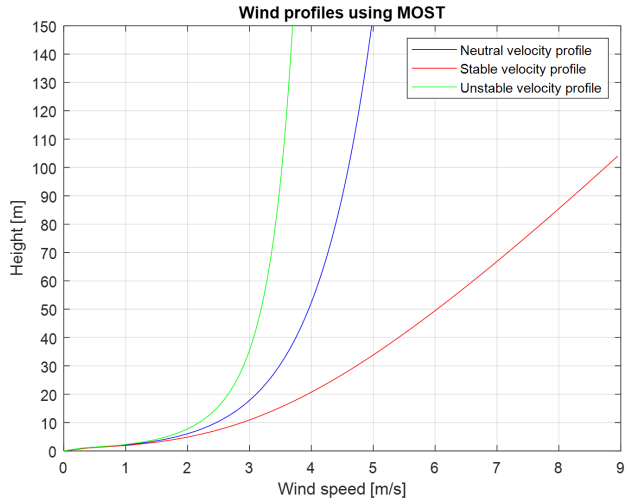

Figure 2.2: Wind speed profiles for stable, unstable and neutral conditions using MOST, equation: 2.8 for an arbitrary value of mean wind velocity, friction velocity, surface roughness and height.

To access the effect of stability of atmosphere such as, increased shear in stable boundary layer. Sathe *et al.* [9] described the effects of atmospheric stability on Wind turbine loads, the study's primarily goal was to understand the effect of stable boundary layer on a wind turbine's damage equivalent loads. The study was conducted at a four specific site, using one site's wind profile to estimate the profile at other. The study used Gryning similarity theory for the development of wind fields. Using HAWC2 the study observed 17% higher variation in the damage equivalent loads between neutral and stable atmosphere. Another study by Park *et al.*[10] studied the effects of stable boundary layer using large eddy simulations. The primary scope of this study was to find a way to recreate stable boundary layer in stochastic wind field driven by a power law. The methodology followed in three steps; starting from enhancing the wind shear, inducing wind veer and addition of turbulence variation. 44 such LES simulations were conducted, the results of these simulations demonstrated an increase in the wind turbine loading under Stable boundary layer. Following this research

another study published by the authors on Large-eddy simulation of stable boundary layer turbulence and estimation of associated wind turbine loads[18] observed under stable conditions and high shear exponent value, the possibility of low level jet occurrence (considering 44 idealised - LES simulations) is high. In the scope of this thesis project a method to recreate a "near-realistic" wind field for low level jets will be discussed.

A broad definition of a low level jet is any wind profile in the lower-tropospheric layer that poses wind speeds higher than the geostrophic wind speeds in that vertical profile is considered a low level jet[19]. A low level jet can occur under favorable synoptic conditions anywhere in the world. Practically LLJ mainly have an impact on moisture transport and large wind shear that can be associated with applicability of wind turbines in the area. Few common analogies that define a low level jet are presented below:

- Fast moving current of air near the surface.
- Large wind speeds below the jet streams, wind speeds are super-geostrophic.
- Wind speed above jet 50%-75% or less of the maximum.
- Strong lateral shear on both sides, typical width 200-300km.
- LLJs have most commonly reported in the spring and the summer.
- LLJs tend to have a maximum wind at the height of 800m above ground level. Strong LLJs are primarily a nightime feature.

Formation or cause of an LLJ has been theorized by the following meteorological phenomena.

- Inertial oscillation.
- Baroclinicity over sloping terrain (stratification across terrain).
- Coupling with return circulation in the jet streak.

Presented here are the most relevant definitions for low level jets for this thesis. (For a better history of the definitions, study conducted by Kalverlaa *et al.*[20] is recommended). Kalverlaa *et al.* presents a consolidation of most commonly used definitions for low level jets. Two of these definitions are presented here.

First: Reduced friction in the evening causes wind to accelerate on top of the decoupled layer. Under the influence of solar insolation during the day the sensible heat of the surface increasing U_*, friction velocity. To explain this, recall the definition of friction velocity, as the ratio of shear experienced by a fluid element to the local density, as provided in the equation: 2.9.

$$U_* = \sqrt{\frac{\tau}{\rho}} \tag{2.9}$$

The increase in heat causes (per ideal gas equation) a decrease in density of the fluid. This decreased density causes friction velocity to increase. Heat flux is drastically reduced due to no source(solar insolation) at the night, causing radiative cooling leading to the formation of a stable stratification, decoupling the atmospheric layers. The reduced friction in the decoupled layer causes an acceleration of the flow due to the Coriolis effect on the decoupled layer causing wind speed to be higher than the geostrophic wind speed leading to the formation of a low level jet (LLJ). The sudden increase in wind speeds will have oscillation across the geostrophic wind profile, in order to achieve equilibrium. The time period of oscillation is as given in the equation: 2.10.

$$T = \frac{2\pi}{f} \tag{2.10}$$

Where f is the Coriolis parameter dependent on the latitude. This theory is put forth by Blackadar[21]. This is better visualized by a figure presented in the study by Malcher *et al.*[22], figure: 2.3. Please note time is presented here in 24 hour format on the wind profiles. The study was performed to understand the evolution of LLJ, presented here are simulation results and not the observed data. Inferring from the representation, at 18:00 (near sunset) there is no sign of the formation of an LLJ, it starts to form at 21:00 and matures at 00:00 then oscillates to 06:00, this oscillation is called inertial oscillation. This study is mainly for a land evolved LLJ, it has been hypothesized a land evolved LLJ could advect to the sea, the reduced surface friction from land to sea will again cause an increase in the wind speed, making LLJ advecting from land to the sea a very

interesting phenomena. A study conducted by Dörenkämper *et al.* [23] simulates such a scenario using large eddy simulation at FINO1 - met mast near the coast of Borkum, Germany, in order to understand the effect on loading caused by a land advected LLJ.

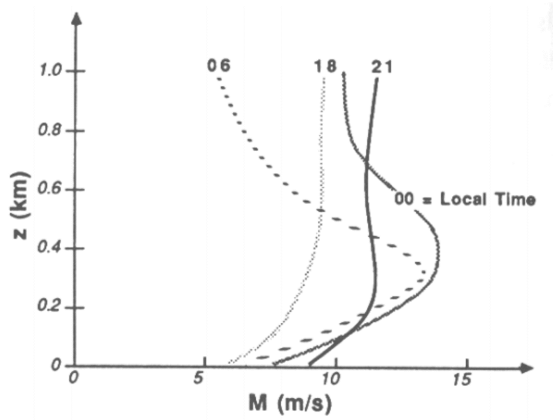

Figure 2.3: Formation of LLJ over time.

Second: Similarly Warm air advecting over colder air would also cause an increase in wind speeds concurring to the same mechanism due to reduced friction from the cooler air. A local stratification of stable boundary layer is formed. The formation of such a stratification is observed over valleys and mountain passes during the day heat flux from the surface causes a mixed layer in the atmospheric boundary layer, during the night (recall surface cools faster than the atmosphere) the gradient of the mountain pass and lack of a mixed layer will simulate warm air(from the atmosphere) advecting over colder air(near the surface).

With multiple definitions, many ways of identify a LLJ from observed data have been defined, a consolidation of which is presented in the study by Kalverla[20] and the references therein. The study uses the definition of LLJ as the difference between the lowest maximum wind speed and the subsequent minimum is at least 2m/s or 25% of the maximum. Inferring from the study by Park *et al.*[18] a high shear coefficient can also be used to identify a possible low level jet. Therefore an approach involving both the theories is chosen for data analysis in this research. It must be noted that Karverlaa *et al.*'s study also presents a very interesting Venn diagram of the percentage of the 95^{th} percentile of the LLJ events with 95^{th} percentile shear and and 95^{th} percentile veer. This has been presented in the figure: 2.4. The numbers in the sets represents the percentage of total data above the 95^{th} percentile limit.

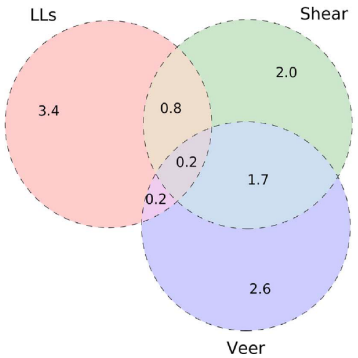

Figure 2.4: A Venn diagram depicting the correlation between the 95^{th} percentile data of LLJ with shear and veer, the numbers represent the percentage of data from the met mast Ijmuiden.

In order to model a low level jet, computationally expensive mesoscale models such as Weather Research and Forecasting (WRF) are used in combination with re-analysis data-sets such as ERA-Interim, ERA-5, MERRA, to name a few. For the scope of this thesis WRF model is used to recreate a low level jet in the past using ERA-Interim data-set, said models will be discussed further in the chapter: Model description. To

reduce computational costs an intermediate site-specific synthetic turbulence model is defined, the general literature of spectral equations (synthetic turbulence model) is presented in the following section.

2.3. Search for a universal spectral equation

Since the development of the first computational fluid dynamic (CFD) model over a century ago for modelling turbulence and predicting fluid flow, emerged an alternate to experimentation. This further enhanced improvement in our understanding of flow phenomena, and in certain cases the only way to understand flow phenomena. For example, recording meteorological data using met masts (Meteorological masts) is a difficult and expensive process, involving technological challenges such as being able to record data either at single point in space (cup or sonic anemometers) or for a fixed range (Light Detection and Ranging (LiDAR) and Sonic detection and ranging (SODAR)), met masts also pose high costs of maintenance for the instruments on board. Reliability and post processing of recorded data is also a challenge in the field, giving rise to interesting research scopes. Kettle[24] proposed the presence of internal boundary layers observed from FINO-1's data. With the recorded data spectral equations can be determined for a particular location, generalizing the turbulence for that location. With rising heights in wind turbines the height of atmospheric boundary layer that is in contact with the wind turbine is also increased, thus height of the met masts to also increase. Theories developed based on shorter met masts need a revamp for example, deviations in wind profile from MOST theory at low heights have been observed in literature[25]. Existing spectral equations such as Kaimal spectrum are once thought to be a universal spectral equation also needs a revamp considering the new heights of the wind turbine and variable stability of the atmospheric boundary layer.

Described in this section are the definitions and basics of understanding and visualizing a spectral equation used in the field of wind energy. This chapter aims to simplify to visualize basics definitions of spectra, coherence, and also demonstrates on how to model a wind field using spectral equations.

2.4. Basics of a spectral form

A met-mast is capable of measuring wind speeds and other meteorological parameters such as wind direction, temperature, moisture, etc based on instrumentation on board. The resulting data is a time series in one dimension, for example 10-minute averaged wind speed recorded over time. The sampling frequency (measuring frequency of the instrument) is defined by the time scale of the lowest energy carrying eddy that is relevant to the application, in general 20Hz is the recording frequency for wind speeds. Measurements are generally averaged over a period of time to reduce variance from mean following spectral gap [26], that is 10 minutes. Recorded data (or a time-series) is non-periodic in nature making the relevant mathematical models complex. Using Fourier transform a signal varying in time can be deconstructed into a combination of sine and cosine waves with various amplitudes and frequencies. A video[27] by dr. Eugene Khutoryansky describes this in a simplistic way providing brilliant visual explanation of the much used function. The resulting transformation in the frequency domain gives an estimate of power present in the signal (power spectral density) Using Fourier transformation techniques such as Welch P.D method[28] one can find the power spectral density of recorded wind data (Note: this function is pre-coded in MATLAB).

It must be noted that one spectral equation can represent multiple time series for a give frequency content or energy. Figure: 2.5 presents a schematic of Fourier transform.

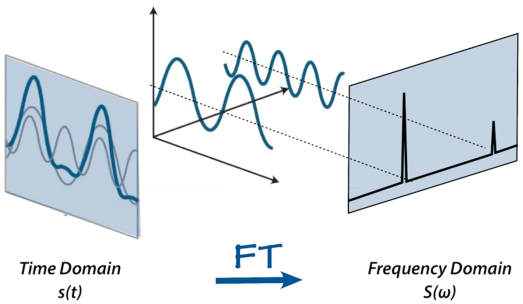

Figure 2.5: A schematic of Fourier transformation

In the field of wind energy, a study published by Henry W. Tieleman on the universality of velocity

spectra[29] in 1992 proposed a unified spectral model for wind velocity in three components. The paper goes on to present two generalized models for spectra: "Blunt" and "Pointed". Blunt model refers to velocity spectrum derived from a flat, smooth and uniform (FSU) terrain. Pointed model is derived from a complex terrain. The study considers a near-neutral atmospheric condition for the spectra proposed. A general form of a velocity spectral model as proposed by the study is presented in the equation: 2.11. The coefficients A and B are defined based on length scale and other boundary layer parameters. To visualize the coefficients control the position of the spectra in a frequency range plot(Energy vs logarithm of wave number). The exponents $\alpha and \beta$ denote the shape of the spectrum (the slop), various studies have been conducted in order to estimate site-specific coefficients for this equation (refer [29] and the reference therein). For a near-neutral condition and blunt model (FSU terrain) $\alpha and \beta$ take the values 1 and $\frac{5}{3}$ and vice versa for a pointed model (Complex terrain).

$$\frac{nS_a(n)}{U_*^2} = \frac{Af}{(1+Bf^{\alpha})^{\beta}} \tag{2.11}$$

The Kaimal spectrum was estimated from extensive field study in order to estimate the wind spectrum, per Tieleman the proposed was a blunt model in both u and v components and pointed model in w component. Components u and v are more influenced by the upwind terrain characteristics, representing a FSU terrain, pointed model is considered for w component. Both Blunt and Pointed models capture what is known as a "spectral peak", this was also discussed in the paper by Van der Hooven on the existence of a spectral gap. The schematic: 2.6 as presented in the book Atmospheric Boundary Layer Flows: Their Structure and Measurement[30] provides a better visualization of a spectral peak.

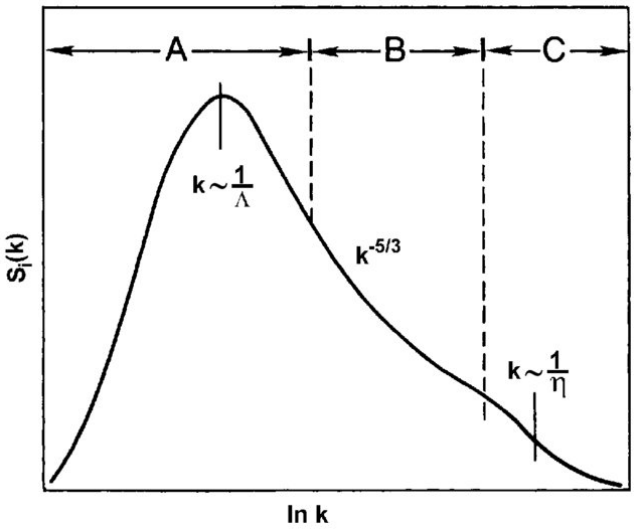

Figure 2.6: Schematic of energy spectrum in the atmospheric boundary layer showing distinct regions of energy production (A) and dissipation (C) and the inertial subrange (B), where both energy production and dissipation are negligible. A is the integral scale of turbulence and η is the Kolmogorov microscale[30]

The value Λ here represents the integral length scale. Plot description: y-axis refers to the power spectral density (can be obtained using Welch's method), the logarithmic x-axis present the wave number. The region A represents the energy production region of the atmospheric boundary layer(slope of the curve is +2), with the integral length scale defined at the peak, energy generation is dominated by solar insolation. The length scale of the atmospheric boundary layer is a very important parameter that is used in the modern day fluid mechanic simulations. The integral length scale is defined by the equation: 2.12.

$$l_0 \propto \frac{k^{2/3}}{\epsilon} \tag{2.12}$$

The region denoted as "B" refers only to energy transfer from larger eddies to the smaller eddies, therefore dissipation of energy is considered negligible (the curve the -5/3 slope), it must be noted that viscosity, ν is not a driving factor for turbulence in this region(Kolmogorov's hypothesis). This is defined as the energy cascade mechanism. Region "C" denotes the inertial subrange, representing heat dissipation of small through

viscosity and heat. Here smaller eddies feed off energy from larger eddies, paraphrasing the quote by Lewis Fry Richardson: “Big whirls have little whirls, That feed on their velocity; And little whirls have lesser whirls, And so on to viscosity.” This dissipation is a continuous function[31]. This observed spectrum is quantified using Kolmogorov’s hypothesis for the inertial subrange.The equation: 2.13 presents the same.

$$S(\kappa) = C\epsilon^{2/3}\kappa^{-5/3} \tag{2.13}$$

C is the Kolmogorov’s constant experimentally determined as 1.5. In order to calculate the length scale without the influence of large scale phenomena such as gravity waves, meteorologists make use of the spectral gap [26] and the forms of equations as presented in equation: 2.14 and equation: 2.15[30].

$$\frac{\kappa_1 F_\alpha(\kappa_1)}{\sigma_\alpha^2} = \frac{A(\kappa_1/\kappa_{1m})}{1 + B(\kappa_1/\kappa_{1m})^{5/3}} \tag{2.14}$$

$$\frac{\kappa_1 F_\alpha(\kappa_1)}{\sigma_\alpha^2} = \frac{C(\kappa_1/\kappa_{1m})}{[1 + D(\kappa_1/\kappa_{1m})]^{5/3}} \tag{2.15}$$

Where, α represents the component of wind; u,v,w. Constants A, B, C, D are adjustable constants derived from observational data, and the subscript m denotes κ_1 at the spectral peak (subscript 1 represents wind component u). Either equation is chosen based on which fits the observed data better for example, equation:2.14 fits unstable w spectra and all stable spectra and equation: 2.15 fits unstable u and v better.

2.5. Wind field modelling - Kaimal spectrum

Using a met-mast to record wind speeds at the site of interest a spectral equation is formulated. The resulting spectral equation is assumed to be constant with height. Using a mean wind profile, the spectral equation can add turbulence to the assumed profile. An example of modelling a wind field using spectral equation is presented in following section. Here IEC-Kaimal spectrum and the IEC coherence model are taken into account.

2.5.1. Step: 1 - Spectral equation: IEC-Kaimal Spectrum

Developed by Kaimal *et al.* from extensive field work and observed data gathered from a met-mast of height 32m installed at flat, uniform site in Kansas, USA, led to the proposal of spectral equations as a function of the length scale, the local mean velocity and the local variance (measurable quantities). The development of this model in 1968[4] marked an empirical spectral equation that would be followed to this day in the field of Wind energy. The equation: 2.16 presents the Kaimal spectrum as defined by IEC for wind components denoted by k:$\{u, v, w\}$

$$S_k(f) = \sigma_k^2 \frac{4\frac{L_k}{U}}{(1 + 6f\frac{L_k}{U})^{\frac{5}{3}}} \tag{2.16}$$

where L_k is the integral scale length, for $k == u; L_k = 8.1 \cdot min(60m, Hubheight)$ (please refer IEC standard 61400-ed3[15] for definitions of other components), f is the frequency in hertz, U is the hub height mean wind speed and σ_k^2 is the variance. The equations are plotted in the figure: 2.7. The plot is a normalized Kaimal spectrum in reference to the friction velocity and magnitude of wind speed in y and x axes respectively. The peak in the spectrum denotes the area with maximum energy. "i" refers to the component of wind speed.

The lower end of the frequency range is the production region for large eddies in the atmosphere, generated by the relative motion between the free-stream gradient flow and the stationary air near the ground, feeding energy to the turbulence and solar insolation. The higher end of the frequency range is considered purely for energy transfer(refer figure: 2.6 for a better explanation). In theory, the spectrum was developed under near-neutral conditions however was extended to the assumption; effects of atmospheric stability induced variation on the spectral equation as a function of the area under the curve or the total variance can be assumed negligible[32], making this a universal relationship. However as explained in the earlier section significant variation has been observed consequently leading to the proposal of Cheynet *et al.* spectral model.

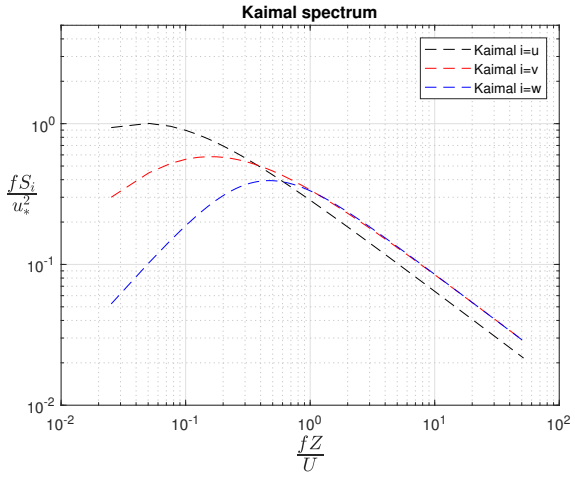

Figure 2.7: Kaimal spectrum for an arbitrary frequency range

2.5.2. Step: 2 - Coherence function

Two waves in space are considered perfectly coherent if the waves have the same phase, frequency and waveform. In order to model a wind field the correlation of velocity components in space has to be known, rephrasing the coherence of the velocity components in the frequency domain. Coherence function for velocity components is defined for spatial separation smaller than a typical length scale. The general formulation for finding the coherence between two points in space is a function of the cross power spectral density between the two points and the power spectral density about that point. Equation: 2.17 presents the general form for coherence.

$$Coh_{i,j}(f) = \frac{|S_{ij}(f)|}{\sqrt{S_{ii}(f)S_{jj}(f)}} \tag{2.17}$$

Where S_{ij} represents the cross power spectral density betweent the points i and j as a function of the frequency f, S_{ii} and S_{jj} represent the power spectral density at the points i and j given by the equation: 2.16 as a function of frequency. Several coherence models have been proposed in the field of wind energy. In this thesis, two coherence models have been used, namely, IEC coherence model and Davenport coherence model. Firstly the Davenport model, as proposed by Davenport is discussed. The model is presented in equation: 2.18. The model assumes an exponential function for coherence.

$$\gamma_i(z_1, Z_2, n) \approx \exp\Big(-\frac{C_1^i n|z_2 - z_1|}{\frac{1}{2}[\overline{u}(z_1) + \overline{u}(z_2)]}\Big) \tag{2.18}$$

Where, z_1 and z_2 are two measurement heights in space, i = $\{u,, v, w\}$, C_1^i is the decay coefficient and n is the frequency. The decay coefficients are sensitive to site location and measurement conditions; spatial separation, measurement height, the mean wind speed, atmospheric stability, angle between wind direction and the measurement instrument (lateral coherence), turbulence intensity and wind shear. Cheynet *et al.* proposes a modification to the equation to mitigate the dependency of the spatial separation on coherence, with two decay coefficients, the given in equation: 2.19.

$$\gamma_i(d_z, n) \approx \exp\Big\{-\Big[\frac{d_z}{\overline{u}}\sqrt{(c_1^i n)^2 + (c_2^i)^2}\Big]\Big\} \tag{2.19}$$

Where d_z is the separation, n is the frequency c_1^i and c_2^i are the decay coefficients, $\overline{u}$ is the mean wind speed. The decay coefficients are dependent on the stability parameter ζ, one such equation is presented: 2.20.

$$c_i^u = 11.0 + 1.8\exp(4.5\zeta) \tag{2.20}$$

Where c_i^u is the decay coefficient for the u component in the i^{th} direction - either x, y or z. It must be noted that the equation: 2.20 is derived from FINO - 1 data-set as used in the study conducted by Cheynet *et al.* Equations for v and w components of the wind are presented in the study.

The IEC coherence model[15] is a modification of the Davenport coherence model and is originally derived for an onshore environment, later was extended to offshore. The equation: 2.21 presents IEC coherence model.

$$Coh_{i,j} = \exp\left\{-a\sqrt{\left(\frac{fr}{\overline{u}_{hub}}\right)^2 + \left(0.12\frac{r}{L_c}\right)^2}\right\} \tag{2.21}$$

where f is the frequency, r is the distance between points i and j on the grid, a is the coherence decrement, $\overline{u}_{hub}$ is the mean hub-height wind speed, and L_c is a coherence scale parameter, the parameters a and L_c are constants (based on standard used, presented here for edition 3) presented in equations: 2.22 and 2.23.

$$a = 12 \tag{2.22}$$

$$L_c = 5.67 \cdot min(60m, Hubheight) \tag{2.23}$$

The equation: 2.21 is defined only for the u component of wind, IEC defines coherence for v and w components as presented in equation: 2.24

$$Coh_{i,j} = \begin{cases} 1 & i = j \\ 0 & i \neq j \end{cases} \tag{2.24}$$

Both coherence functions are used in the project and will be discussed in the chapter: Model description.

2.5.3. Step: 3 - Wind field generation

For the generation of a wind field, the resulting spectrum at each grid point considering coherence must be known, here the code published by Etienne Cheynet[33] is used to calculate the same. The equation: 2.17 is used to calculate the resulting spectrum. The code is modified to in corporate IEC and Davenport coherence model as presented in equations: 2.21 and 2.18, respectively.

2.6. CJR model

Having defined the basics of a spectral form this section presents the applicability of these equations in the field of wind energy and their improvements. In a recent study an intermediate "spectral plateau" following a -1 exponent in the surface layer has also been indicated by Drobinski *et al.*; on the Numerical and experimental investigation of the neutral atmospheric surface layer[34]. It was later found the existence of spectral plateau at higher heights refer Cheynet *et al.*[13] and the reference therein. An example of a spectral plateau is plotted in the figure: 2.8 (the dip at lower frequencies is the spectral plateau) (note, CJR stands for Etienne Cheynet, Jasna B. Jakobsen, Joachim Reuder). The study conducted by Cheynet *et al.* aims to put forth site specific, spectral equations and davenport coherence function for FiNO - 1 metmast. Methodology followed for this study includes curve-fitting a general spectral equation based on observational data.

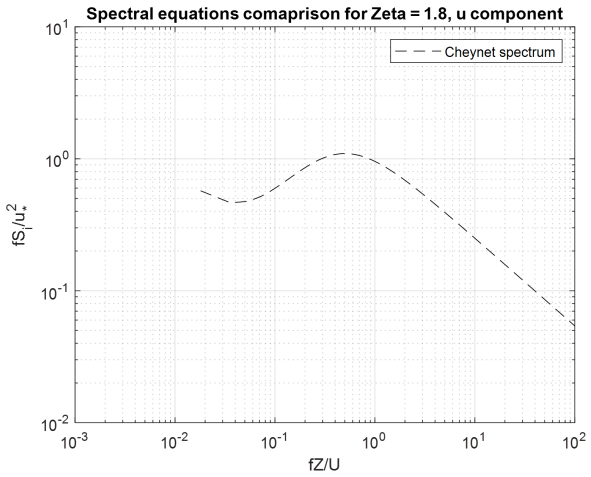

Figure 2.8: Plotted the u-component CJR spectral model for an arbitrary stability value of 1.8.

The general form of the spectral equation capable of producing this observed spectral plateau must satisfy two conditions[35]:

- Approximations to both pointed and blunt models.
- Both u and w component must have the same spectral equation.

The spectral form achieving these conditions is called "Pointed-Blunt" model(as called by Cheynet *et al.*). Equation: 2.25 represents its form.

$$\frac{nS_i}{U_*^2} = \frac{a_1^i f}{(1+b_1^i f)^{\frac{5}{3}}} + \frac{a_2^i f}{(1+b_2^i f^{\frac{5}{3}})} \tag{2.25}$$

This equation is further modified to incorporate stable and unstable stratification. Basing on observed data, a spectral gap is found as well as other mesoscale fluctuations it was observed the sub-range identified followed -2 and -2/3 scaling per frequency that is $a_3 f^{-2}$ and $a_4 f^{\frac{-2}{3}}$ terms would be added to the general equation mentioned:2.25. The paper assumes to then consider mesoscale fluctuation to be dominant for simpler modelling. Equation: 2.26 presents the final spectral equation.

$$\frac{nS_i}{U_*^2} \approx a_3 f^{-2} + \frac{a_2^i f}{(1+b_2^i f^{\frac{5}{3}})} + c_1 f^{\frac{-2}{3}} \tag{2.26}$$

The study estimates the coefficients by curve fitting the spectrum of observed data for various stability parameters, in the study the stability range of -2 to +2 is considered. The term i in the equations represents the velocity components. Algorithmic developed by the study is programmed to select the most suitable equation of Eqn: 2.25 and Eqn: 2.26 for a given velocity component. The fitted coefficients for the component u are presented in the paper, coefficients received from the artist are presented in Appendix - A.

3

Data analysis

This chapter describes the methodology followed to identify LLJ phenomena from a meteorological met-mast, FINO 1. Following sections include description of the met-mast, methodology followed for LLJ identification and results and validation of the methodology.

3.1. FINO 1 met-mast

Meteorological data used in this research is acquired from the research met-mast, FINO - 1[14]. The meteorological data-set consists recordings of wind speed, wind direction and temperature measurements. The FINO - 1 met-mast equips; 8 anemometers and wind vanes at heights ranging 33m, 40m, 50m, 60m, 70m, 80m, 90m and 100m, temperature sensors at heights 33m, 50m, 70m and 90m, high-resolution UltraSonic Anemometers (USA) at 40m, 60m and 80m. The location of the instruments is depicted in figure: 3.1[36]. The met mast is relatively close to the shore, about 45km off the coast of Borkum, Germany. This research utilizes wind speed and wind direction data from the year 2004 to 2012 for data analysis. It must be noted that observational data from "100 meter" anemometer has been ignored, as it has been found to have errors in measurements. Wind speeds in the range of 5m/s to 30m/s have been considered for this research, Being the operational range of a wind turbine.

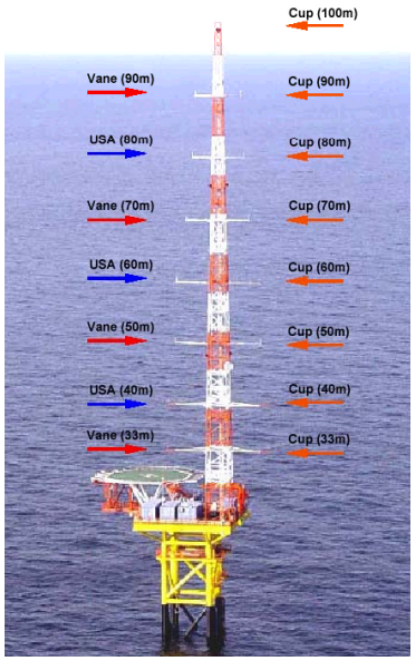

Figure 3.1: FINO-1 platform north sea

3.2. Methodology

Methodology followed for data analysis in this thesis is fairly simple, firstly power law (using equation: 2.1) fit is used to extract the shear exponent, α. Second, filters on the shear exponents were instated; negative shear coefficient was filtered to the range of 0 to -4, positive shear coefficient was filtered between 0 and 0.8 to avoid possible measurement errors. Finally, the resulting data-set's 95^{th} and 5^{th} percentile is chosen as the threshold to select dates for further simulations. Plots for the 95^{th} and 5^{th} percentile for wind shear exponent are presented in figure: 3.2. The threshold values (95^{th} and 5^{th} percentile) for shear coefficient are $[0.33, -0.12]$. The resulting data-set includes only the dates with α beyond the thresholds described above.

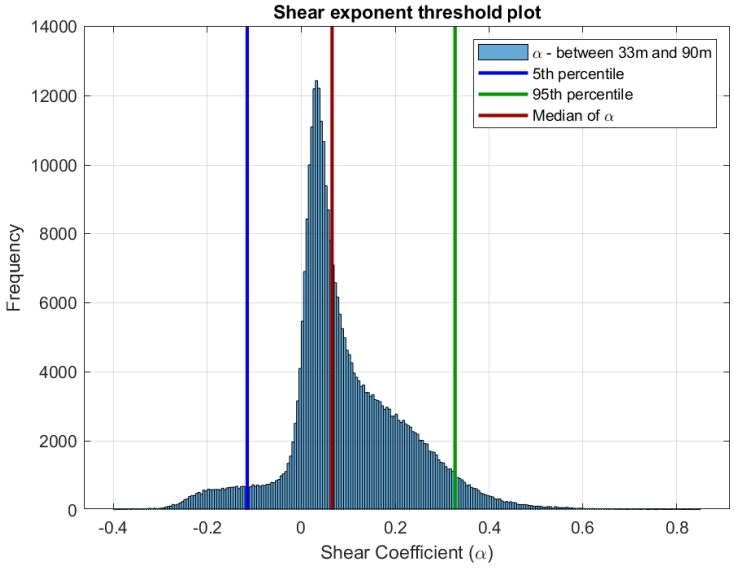

Figure 3.2: Histogram depicting the distribution of shear exponent α, 95^{th} and 5^{th} percentile thresholds and median of α (=0.066). 95^{th} and 5^{th} percentile for shear coefficient are $[0.33, -0.12]$.

Similar procedure is selected for the wind direction as well. A wind direction bin of 120° was chosen for the purpose of mast correction[37]. Difference in wind direction (wind veer, β) is calculated between 33m and 90m wind vanes. Figure: 3.3 presents the resulting distribution of the wind direction along with the 95^{th} and 5^{th} percentile thresholds. The values for the same are $[13.6°, -8.0°]$.

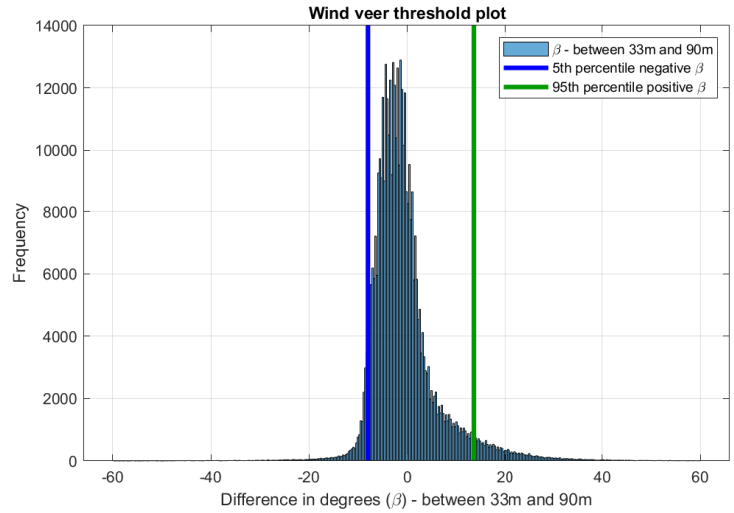

Figure 3.3: Histogram depicting the distribution of wind veer, β, 95^{th} and 5^{th} percentile thresholds.

In order to estimate an anomalous event the two data-sets for wind direction and wind shear (involving four threshold values) were then correlated with each other in combinations considering the 95^{th} percentile threshold. The resulting data-sets explored considering identified thresholds as limits are; *threshold shear events*: data-set including dates with $\alpha > 95^{th}$ percentile value, *threshold shear and veer events*: perfectly correlated data-set including dates with α and $\beta > 95^{th}$ percentile threshold, *threshold negative shear and veer events*: perfectly correlated data-set including dates with $\alpha < 5^{th}$ percentile value and $\beta > 95^{th}$ percentile value, similarly for *threshold negative shear events*, and *threshold veer events*. Consolidation of the data-sets and their attributes is presented in table: 3.1. The 5^{th} percentile value of β has been neglected in identifying data-sets in this research due to low wind speeds concurring to the event.

#	Data-set	Attribute
1	Threshold shear events	$\alpha > 95^{th}$ percentile threshold
2	Threshold shear and veer events	α and $\beta > 95^{th}$ percentile threshold
3	Threshold negative shear and veer events	$\alpha < 5^{th}$ percentile threshold and $\beta > 95^{th}$ percentile threshold
4	Threshold negative shear events	$\alpha < 5^{th}$ percentile threshold
5	Threshold veer events	$\beta > 95^{th}$ percentile threshold

Table 3.1: Presents the data-sets explored from eight years of observational data.

The resulting five data-sets are then sorted based on the number of occurrences the event. Highest occurrence being the most prominent event (unlikely to be a measurement error) thus selected as a case of interest. Figure: 3.4 presents an example of one data-set "threshold shear events" ($\alpha > 95^{th}$ percentile threshold), x axis presents the number of days with $\alpha > 95^{th}$ percentile threshold and the number of occurrence of threshold shear on the particular day on y axis, lower number of occurrence of the event concurred to a lower consistency of the event. Therefore, events with very high occurrences are better suited for further analysis.

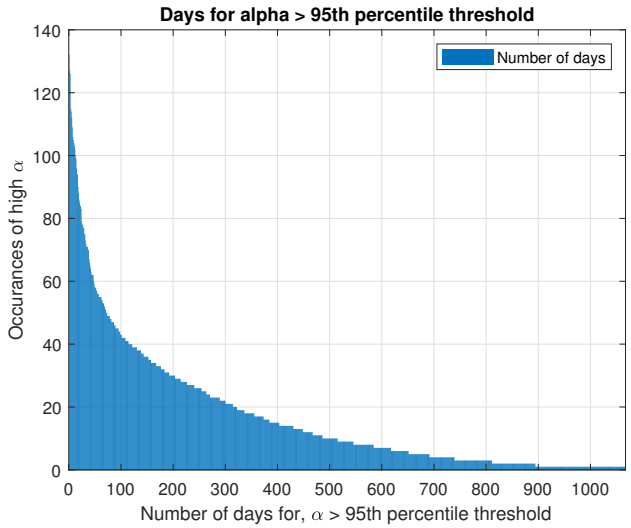

Figure 3.4: Histogram of threshold wind shear events for days of years from 2004 to 2012 filtered based on 95^{th} percentile value of the shear coefficient.

Data of the type presented in the figure: 3.5 has also been ignored, as these were found to be unrealistic, and possible measurement error, also would be a challenge to simulate using a mesoscale model such as WRF.

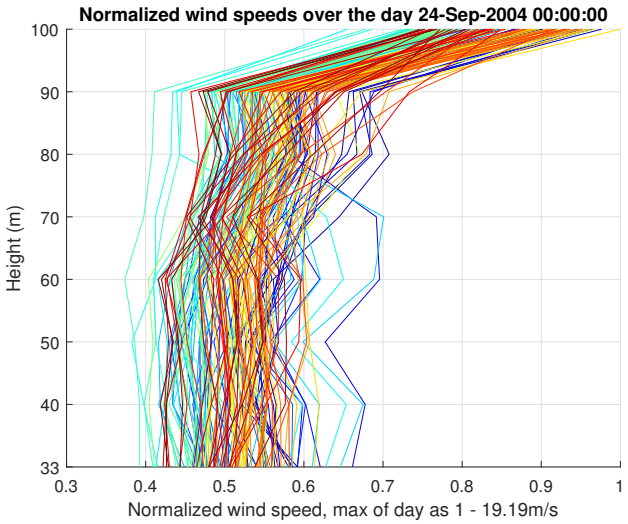

Figure 3.5: Example of a kinked profiles at FINO 1, presented data is an example of ignored dates. Here wind speeds are normalized with respect to the maximum wind speed for the day to understand the profiles over the time of 24 hours.

The advantage of segregating observational data into five unique data-sets lies with the simplicity of working with prominent atmospheric events that have a greater possibility of being reproduced by WRF and to simplify the data analysis by reducing overall data-set(eight years of data) into relevant smaller data-sets. Some statistics of eight years observational data indicate, 32.4% "threshold shear events", 3% "threshold shear and veer events", 6.3% "threshold negative shear and veer events", 25.2% "threshold negative shear events" and 36.1% "threshold veer events" (please note the summation of the percentages cannot be 100% as there are overlapping events).

Baas *et al.*'s criteria[38] for identifying an LLJ is one of the ways to identify a LLJ, In this thesis a visual method is chosen, considering an inference from Kalverla *et al.*'s study, particularly the figure: 2.4, it is observed that 40% of 95^{th} percentile values of high shear event demonstrated a low level jet, similarly 10% of 95^{th} percentile values of high veer event demonstrated a low level jet. Therefore considering these criteria and the mentioned data-sets subsequently led to the identification of three events as presented in the table: 3.2. Of the many events that were identified with this process involving combinations event attributes, only three dates are chosen in the interest of simplicity and computational time considering WRF.

3.3. Results and discussion

The resulting selection of dates is presented in the table: 3.2. It must be noted that the list and the details provided within are solely from data analytics and are used as a reference to select a day for simulation. A well-compiled mesoscale simulation of the selected dates will determine which part of the day can be used for further analysis (wind field generation and loading using FAST, this is further explained in the chapter of case studies). This decision has been taken considering high computational costs that would incur to simulate difficult scenarios requiring higher resolution of grid.

#	Date	β	α	Description
1	02-Jul-2006	17° ~31°	-0.12 ~-0.22	Low level jet
2	23-May-2012	~4°	>0.31	Low level jet
3	14-April-2004	>25°	>0.30	Low level jet

Table 3.2: Table presenting the final selection of dates and events that will be simulated.

To understand the results in term of their behaviour and meteorological phenomena, individual time vs height plots and wind profiles plot for the day are presented in the figures: 3.6, 3.7, and 3.8. Please note the color scheme for the wind profiles ranges from day to night as red to blue, that is red profiles represent day profiles and blue referring to the night profiles, the span of the day covers the colors within this range, in the sequence of red - green - blue (day-afternoon-night).

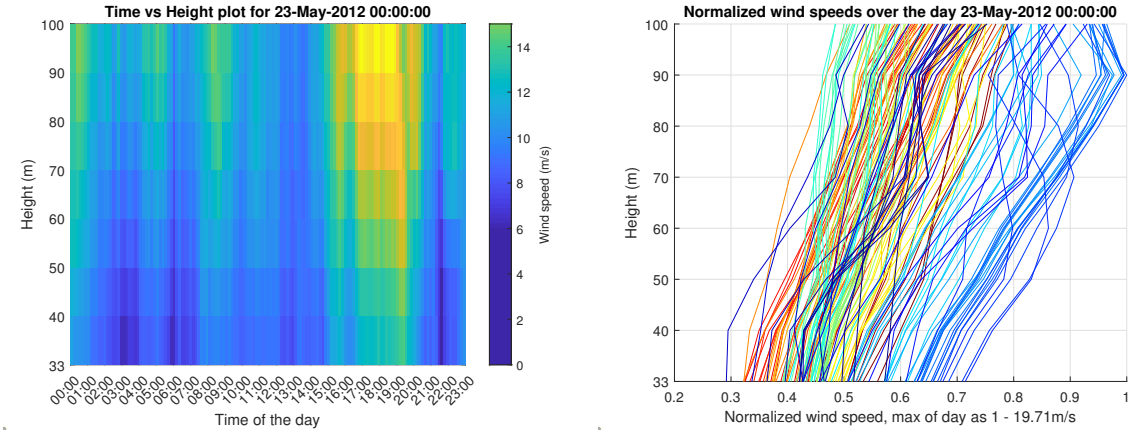

Figure 3.6: Starting from the left, plot of observed data at FINO 1 for the date 23^{rd} May 2012 and plot of wind speed profiles normalized over the day.

Inferring from plots and data analysis; formation of a evening LLJ occurring from 16:00 - 20:00 on the 23^{rd} May 2012 is evident from the time vs height plot presented in the figure: 3.6 (from left). α during the range is approximately 0.4 that is greater than threshold value (0.33). In order to understand the atmospheric phenomena that could influence the jet's formation, pressure contour plots for this day from reanalysis achieves available in [39] are utilized, contours indicate no specific meteorological event for the occurrence. It would be interesting as to identify the source of this jet, as this is not the focus of the thesis, it will not be studied here. Figure: 3.6(right) is plotted to ensure no occurrences of a kinked profile in the observed data and to visualize the change in wind profile over time starting from the indicated time in title.

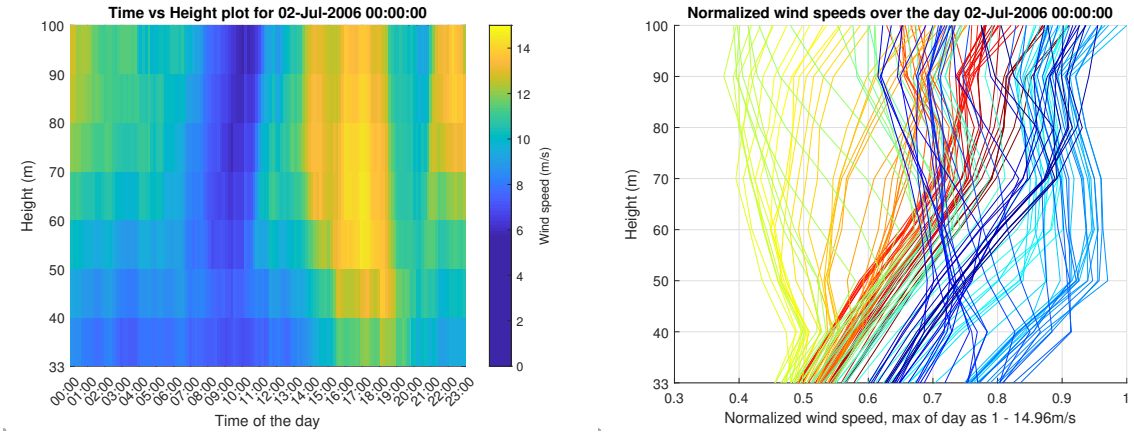

Figure 3.7: Starting from the left, plot of observed data at FINO 1 for the date 2^{nd} July 2006 and plot of wind speed profiles normalized over the day.

Formation of an evening low level jet at 14:00 - 19:00 on the 2^{nd} July 2006 is evident from the time vs height plot presented in the figure: 3.7. This case was chosen to based on a threshold negative shear and veer event, a consistent negative α is observed during the morning from 09:30 to 11:00; -0.13 to -0.22. However, the wind speeds during this time, although within the operating range of a wind turbine, are lower than wind speeds during the evening 14:00 to 19:00, making this a more interesting case study from a LLJ point of view. α during the evening range is approximately 0.15 to -0.15, that is lesser than the negative shear threshold value (-0.12) from 19:00. Judging from the time vs height plot, the evening jet is better case study, consisting of higher wind speeds. Figure: 3.7(right) is plotted to ensure no occurrences of a kinked profile in the observed data and to visualize the change in wind profile over time starting from the indicated time in title. Observing the pressure contour plots for this day from reanalysis achieves available in [39] indicate the presence of high pressure to the north of FINO - 1 and a strong low pressure to the south, this pressure difference is likely to be the cause of this low level jet.

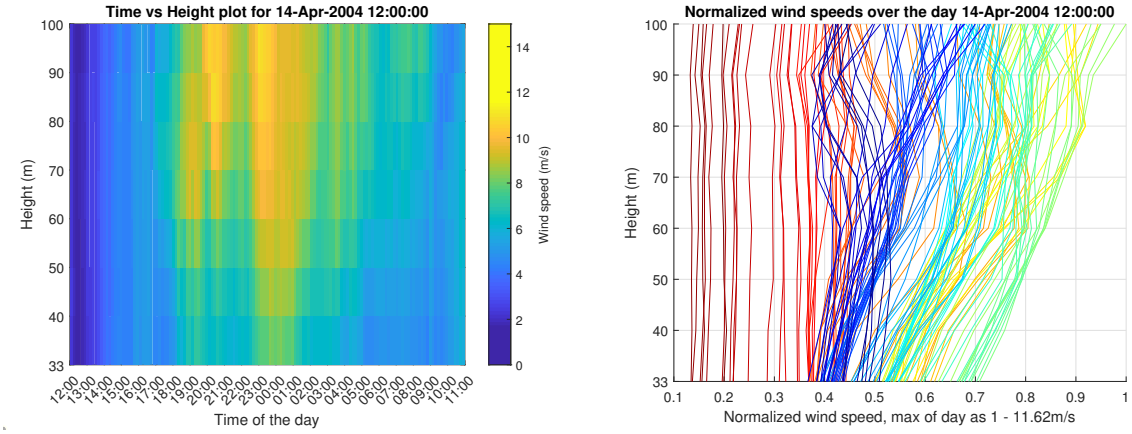

Figure 3.8: Starting from the left, plot of observed data at FINO 1 for the date 14^{th} April 2004 and plot of wind speed profiles normalized over the day.

This case is observed to be a three day consecutive event, starting 14^{th} April 2004 to 16^{th} April 2004. With low level jets occurring on all three days. For simplicity of the model one event occurring over 2 days 14^{th} April and 15^{th} April is selected for simulation. This is pertaining to high wind speeds, high shear and high veer for this event. Inferring from time vs height plot refer figure: 3.8(from left), the event starts at 20:00 on the 14^{th} and ends at 01:00 on the 15^{th}. α observed is approximately between 0.3 to 0.6 (greater than 95^{th} percentile shear threshold of 0.33), and is consistent from 20:00 to 23:50. Wind veer, β is also higher than 95^{th} veer threshold of 13.7° observed to vary from 10° to 26° over time. Observing the pressure contour plots for this day from reanalysis achieves available in [39] indicate the presence of a possible cold front. Figure: 3.8(right) is plotted to ensure no occurrences of a kinked profile in the observed data and to visualize the change in wind profile over time starting from the indicated time in title. Note: plots for trend of change in wind speeds through the day and histogram over one year observing dominant months crossing 95^{th} percentile wind shear exponent presented in Appendix A.1.

4

Model framework

This chapter presents the methodology followed, computational challenges and detailed explanation of the model framework proposed for simulating a wind field considering the wind profile of a low level jet, in order to re-create "near-realistic" wind field depicting a low level jet that can be used to understand the effects of low level jets on wind turbine loading and low computation method of wind field generation. Ideally, one could use a mesoscale model such as WRF model to perform an LES simulation to reproduce the wind field of a low level jet derived from reanalysis data-sets, making this a realistic simulation. However, computational cost required for such a project is very high. Here we present in the table: 4.1 a sum up of the computational cost incurred for such a model proposition at different resolutions. It is predicted that a rough estimate of 10,000 processors is needed to create a wind field using WRF-LES. Therefore this being an unrealistic approach the following section presents the model chain proposed considering lower computational cost.

4.1. Model chain

Weather Research and Forecast (WRF) is a mesoscale model used to forecast weather, hindcast weather and to study atmospheric phenomena, in this thesis the model is used to re-create low level jets, identified through the aforementioned data analysis at FINO - 1. The resulting data consisting of wind profile, Obhukov length, surface roughness length and other meteorological data, these are required for the next stage in the model chain. The site-specific spectral model utilizes the spectral equations as presented by Cheynet *et al.* specifically for the location FINO - 1. Modifying a wind field simulator from Mathworks [33] created by Etienne Cheynet a wind field considering parameter derived from WRF is created. Parameters included to the modifications from WRF derived: stability parameter, surface roughness length, friction velocity, magnitude of wind speeds and the resulting wind profile till the maximum grid height of FAST, vertical levels of WRF are used as input to the Site-specific spectral model. The resulting wind field is converted to FAST (Fatigue, Aerodynamics, Structures and Turbulence) readable format, TurbSim standard format ".bts". Which is further used to access the turbine ultimate loading on a 5MW NREL wind turbine. The software is from national renewable energy laboratory (NREL) is widely used in the Wind energy academia and industry. Presented in the following chapters are further explanations of the models, and the changes implemented to complete the model chain. The model framework is presented in the figure: 4.1.

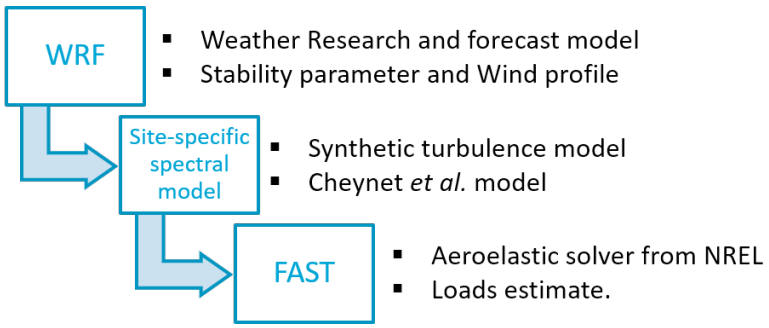

Figure 4.1: Proposed model chain.

4.2. Weather, Research and Forecast

Weather research and forecast model[40] used in this research is an open source mesoscale modelling software, version: 3.9.1.1. WRF is a numerical weather prediction (NWP) designed for both research and industrial applications. The basis of an NWP is to use the state of fluid at a given instant of time and predict the state of the fluid for a consequent instant of time using fluid mechanics and thermodynamic equations. Basic working of an NWP model are presented in the flowchart: 4.2. A NWP model uses observations as the initial state to drive a physics based model (Numerical integration - computable form physics equations using finite element techniques such as constant volume) capable of simulating complex processes in the atmosphere to interpret for forecasts using graphical applications. Against, a conventional model which would create weather maps for a knowledge and experience based forecast. Using WRF, a NWP model weather prediction can be achieved realistically in comparison to a conventional model.

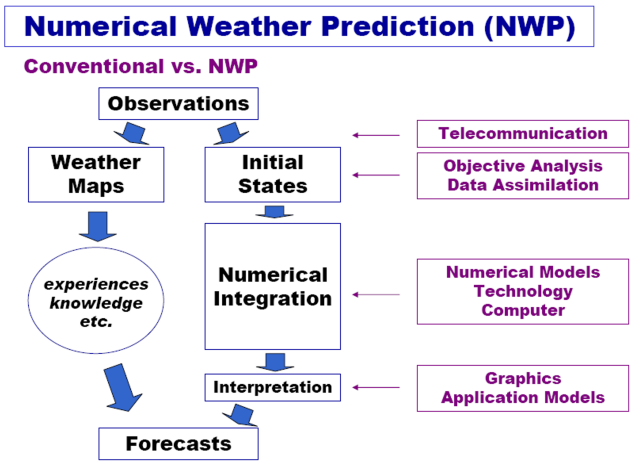

Figure 4.2: Comparison between conventional weather prediction and numerical weather prediction.

A NWP flowchart presented above follows a 5 stage work flow to run an effective mesoscale simulation. Explained here is a very basic view on the framework.

- Starting with observations; WRF model uses either of two data-sets derived from observational data as the initial state of the model. Analysis data and re-analysis data. These data-sets are created using WRF ensembles with observational nudging, the model is run with minimal initial conditions but is nudged by observations over time. An ensemble of such simulations results in data-sets spanning across the globe corrected by observations. WRF model is capable of both, weather forecast and hindcast. For this research hindcast is used, as low level jets occurred in the past are investigated. For hindcast, re-analysis data-sets are applicable.
- Initial state is thus defined by re-analysis data-sets. The data-set is generally of low resolution (grid size of ERA-INTERIM is $\approx$ 30 km) requiring down-scaling for any possible investigation on a wind turbine.
- Numerical integration consists of computable thermodynamic physics and fluid dynamic models to simulate such atmospheric phenomena responsible for down-scaling.
- Resulting simulation requires a graphic user interface model for better understanding of the results for Interpretation and hindcasts.

The software is created and maintained by National Center for Atmospheric Research (NCAR), operated by University Corporation for Atmospheric Research (UCAR). The software is a multi organization next-generation mesoscale forecast and hindcast model for the purpose of better understanding and prediction of mesoscale weather. WRF is a portable code, efficient in a range of computing environments, from laptops to high power computing clusters. Its spectrum of physics and dynamics options are designed to simulate atmospheric phenomena to the highest achievable accuracy. WRF software framework is a cluster of many solvers, including WRF-Chem (air chemistry modelling), WRF-ARW (advanced research WRF) and WRF-Var (variational data assimilation system). For this thesis WRF-ARW for mesoscale modelling, 3.9.1.1 is utilized. The following subsections provide major features, WRF framework and implementation.

4.2.1. WRF-ARW software framework

The model framework for WRF is presented in the figure: 4.3. WRF is a Linux based modelling software coded in Fortran and has minimal graphic user interface (GUI) communication between different stages of the model are via text files. softwares such as WRF Domain Wizard[41] have been explored for a good GUI, however it is not very intuitive and only presents the text files in a GUI manner. Primarily there are two stages in a WRF simulation, WPS and WRF. WPS - WRF pre-processing system, is used to set up the model's domain, initial data and grid for a WRF simulation. Inputs for both WPS and WRF are solely through text files namely; namelist.wps for WPS and namelist.input for WRF. These stages are further explained in the following.

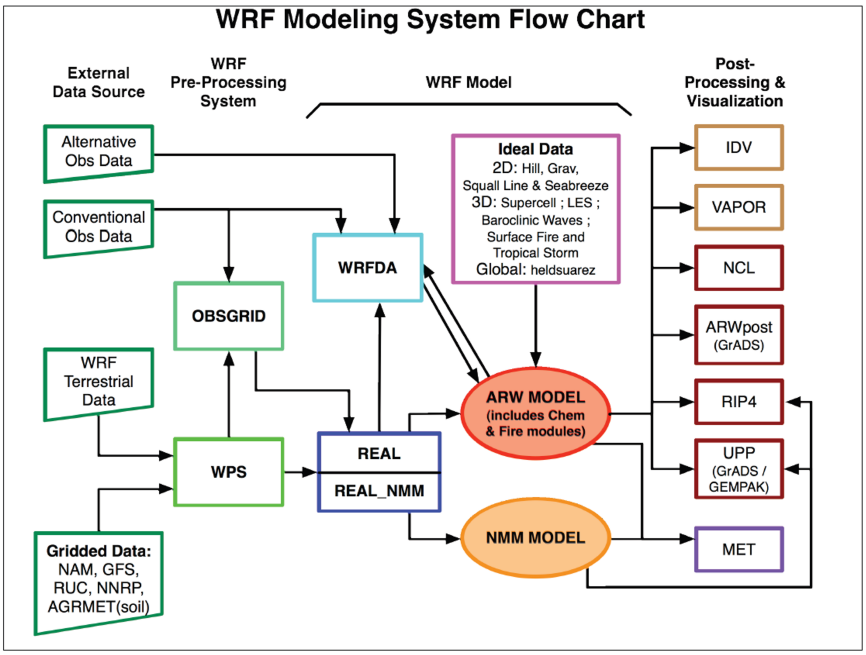

Figure 4.3: WRF modelling framework

Starting from the left of the flow chart;

- *External data source*: Alternate observational data and conventional observational data are not used in this thesis, these data-sets correspond to observational nudging of the model (nudging is the process of utilizing observational data to influence or nudge the simulation into concurrence with observational data). In order to define terrain characteristics of the world in WRF, WRF terrestrial data is used. The data-set is constant through out the simulation, defining the terrain data, soil parameters, albedo, green fraction (vegetation cover), soil type, etc. The data is acquired from [42]. Gridded data represents either re-analysis data-sets or analysis data-sets, presented in the flow chart are the type of data-sets available; NAM, GFS, MERRA, ERA-5, 20^{th} century re-analysis, ERA-interim, etc. Re-analysis data-set, ERA-Interim[43] is used in this research to re-create events from the past. This stage of the workflow defines the data to be used for setting the initial state of the model.
- *WPS - WRF pre-processing system*: External data is extended to WRF pre-processing system to set the grid and initial data for WRF simulation. The system consists of three sub-functions namely: geogrid, ungrib and metgrid. Firstly, geogrid is used to form a 3 dimensional simulation space defined based on domains and grid in namelist.wps, it also translates terrestrial data onto this space. Domains used for the research are presented in the figure: 4.4, location: over FINO - 1. Ungrib converts re-analysis data-set into a readable grid format for WRF. Metgrid interpolates terrestrial data between the horizontal grid points of the domains, as the resolution of the terrestrial data is not the same as the resolution of the grid defined. It must be noted that every domain in the figure: 4.4 consists of a different resolution requirement. With d01 (outer most domain) being the lowest resolution, and d04 with the highest resolution. Refer tables in appendix B.1: B.1 and B.2 for the namelist used.
- *WRF model*: Two sub-functions defined in WRF relevant to this research are discussed here, real and ARW Model (WRF-run). The data from metgrid - WPS is linked to real. Real, interpolates vertical layers

of the grid for the domains defined. Vertical levels can either be defined by the user or let WRF set the vertical layers accordingly. For WRF-run physics and dynamic schemes need to be defined among other parameters; running time, nudging options, restart intervals, I/O variables, etc. These parameters are defined in namelist.input. The WRF model uses physics schemes defined by the user under this file as the settings for the simulation. The namelist used for this thesis is provided in the appendix B.2, refer: B.3 through B.8. Note - "real_NMM" refers to non-hydrostatic model, which is a case of ideal simulation and therefore unused in this research, WRFDA - WRF with observational nudging is also not used in this thesis.

- *WRF post processing*: Post processing and visualization of the resulting simulation is also a challenging feature in WRF. Output files demand high storage requirements, also are stored in an unconventional format, netcdf. Using softwares such as MATLAB is not advisable as the file size is generally too high for MATLAB to handle and coding becomes complex soon. For this thesis multiple softwares for post-processing are used: First, IDV[44] (Integrated Data Viewer) - to visualize the domains actively during setup of WPS, this helps in faster definitions of the domains (to take into account land boundaries) and can also be used to view preliminary results of WRF. IDV is considered for its ease of use and intuitive GUI for the user. NCL (NCAR Command Language) platform is programming language used to read netcdf files, the language is fast and effective method to read large netcdf files. Sample codes are available at [45], these codes are used for creating better visualizations and final stage plots from WRF output. Softwares such as VAPOR (Visualization and Analysis Platform for Ocean, Atmosphere, and Solar Researchers)[46] by UCAR for visualizing flow over time and to make animations is also explored, however due to its high video memory requirements and complex installation procedure, this software is unused. Panoply[47] by NASA for viewing output variables and to extract times-series data have also been utilized in this research during the preliminary stage of implementation.

Exploring the major features of WRF-ARW solver under WRF Software Framework (WSF)[48]. WSF include physics schemes proposed over the years to parameterize mesoscale flow, down-scaling with domains on a planetary level, pre-processing and post processing of data, observational nudging of the model, etc. Presented below are the major feature of WSF as defined by: [48]. Some of the major features for the reader's better understanding and relevance to the research are presented here. It is recommended to refer the cited for the complete list.

Major feature of WRF model:

- Equations: Fully compressible, Euler non-hydrostatic with a run-time hydrostatic option.
- Prognostic Variables: Velocity components u and v in Cartesian coordinate, vertical velocity w, perturbation potential temperature, perturbation geopotential, and perturbation surface pressure of dry air. Optionally, turbulent kinetic energy, Obhukov length, friction velocity, etc.
- Vertical Coordinate: Terrain-following, dry hydrostatic-pressure, with vertical grid stretching permitted. Top of the model is a constant pressure surface.
- Initial Conditions: Three dimensional for real-data.
- Nesting: One-way interactive, two-way interactive, and moving nests. Multiple levels and integer ratios.
- Among other, refer: [48]

Multiple physics options are presented in WRF model, the majority are divided into the following sub-categories.

- Microphysics: Physics schemes ranging from simplified physics suitable for mixed-phase physics, process studies such as cloud formation.
- Cumulus parameterizations: Physics scheme describing mass-flux schemes such as cloud movement.
- Surface physics: Physics scheme describing multi-layer land surface models ranging from a simple thermal model to full vegetation and soil moisture models, including snow cover and sea ice.
- Planetary boundary layer physics: Physics scheme describing turbulent kinetic energy prediction.

- Atmospheric radiation physics: Longwave and shortwave schemes with multiple spectral bands and a simple shortwave scheme suitable for climate and weather applications. Cloud effects and surface fluxes are included.

WRF is a very complex software capable of simulating majority of the atmospheric phenomena. Compiling procedure for WRF on hpc12 cluster at the aerospace faculty at TU Delft is followed per the procedure described in: [49]. The definitions used in the namelist options including; I/O options, physics schemes is a challenging feat on its own, with guidance from dr. Sukanta Basu, the namelists were defined. For a better understanding of the namelist files, please refer [50].

4.2.2. WRF implementation

The software is computationally very demanding. Delft University of Technology's high power computing cluster - 12 (Aerospace faculty) is used for this research. With a maximum usability of 48 cores. Implementation of WRF for the location of FINO - 1 is carried out in multiple stages. Described in the previous section are the softwares to effectively implement WRF for this research. Starting with defining the namelist.wps, dates for simulation are selected from data analysis. Domain configuration is chosen based on several trials of simulations for different domains and several resolutions. A one-way quadruple-nested domain as presented in the figure: 4.4 is chosen for this research considering computational costs. Presented in this section are the methodology used to define the stage of the namelist in WRF.

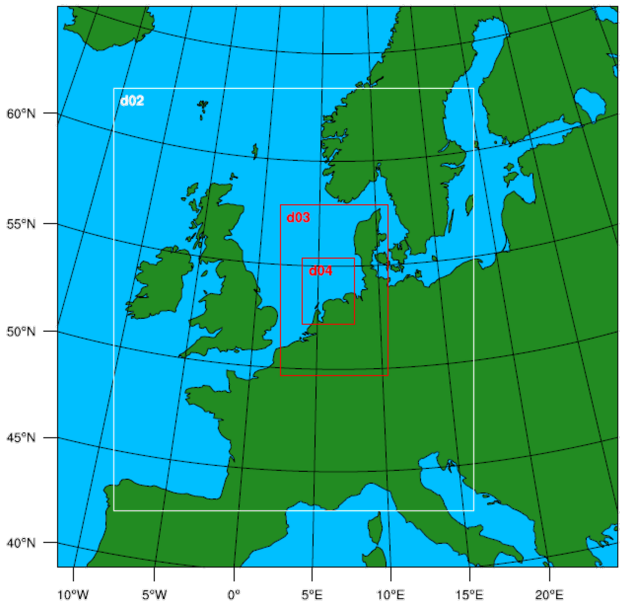

Figure 4.4: A representation of nested domains used for the assessment of low level jets over FINO1

Starting with the definition of the grid resolution of domains presented, ideally the resolution must be adequate for simulating loads on a wind turbine, an ideal grid resolution or a minimum grid resolution for simulating loads on a wind turbine has been studied in the past by Raj *et al.*[51]. The study presented a combination of different spatial resolutions (grid resolution) and temporal resolution and their effect on wind turbine loading. The study concluded stating a minimum grid resolution of 10m is adequate for a loss-less simulation of wind turbine loads. The turbine teste was a 1.5MW 3-bladed wind turbine. A different study by Sim *et al.*[52] produced the results; $\frac{1}{10}^{th}$ the diameter of the turbine in assessment and a minimum time step of 0.02 ($2 \cdot dx = 2 \cdot \frac{10m}{1000m}$) could provide loss-less results for loading analysis. Learning from these studies for this research, a time step of 0.02 and a spatial resolution of 12.6m (diameter of the turbine in consideration, NREL 5WM is 126m[53] therefore 126m/10) is need for simulating loads on a wind turbine accurately. Therefore in an ideal case, a WRF - LES simulation with aforementioned grid and temporal resolutions will serve the purpose of the research. However, after considering an added 5^{th} domain to the simulation the computational cost were found to be very high, refer table: 4.1. With the available 48 cores it would take an estimated 105 days for completing one such simulation. This being an unrealistic approach, a modelling framework as

proposed in figure:4.1 is necessary for simulating LLJ on a wind turbine with minimal computational costs. Therefore, a 4-way nested-domain over FINO - 1 is decided, with the largest domain having a spatial (grid) resolution of 27km and a temporal resolution of 180s (this is decided based on the thumb rule of WRF for times-step as $6 \cdot \delta x$, grid resolution in kilometers). The computational time for this grid is found to be close to 2 days, with 30 cores.

#		Grid resolution	Temporal resolution	Computation cost		
				Processors	RAM	Est.
1	Affordable case – 4 domains	1km	4s	48	30	~1 day
2	Near-Ideal Case – 5 domains	100m	0.2s	48	30	~105 days

Table 4.1: WRF computing time comparison for nested domains.

For WRF - setup, domains and date for simulation remain the same as WPS. I/O fields of WRF have been modified for the addition of Ohbukov length, surface roughness length using "myoutfields.txt" in the namelist.input (refer: B.3), a text file for the sub-function real to indicate addition or removal of variable from the output of the solver. Refer appendix B.2 for details of this definition. As mentioned earlier, time step has been defined based on the thumb rule for WRF simulation. Vertical grid levels, damping options and physics schemes have been defined in consultation with dr. Sukanta Basu specific to the location of FINO - 1. The resulting output of the WRF simulation provides 4-dimensional data set with 3-dimensions in space and 1-dimension in time for various simulated atmospheric variables. Data from the resulting netcdf files has been extracted using MATLAB (functions: ncread and netcdf). Of the extensive data-set output from WRF, variables that are relevant to the next step of the model framework are the wind profile for the time instant of the peak wind speed during low level jet, the obhukov length for calculating stability parameter, the surface roughness length and the vertical grid.

4.3. Synthetic turbulence model

To downscale the wind profile from WRF to a high resolution wind field, a site-specific spectral model is chosen for modelling the wind field for in this research. For the location of FINO - 1 Cheynet *et al.*'s spectral model as given in the equations: 2.25 and 2.26 with coherence function given by equations: 2.19 and 2.21 are utilized. Cheynet *et al.* presents the coefficient used in the equations 2.25, 2.26 and 2.19 based on the stability parameter derived from the site. The spectral equations are designed for stability parameter in the range of -2 and 2. The coefficients for the spectral equations are acquired from the author, are presented in Appendix B.5. Note: the coefficients are fitted to either of equation: 2.25 and 2.26 based on best possible match. The stability parameter depended Davenport coherence function is valid for stability parameter between the range of -2 and 0.3. Mentioned equations were implemented in the modelling software written by Etienne Cheynet[33], the software was written for Kaimal spectrum with davenport coherence model considering arbitrary decay coefficients. The software is modified to suit the requirements of this research by implementing the modified davenport model considering changes in stability parameter, IEC coherence model for stability parameter greater than 0.3 until 2, and the stability parameter dependent spectral equations. The site-specific spectral model is henceforth called CJR model (Etienne **C**heynet, Jasna B. **J**akobsen and Joachim **R**euder). The software is capable of producing a windfield inherently, in order to convert the same to FAST readable format, TurbSim ".bts" - binary format conversion using the code provided in Appendix B.3. Validation of the code used from mathworks [33] and TurbSim using the same IEC Kaimal spectrum (refer, equation: 2.16) is presented in the Appendix: B.4. The resulting file is provided as an input to FAST module.

4.4. NREL - FAST

"An aeroelastic computer-aided engineering (CAE) tool for horizontal axis wind turbines" National renewable energy laboratory's aeroelastic simulator - FAST is used to study the loads for the identified case studies, using a common wind turbine for the case studies, 5MW NREL - RE power wind turbine, provided by NREL-FAST as default Wind turbine. The specification of the turbine are presented in the table: 4.2.

Rating	5 MW
Rotor Orientation, Configuration Upwind,	3 Blades
Drivetrain High Speed,	Multiple-Stage Gearbox
Rotor, Hub Diameter	126 m, 3 m
Hub Height	90 m
Cut-In, Rated, Cut-Out Wind Speed	3 m/s, 11.4 m/s, 25 m/s
Cut-In, Rated Rotor Speed	6.9 rpm, 12.1 rpm
Rated Tip Speed	80 m/s
Overhang, Shaft Tilt, Precone	5 m, 5°, 2.5°
Rotor Mass	110,000 kg
Nacelle Mass	240,000 kg
Tower Mass	347,460 kg

Table 4.2: Specification of NREL-5MW wind turbine used for the study.

The turbine is a triple bladed offshore wind turbine rated at 5MW and a rated wind speed of 11.4m/s. For this research, we use the test 19 from FAST achieve - OC3-Monopile with rigid foundation for testing the wind loading[54]. The test is predefined in FAST, to incorporate an offshore wind turbine with mono-pile foundation. Note: FAST - Linux is used in this research, as it is coupled with the CJR and WRF models for ease of usage.

4.4.1. FAST model framework

FAST is a computer aided engineering tool combining aerodynamics models, hydrodynamics models for offshore structures, control and electrical system (servo) dynamics models, and structural (elastic) dynamics models for design and analysis of wind turbines. FAST enables analysis of a range of wind turbine configurations, including multi-bladed rotors, various foundations for the turbine, pitch or stall regulations, rigid rotor or teetering rotor and upwind or downwind rotor. The model frame work is presented in the figure: 4.5.

- External conditions - Parameters from the simulated windfield either from TurbSim or user-defined windfield consisting of 3 components of wind velocity, turbulence intensity, wind profile and mean wind speed at hub height. Parameters that induce loading on the turbine.
- Applied loads - Aerodynamic loads induced in the wind turbine due to external conditions and power extraction. Hydrodynamic loads influenced by waves and currents of the sea.

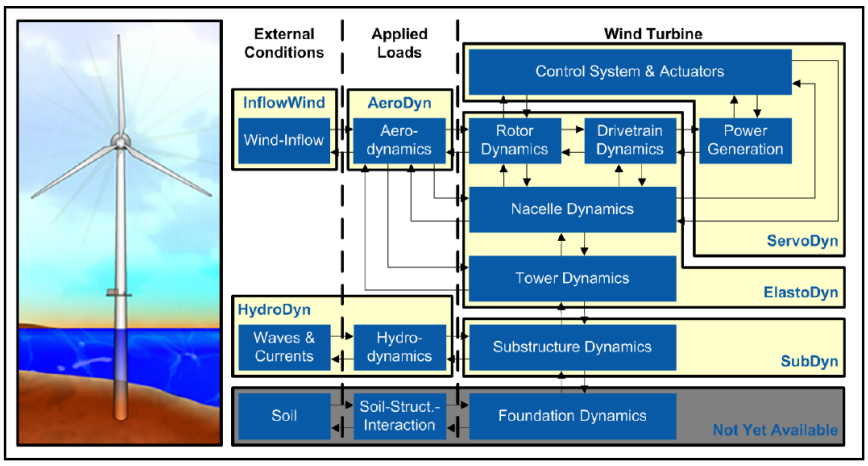

Figure 4.5: FAST - NREL model framework for bottom-fixed offshore wind turbine.

FAST model framework consists primarily of three stages:

- Wind turbine - This module corresponds to coupled physics: aero-hydro-servo-elasto modules. Aerodyn uses windfield parameters to solve for blade-element aerodynamic loads. Hydrodyn solves for

hydrostatic, diffraction and viscous loads on the turbine induced by the irregular incident waves and currents on an offshore wind turbine. Servodyn simulates controller logic for pitching, sensors aboard, yaw alignment, generator torque, etc. Elastodyn solves for structural loads on the rotor considering gravitational loads, servodyn, aerodyn and hydrodyn.

4.4.2. FAST Implementation

FAST-Linux interface on hpc is used for this research. Input wind field for FAST is created using the spectral model mentioned. The ultimate load cases are investigated in this thesis, primarily loads as presented in the table: 4.3 are investigated. Only one realization of loads cases is investigated, considering heavy computation time for the spectral model ($\approx$ 4 hours of simulation for one windfield on 15 processors and 10GB of RAM). The resulting loads are presented in the chapter: Case studies. A comparison between IEC standard spectral models and proposed model framework is studied here. In order to maintain equality of comparison between different spectral models "Meteorological and Non-IEC Meteorological Boundary Conditions" under the TurbSim input file are extracted from WRF to be implemented in TurbSim, these include; mean total wind speed, jet height, surface roughness length, latitude of the site, gradient Richardson number and friction velocity. For the proposed model approach, IEC coherence function is used for the the cases with high stability. For unstable conditions Davenport coherence model is used as the model described by Etienne Cheynet is limited to unstable conditions.

#	Forces /Moment	Notes
1	OoPBM	Out of plane bending moment of the Blade root
2	TTYM	Tower top yawing moment
3	FATBM	Tower fore-aft bending moment at base
4	GenPwr	Generator power

Table 4.3: A summary of the loads that will be studied.

5

Case studies and Discussion

This chapter presents results and discussion for the case studies identified (table: 3.2) through data-analysis. Model chain as presented in the flow chart: 4.1 is used for simulation. Simulations are performed using 30 cores and 10GB of RAM at high power computing facility at Aerospace faculty in Delft University of Technology. Comparison of wind profiles and wind shear from WRF and observational data is presented in the form of time vs height plots and wind shear plots. Presented in Appendix C.1 are the plots of WRF pressure contours, re-analysis archive data and hodographs for different case studies. FAST ultimate loads derived from WRF-CJR-FAST, IEC Kaimal-TurbSim-FAST and IEC GPLLJ-TurbSim-FAST are presented in the following sections. Ultimate design load case 1.1 (refer: 2.2) is explored in this thesis. Turbulence intensity class - C is chosen for analysis in this research, inferring from the research [55]. Ultimate loads for all case studies were calculated using the following methodology.

The safety factors and material properties considered for calculating ultimate loads are presented in the table: 5.1. Safety factors are assumed from IEC standards[15].

Table 5.1: Material properties and safety factors

Description	**Value**	**Units**
Tensile strength epoxy glass	900	MPa
Tensile strength steel	355	MPa
Blade clearance	10.97	m
Deflection safety factor	1.9305	
Stiffness flap-wise cylinder 1 (k)	1.81e+10	Nm^2
Stiffness flap-wise cylinder 2 (k)	7.13e+09	Nm^2
y - cylinder 1	1.69	m
y - cylinder 2	1.36	m
Stress safety factor	2.03	

Maximum blade clearance was calculated using simple geometry given by equation: 5.1.

$$Bladeclearance = offset \cdot cos(\theta_1) + r \cdot sin(\theta_2) - (\frac{d}{2}) \tag{5.1}$$

Where, $offset$ is the nacelle offset = 5.019m, r is the blade radius = 63m, θ_1 is the tilt of nacelle affecting the clearance = 5°, θ_2 is the combined tilt of nacelle and the blade tip = $(5+2.5)°$, d is the diameter of the tower section relevant for tip deflection = 4.5090m. Tip deflection and stress safety factors were calculated using the partial safety factors given by the IEC standard. Presented in the equation: 5.2.

$$\gamma_s = \gamma_f \times \gamma_m \times \gamma_n \tag{5.2}$$

Where, γ_f is the load safety factor = 1.3, γ_m is the material safety factor = 1.3 for stress and 1.1 for tip deflection and γ_n is the load severity/consequence of failure = 1.35. Maximum stress and the respective safety factors are calculated from FAST results, extracting maximum of root moments, tower base and top moments

and tip deflection. Although the maximum stress on the blade will occur at a weaker cross-section of the blade geometry than the root, for simplicity root stress is calculated. Basic stress formulae are considered for calculating the maximum stress on cylinder 1, 2 of the blade (blade root section 1 and root section 2), tower top and tower base. As presented in equations: 5.3 through 5.5.

$$\sigma_s = \frac{M \times y}{I} \tag{5.3}$$

$$I = \frac{k}{E} \tag{5.4}$$

$$Safety\ factor = \frac{Tensile\ strength}{\sigma_s \times \gamma} \tag{5.5}$$

Maximum blade tip deflection is calculated as the maximum deflection between in-plane and out of plane deflection. Maximum blade root stress was calculated as the maximum between blade root moment Edge wise, blade root moment Flap wise and blade root moment in-plane. Maximum stress at the top and bottom of the tower were calculated as the maximum of of tower fore-aft moment and tower top yawing moment. Using the aforementioned methodology of calculating ultimate loads, presented in the following section are the case studies identified for this research.

5.1. Case study 1 - 2 July 2006

The following section presents WRF vs observation results and FAST results for the case of 2^{nd} July 2006.

5.1.1. WRF results

Comparison of the time vs height plots of WRF and observations are presented in figure: 5.1. Note: vertical spatial resolution of WRF and observation is not the same. WRF captures the event, low level jet, as indicated by the observations (bright yellow) at a similar time period of the day. Further increase in WRF resolution may help capturing the event better, however for this research considering limited computational power presented results are carried forward for further analysis. Please note: WRF pressure contours their comparison with re-analysis archives and accessing hodographs for this event are presented in the Appendix: C.2.

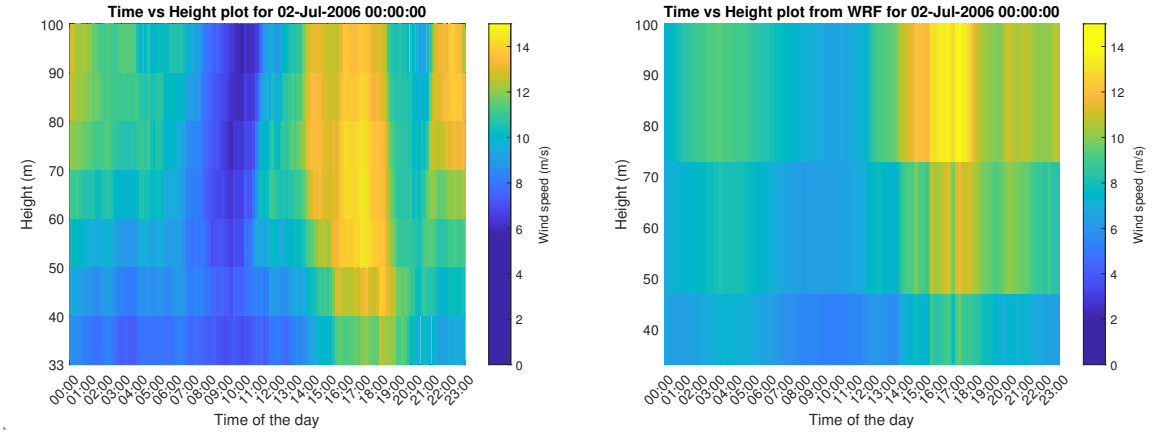

Figure 5.1: Comparison of observed and simulated wind fields for the case 2^{nd} July 2006, starting from the left, time vs height plot of observed data at FINO 1 and time vs height plot of WRF simulation.

Wind shear profile at one instant of time, 17:00 is extracted from WRF to be used in CJR model for creating a 10-minute windfield for FAST simulations considering a grid height for FAST of 160m. The wind shear is presented in the figure: 5.2. For this research one instant of time at 17:00 during the LLJ is identified for investigating ultimate loading on the wind turbine.

Wind shear profile comparison between WRF and observations at 17:00 until the observational height limit of 100m is presented in the figure: 5.2. Lower resolution of WRF is assumed to effect the wind shear profile at these heights, however as the model can still predict LLJ at the right instant of time, identified wind profile as presented in figure: 5.2 is used for further analysis.

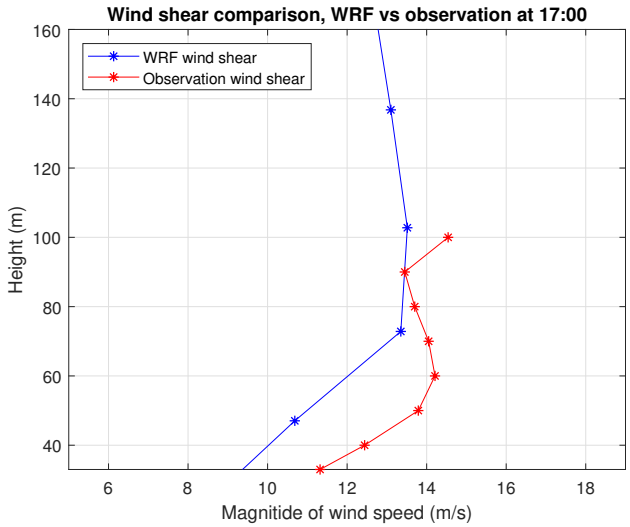

Figure 5.2: Wind shear comparison between WRF and observations for the day: 2^{nd} July 2006 at 17:00. Similar wind profile is simulated.

Spectral equations for CJR model are dependent on the stability parameter(ζ), therefore ζ is extracted from WRF at the instant of time, 17:00 at hub height of 90m (through linear interpolation between vertical levels), and is found to be 1.8. Recalling, IEC coherence model will be used for positive ζ values, IEC coherence model is thus used for this case-study.

5.1.2. FAST results

This section presents results from FAST comparing CJR model, IEC great plains LLJ (GP_LLJ) and Kaimal spectrum induced loading on the 5MW wind turbine as presented in table: 4.2. The comparison for out of plane bending moment, tower top yaw moment, tower base fore-aft moment, generator power and magnitude of wind speeds are presented in figures: 5.3 through 5.6.

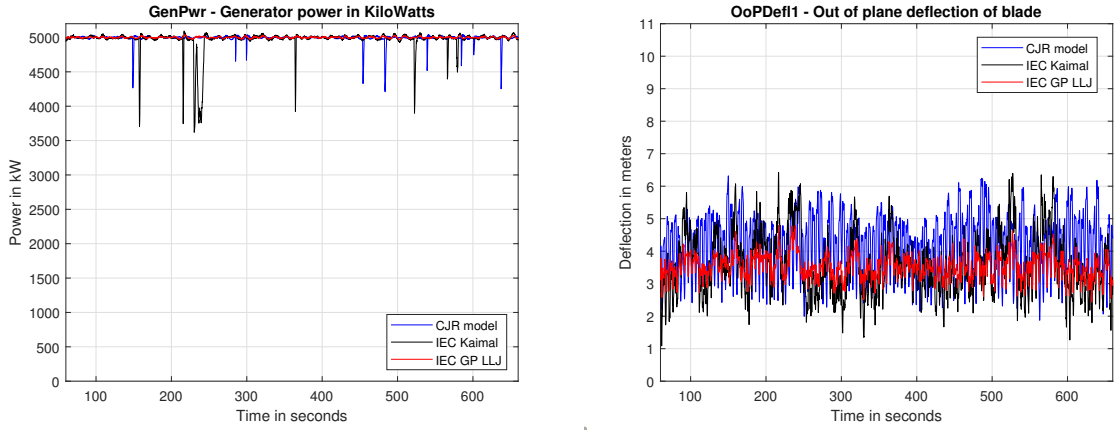

Figure 5.3: Comparison of out of plane bending moment and generator power for IEC Kaimal - NTM model, CJR model and IEC GPLLJ model.

Inference: As the hub height wind speed is greater than rated wind speed of the with turbine, we expect the power to be about 5MW. Fluctuations in the power are as a result of the FAST's variable-speed controller and pitch controller between the operating range of 2 and 3 as depicted in figure 7-2 of the definition of 5MW standard wind turbine [53].

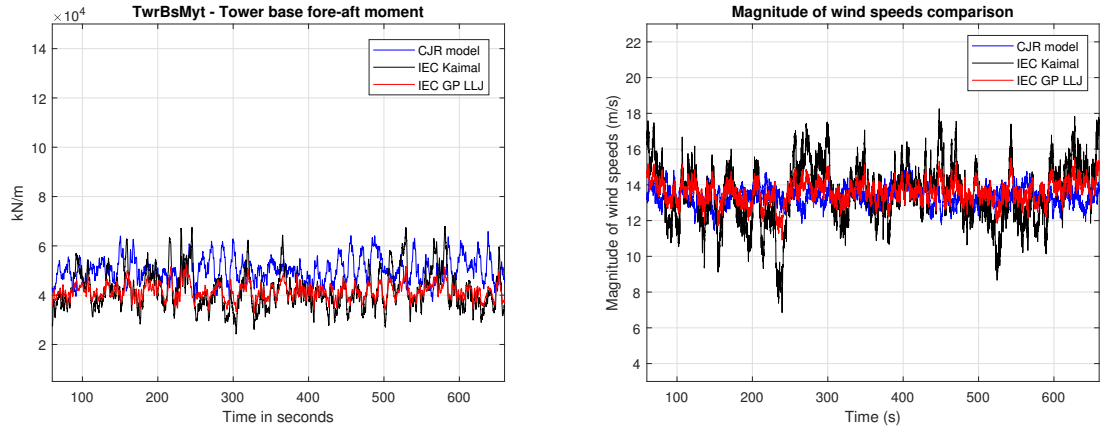

Figure 5.4: Comparison of tower base fore-aft moment and magnitude of wind speeds for IEC Kaimal - NTM model, CJR model and IEC GPLLJ model.

Inference: Implemented CJR model predicts lower turbulent wind profile in comparison to IEC Kaimal and IEC GPLLJ. To further examine the wind profiles from FAST, spectra for the components of wind speeds are plotted for comparison, presented in figure: 5.5 and figure: 5.6, u and w-component wind spectra for GP_LLJ model and CJR model are very similar. V-component demonstrates the presence of a spectral plateau for stable atmospheric boundary conditions, therefore energy content in CJR and GP_LLJ is similar but is vastly different from IEC Kaimal.

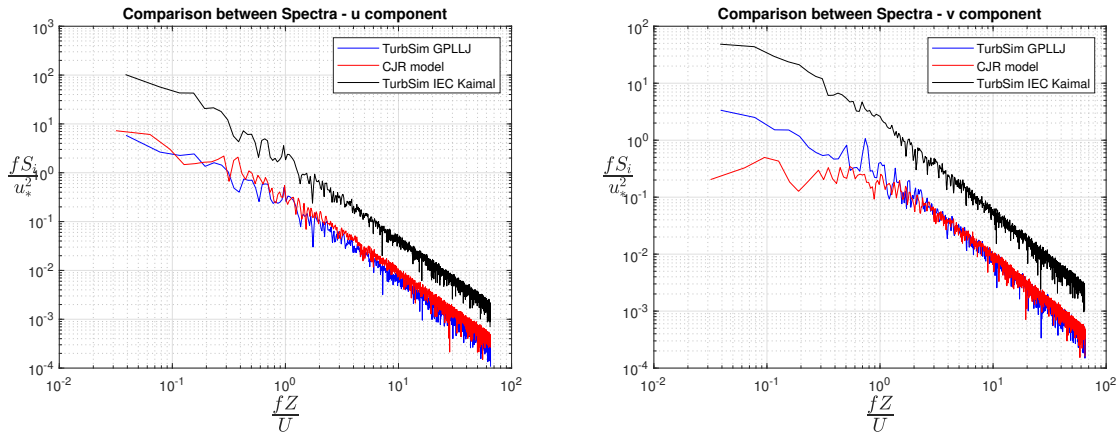

Figure 5.5: Comparison of u and v component of wind speeds for IEC Kaimal - NTM model, CJR model and IEC GPLLJ model.

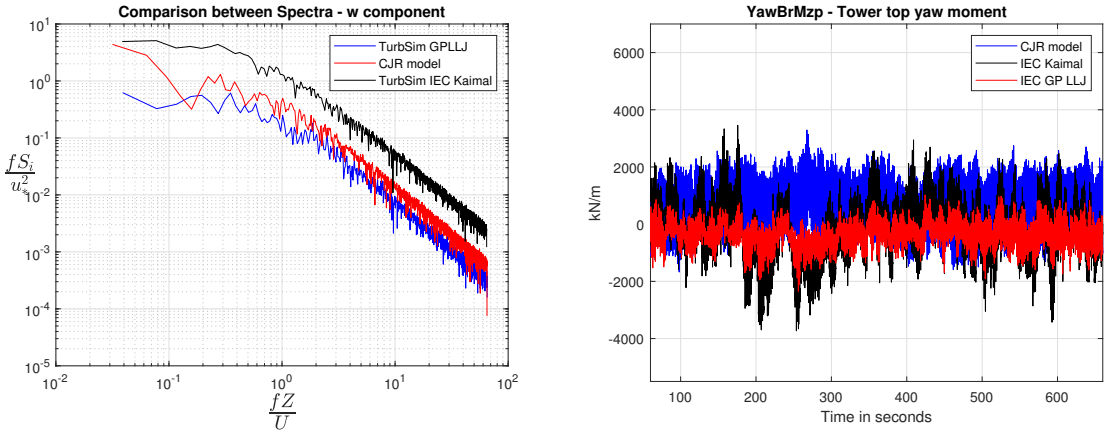

Figure 5.6: Starting from left, comparison of spectra for w-component of wind speeds. Right, comparison of tower top yaw moment for IEC Kaimal - NTM model, CJR model and IEC GPLLJ model.

Further study on the ultimate loads is Presented in table: 5.2 are the results of estimated ultimate loads on the wind turbine. CJR model overall predicts lower values of stress and tip deflection in comparison to IEC Kaimal, but predicts the same or more in IEC GPLLJ model. This difference in loads due to lower turbulence predicted by CJR model. Lower turbulence at hub height was also observed in the research by Westerhellweg *et al.* [55] for higher stabilities.

Description	CJR	Units	MoS	IEC Kaimal	Units	MoS	IEC GPLLJ	Units	MoS
'Max Blade tip deflection'	6.32	'm'	0.90	6.42	'm'	0.88	6.42	'm'	0.88
'Blade clearance'	4.65	'm'	0.90	4.54	'm'	0.88	4.54	'm'	0.88
'Stress at cylinder 1'	79.52	'MPa'	4.96	84.12	'MPa'	4.69	64.82	'MPa'	6.09
'Stress at cylinder 2'	162.39	'MPa'	2.43	171.77	'MPa'	2.30	132.36	'MPa'	2.98
'Stress at tower base'	167.26	'MPa'	1.05	172.69	'MPa'	1.02	133.06	'MPa'	1.32
'Stress at tower top'	14.83	'MPa'	11.82	16.80	'MPa'	10.44	10.56	'MPa'	16.60

Table 5.2: Ultimate loads comparison between CJR, IEC Kaimal and IEC GPLLJ models.

5.2. Case study 2 - 23 May 2012

Following similar construct as case study 1 presented in the following sections are the results from WRF, observations and FAST for the case: 23^{rd} May 2012.

5.2.1. WRF results

Comparison of the time vs height plots of WRF and observations are presented in figure: 5.7. Note: vertical spatial resolution of WRF and observation is not the same. WRF captures the event at a higher vertical level in comparison to the observations. Low level jet, as indicated in the observations (bright yellow). Further increase in WRF resolution may help in capturing the event better, however for this research with limited computational power presented results are carried forward. Please note: WRF pressure contours their comparison with re-analysis archives and hodographs for this event are presented in the Appendix: C.3.

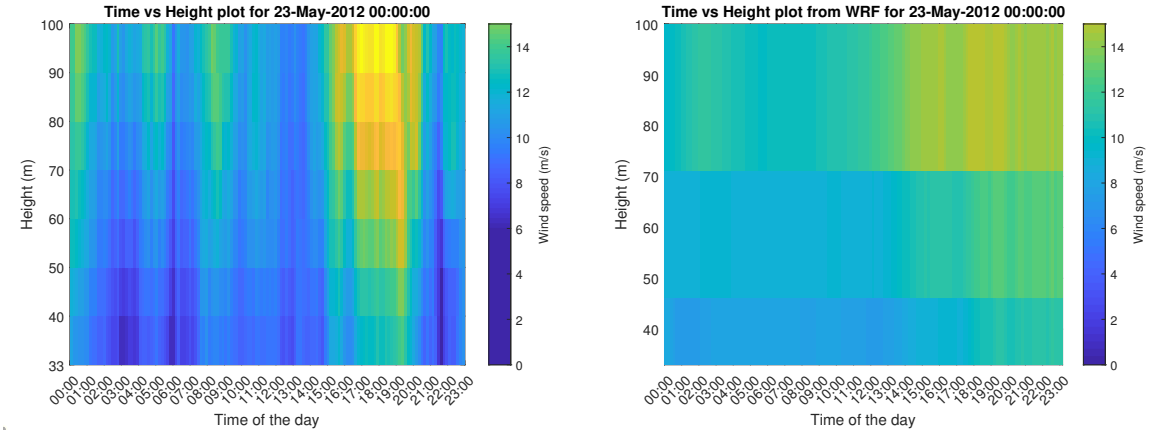

Figure 5.7: Comparison of observed and simulated wind fields for the case 23^{rd} May 2012, starting from the left, time vs height plot of observed data at FINO 1 and time vs height plot of WRF simulation.

Wind shear profile at one instant of time, 18:00 is extracted from WRF to be used in CJR model for creating a 10-minute windfield considering a grid height for FAST of 160m. The wind shear is presented in the figure: 5.8. For this research one instant of time at 18:00 during the LLJ is identified for investigating ultimate loading on the wind turbine.

Wind shear profile comparison between WRF and observations at 18:00 until the observational height limit of 100m is presented in the figure: 5.8. Lower resolution of WRF is assumed to effect the wind shear profile at these heights, however as the model can still predict LLJ at the right instant of time, identified wind profile as presented in figure: 5.8 is used for further analysis.

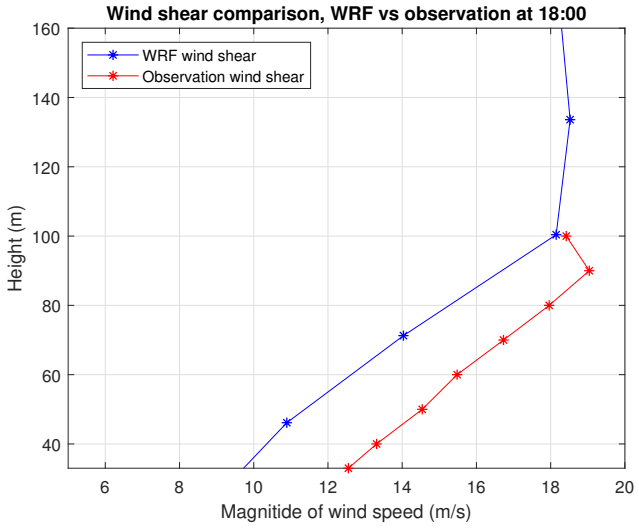

Figure 5.8: Wind shear comparison between WRF and observations for the day: 23^{rd} May 2006 at 18:00. Similar wind profile is simulated.

Spectral equations for CJR model are dependent on the stability parameter(ζ), therefore ζ is extracted from WRF at the instant of time, 18:00 at hub height of 90m (through linear interpolation between vertical levels), and is found to be 1.8.

5.2.2. FAST results

This section presents results from FAST comparing CJR, IEC great plains LLJ (GP_LLJ) and Kaimal spectrum induced loading on the 5MW wind turbine as presented in table: 4.2. The comparison for out of plane bending moment, tower top yaw moment, tower base fore-aft moment, generator power and magnitude of wind speeds are presented in figures: 5.9 through 5.12.

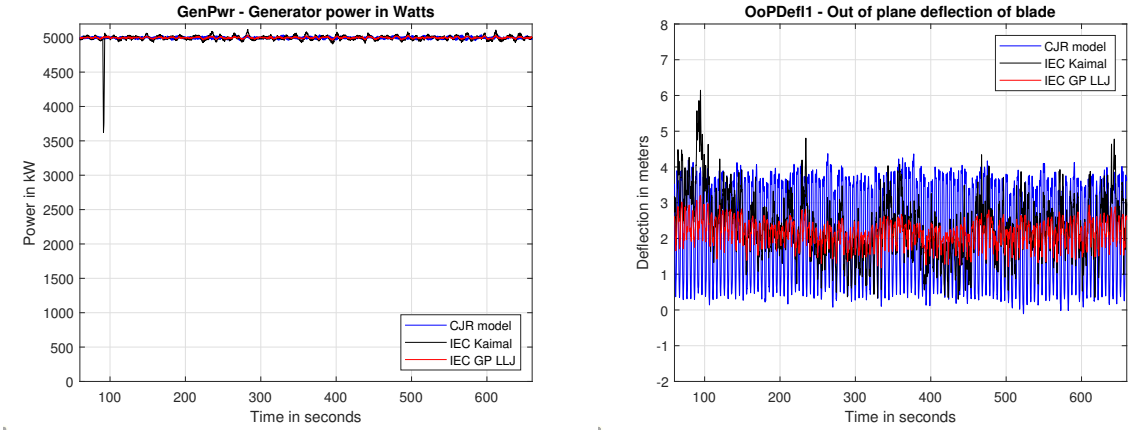

Figure 5.9: Comparison of out of plane bending moment and generator power for IEC Kaimal - NTM model, CJR model and IEC GPLLJ model.

Inference: As the hub height wind speed is greater than rated wind speed of the with turbine, we expect the power to be about 5MW. Fluctuations in out of plane bending moment are induced due to turbulence in the wind field and FAST's in-built pitch controller. The oscillations in out of plane blade deflection are as a result of both excitation frequencies and natural frequencies induced by the higher wind shear of CJR model in comparison to IEC models.

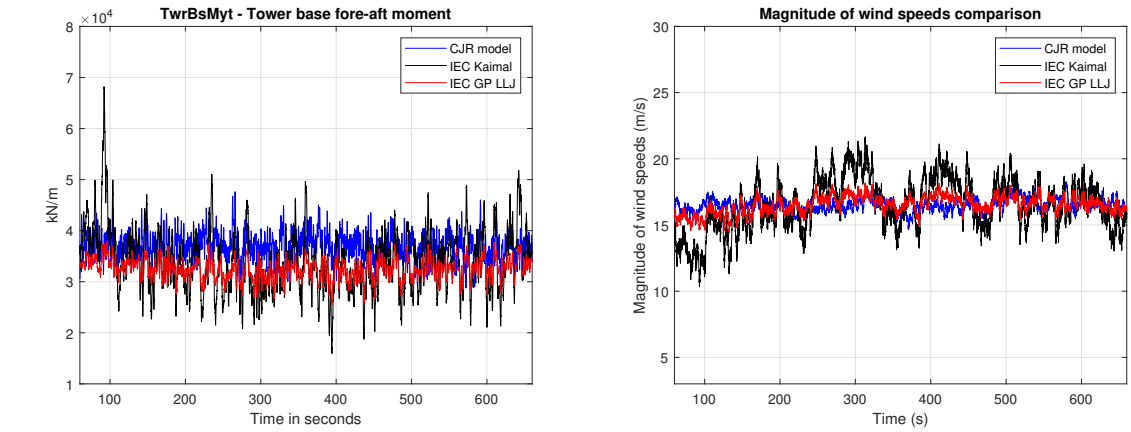

Figure 5.10: Comparison of tower base fore-aft moment and magnitude of wind speeds for IEC Kaimal - NTM model, CJR model and IEC GPLLJ model.

Inference: Implemented CJR model predicts lesser turbulence in comparison to IEC Kaimal and IEC GPLLJ. A spectral analysis for this case is performed to infer energy content in the input wind field at high stability. Figure: 5.11 and 5.12 present the spectra comparison for the input wind field, as presented in the study by Etienne Cheynet a spectral plateau is present for v and w components of the wind field.

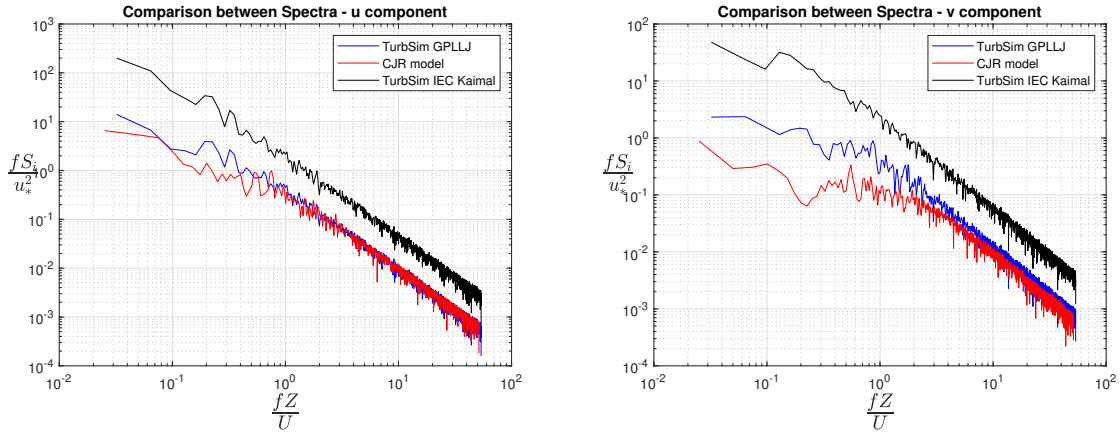

Figure 5.11: Comparison of wind spectra for components of wind field as input to FAST for spectral models, IEC Kaimal, GP_LLJ and CJR model.

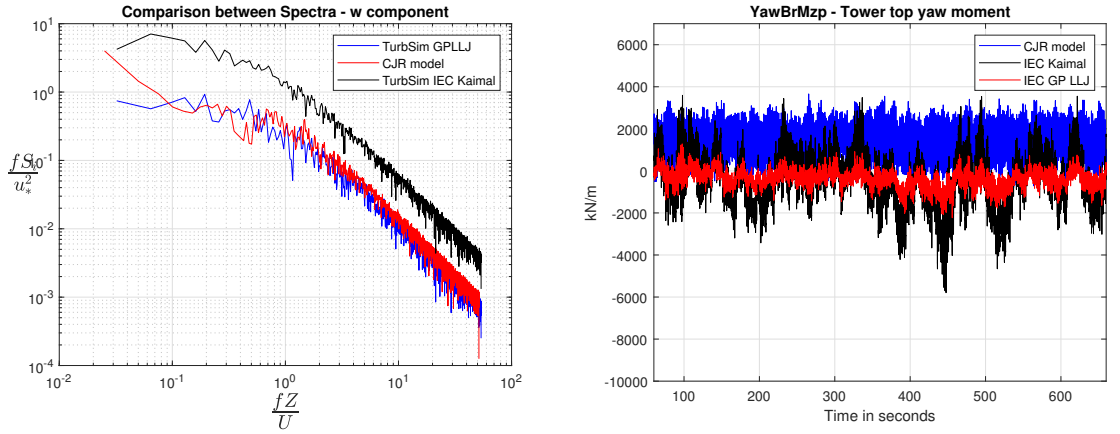

Figure 5.12: Starting from left, w-component wind spectra for IEC Kaimal, CJR and GP_LLJ model as input wind fields to FAST. Right, comparison of tower top yaw moment for IEC Kaimal - NTM model, CJR model and IEC GPLLJ model.

Presented in table: 5.3 are the results of estimating ultimate loads on the wind turbine. CJR model presents lower values of tip deflection in comparison to IEC Kaimal but greater values to IEC GPLLJ model. CJR model estimates slightly higher stress values at cylinder 1, 2 and tower top.

Description	CJR	Units	MoS	IEC Kaimal	Units	MoS	IEC GPLLJ	Units	MoS
'Max Blade tip deflection'	4.37	'm'	1.30	6.15	'm'	0.92	6.15	'm'	0.92
'Blade clearance'	6.59	'm'	1.30	4.82	'm'	0.92	4.82	'm'	0.92
'Stress at cylinder 1'	61.14	'MPa'	6.45	75.71	'MPa'	5.21	46.36	'MPa'	8.51
'Stress at cylinder 2'	124.84	'MPa'	3.16	154.60	'MPa'	2.55	94.68	'MPa'	4.17
'Stress at tower base'	121.08	'MPa'	1.45	173.37	'MPa'	1.01	96.66	'MPa'	1.81
'Stress at tower top'	16.47	'MPa'	10.65	26.08	'MPa'	6.72	10.03	'MPa'	17.47

Table 5.3: Ultimate loads comparison between CJR, IEC Kaimal and IEC GPLLJ models.

5.3. Case study 3 - 14 April 2004

Following similar report construct as case study 1 presented in the following sections are the results from WRF, observations and FAST for the case: 14^{th} April 2004.

5.3.1. WRF results

Comparison of the time vs height plots of WRF and observations are presented in figure: 5.13. Note: vertical spatial resolution of WRF and observation is not the same. WRF captures the event, as indicated in the observations (bright yellow). Further increase in WRF resolution may help in capturing the event better, however for this research with limited computational power presented results are carried forward. Please note: WRF pressure contours their comparison with re-analysis archives and hodographs for this event are presented in the Appendix: C.4.

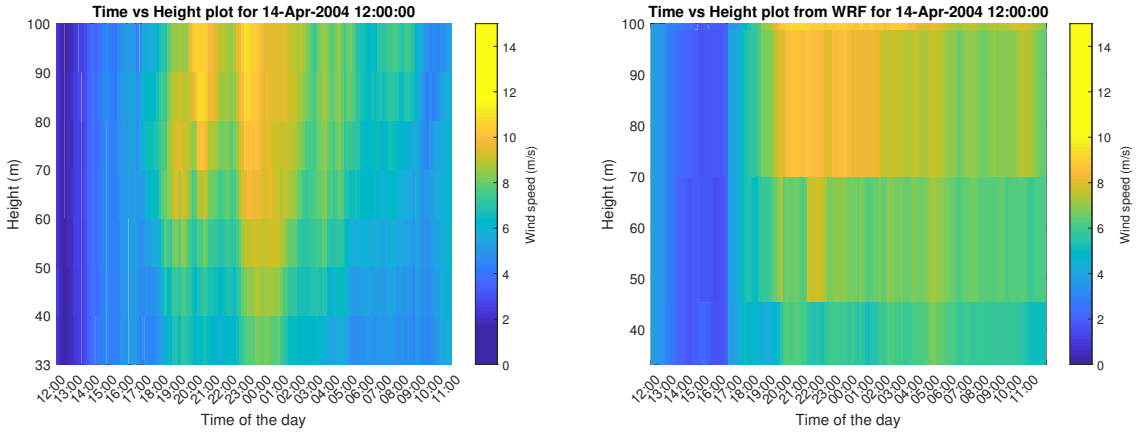

Figure 5.13: Comparison of observed and simulated wind fields for the case 14^{th} April 2004, starting from the left, time vs height plot of observed data at FINO 1 and time vs height plot of WRF simulation.

Wind shear profile at one instant of time, 20:20 is extracted from WRF to be used in CJR model for creating a 10-minute windfield considering a grid height for FAST of 160m. The wind shear is presented in the figure: 5.14. For this research one instant of time at 20:20 during the LLJ is identified for investigating ultimate loading on the wind turbine.

Wind shear profile comparison between WRF and observations at 20:20 until the observational height limit of 100m is presented in the figure: 5.14. Lower resolution of WRF is assumed to effect the wind shear profile at these heights, however as the model can still predict the event at the right instant of time, identified wind profile as presented in figure: 5.14 is used for further analysis.

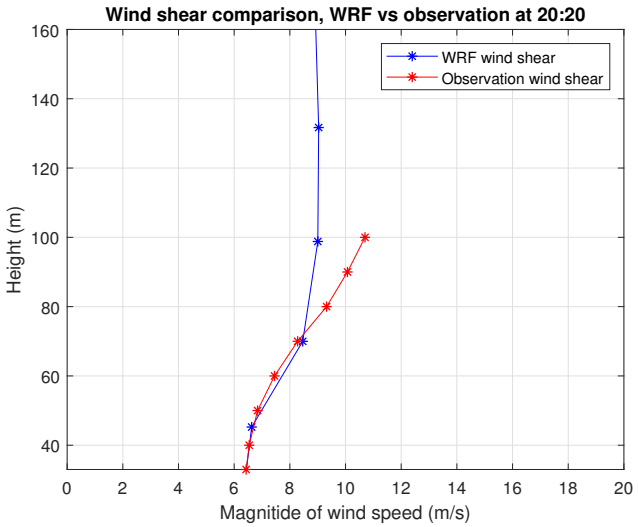

Figure 5.14: Wind shear comparison between WRF and observations for the day: 14^{th} April 2004 at 20:20. Similar wind profile is simulated.

Spectral equations for CJR model are dependent on the stability parameter(ζ), therefore ζ is extracted from WRF at the instant of time, 20:20 at hub height of 90m (through linear interpolation between vertical levels), and is found to be -1.94. Therefore stability parameter dependent Davenport coherence model is used for this case study, refer equation: 2.19. As the event visually represents a low level jet, it is deemed as one in this thesis. However LLJ in unstable atmospheric boundary conditions is not a commonality and would need to be studied further.

5.3.2. FAST results

This section presents results from FAST comparing CJR, IEC great plains LLJ (GP_LLJ) and Kaimal spectrum induced loading on the 5MW wind turbine as presented in table: 4.2. The comparison for out of plane bending moment, tower top yaw moment, tower base fore-aft moment, generator power and magnitude of wind speeds are presented in figures: 5.15 through 5.18.

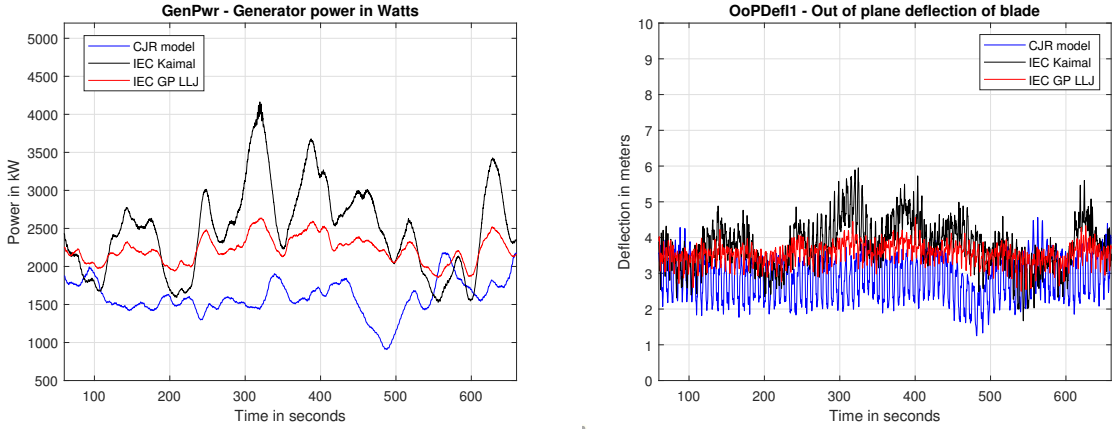

Figure 5.15: Comparison of out of plane bending moment and generator power for IEC Kaimal - NTM model, CJR model and IEC GPLLJ model.

Inference: The lower turbulence in the CJR model presents lower power production in comparison IEC Kaimal and GPLLJ. Similar effect is observed in the case of out of plane tip deflection.

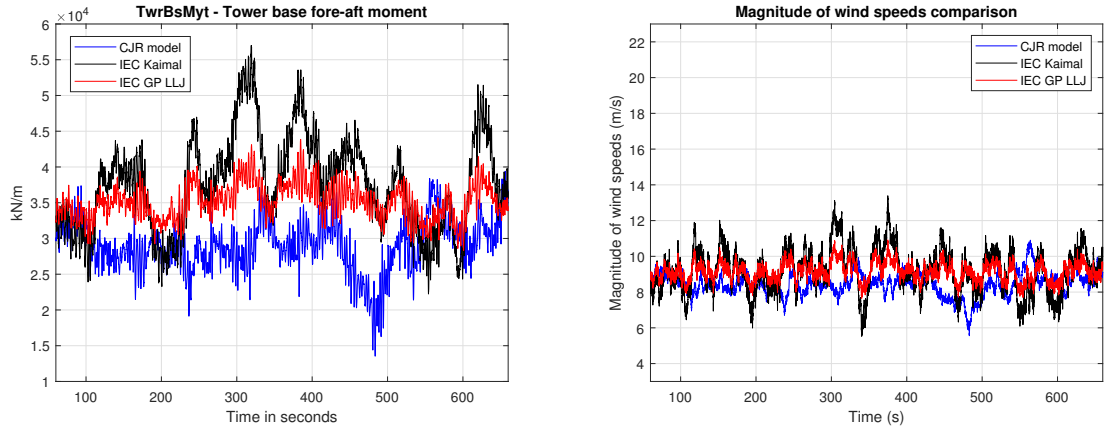

Figure 5.16: Comparison of tower base fore-aft moment and magnitude of wind speeds for IEC Kaimal - NTM model, CJR model and IEC GPLLJ model.

Inference: CJR model's lower energy content presents lower magnitude of forces in comparison to IEC Kaimal and GP_LLJ models. A comparison of the spectra for the three models is presented in the figure: 5.17 and 5.18

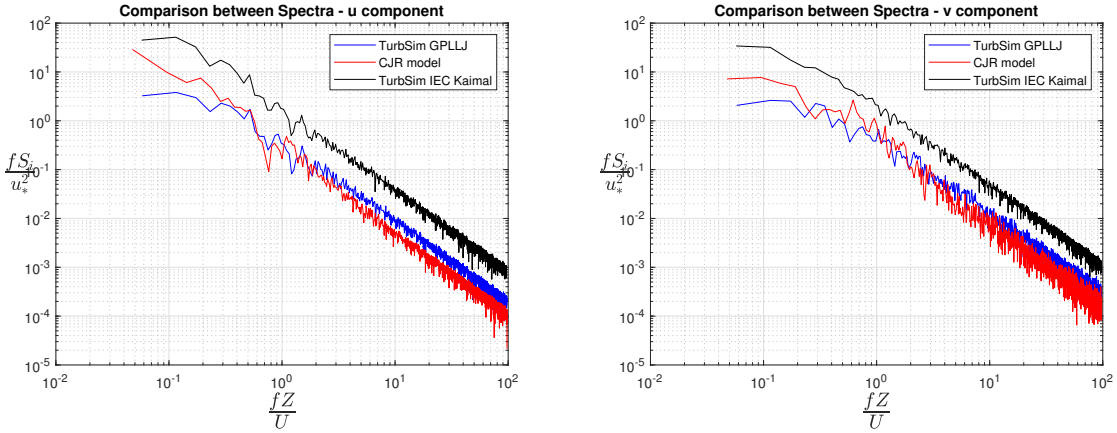

Figure 5.17: Comparison of wind spectra for IEC Kaimal, GP_LLJ and CJR model as input to FAST simulations.

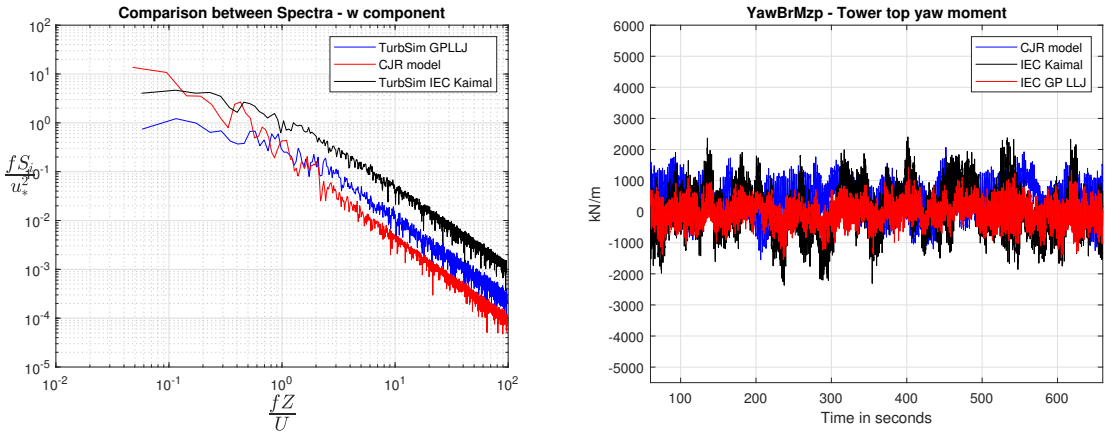

Figure 5.18: Starting from right, comparison of wind spectra for w-component of CJR, IEC Kaimal and GP_LLJ model. Right, comparison of tower top yaw moment for IEC Kaimal - NTM model, CJR model and IEC GPLLJ model.

Presented in table: 5.4 are the results of estimating ultimate loads on the wind turbine. CJR model presents

lower values of tip deflection and stresses in comparison to IEC Kaimal and IEC GPLLJ model at cylinder 1, 2 and tower base. At unstable conditions ultimate loading predicted via CJR model is lower in comparison to other models used.

Description	CJR	Units	MoS	IEC Kaimal	Units	MoS	IEC GPLLJ	Units	MoS
'Max Blade tip deflection'	4.56	'm'	1.25	5.95	'm'	0.95	5.95	'm'	0.95
'Blade clearance'	6.41	'm'	1.25	5.02	'm'	0.95	5.02	'm'	0.95
'Stress at cylinder 1'	55.33	'MPa'	7.13	72.14	'MPa'	5.47	55.73	'MPa'	7.08
'Stress at cylinder 2'	112.99	'MPa'	3.49	147.30	'MPa'	2.68	113.81	'MPa'	3.47
'Stress at tower base'	100.21	'MPa'	1.75	144.90	'MPa'	1.21	111.52	'MPa'	1.57
'Stress at tower top'	9.31	'MPa'	18.82	10.82	'MPa'	16.20	6.93	'MPa'	25.31

Table 5.4: Ultimate loads comparison between CJR, IEC Kaimal and IEC GPLLJ models.

5.4. Discussion

Presented here in plots 5.19 through 5.21 are consolidated comparisons for the stressed calculated for the case studies.

Presented in figure: 5.19 are the consolidated results for maximum stress calculated at the blade root, cylinder 1 and cylinder 2. Blade root stress at both cylinder 1 and cylinder 2 are directly related to the tip deflection, for the case of CJR model lower maximum tip deflection is inferred from the figure: 5.20 in comparison to IEC Kaimal and IEC GPLLJ. Cylinder 1 and cylinder 2 of the blade root represent a higher stress value for IEC Kaimal in comparison to CJR and IEC GPLLJ model, this is pertaining to the fact that IEC Kaimal establishes a higher variance in wind spectra that is higher turbulence. It must be noted that, for the case of 14^{th} April 2004 no significant difference is observed at cylinder 1 and 2, whereas in cases of higher stabilities such as 2^{nd} July 2006 and 23^{rd} May 2012 CJR model predicts higher stresses on the blade root in comparison to GPLLJ model. It must be pointed out that CJR and GPLLJ models are site-specific spectral models for different locations, Kansas being closer to the equator and FINO1 higher up in the hemisphere. Further investigation using SCADA data or FEM analysis could provide better insights into each model's viability at said location.

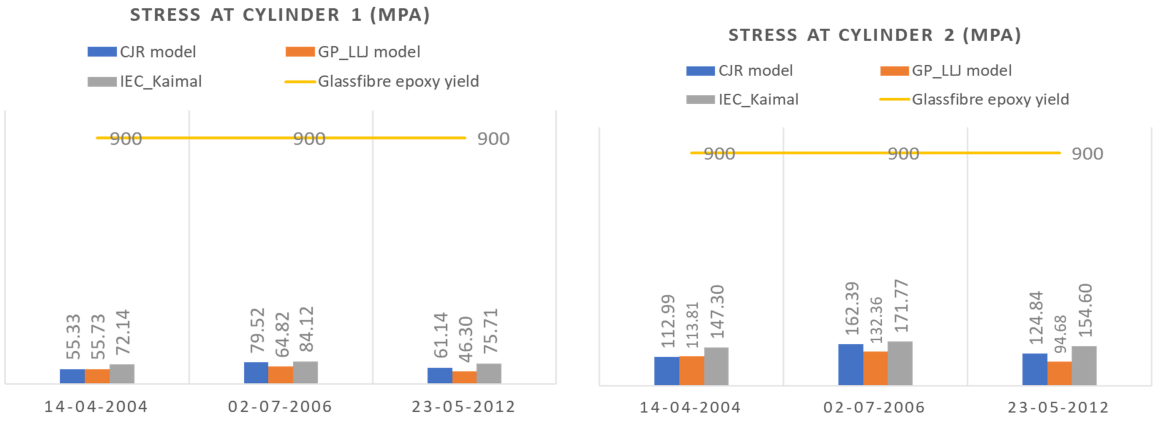

Figure 5.19: Comparison of stress at cylinder 2 for presented case studies for IEC Kaimal - NTM model, CJR model and IEC GPLLJ model.

Drawing observations from Jinkyoo *et al.* [10], higher wind shear added to a neutral boundary layer indicates enhanced periodic spikes in out of plane bending moment, as can be observed in the plots for out of

plane bending moment in section of case studies. Maximum tip deflection observed with the CJR model is lower than IEC Kaimal spectrum and IEC GPLLJ in all cases identified. Although the maximum tip deflection is lower than IEC models, visually larger variations in the deflection are observed in CJR model, therefore we recommend a fatigue analysis for the identified cases in comparison to IEC and SCADA data.

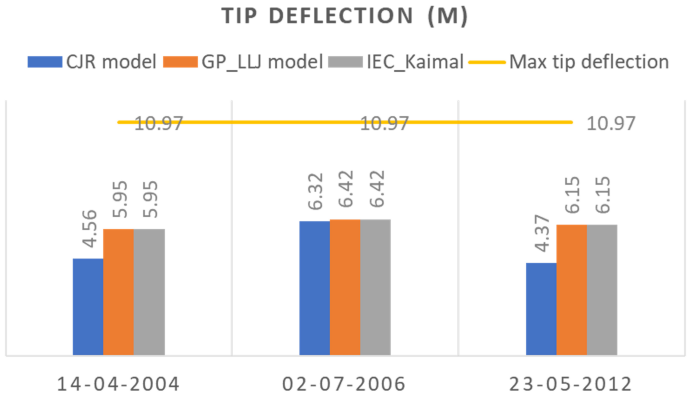

Figure 5.20: Comparison of tip deflection for presented case studies for IEC Kaimal - NTM model, CJR model and IEC GPLLJ model.

Drawing observations from Jinkyoo *et al.* [10] under a stable boundary layer (as in the case of 2^{nd} July 2006 and 23^{rd} May 2012) tower fore aft bending moment contains lower energy, therefore tower top and base loading should be lower in comparison to loading under a neutral boundary layer. Consequently lower loading on the tower top and base in comparison to IEC Kaimal is observed for the cases of IEC GPLLJ and CJR model, as presented in the figure: 5.21.

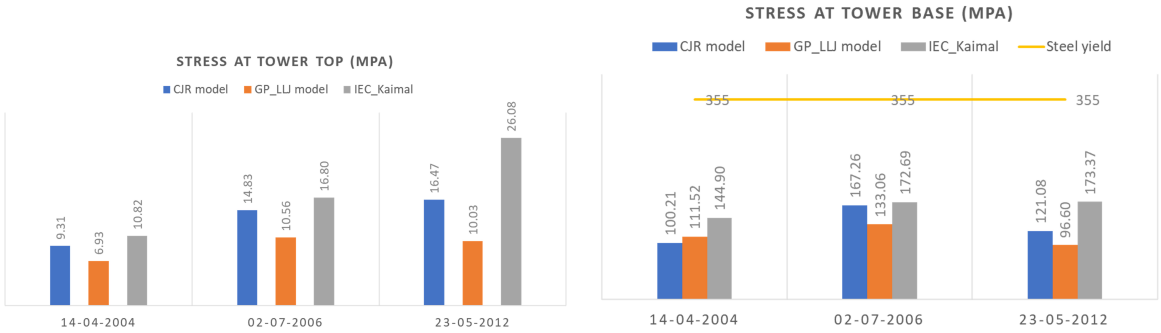

Figure 5.21: Comparison of stress at tower top and base for presented case studies for IEC Kaimal - NTM model, CJR model and IEC GPLLJ model.

Consolidating the results of all cases studies in the table: 5.5. For cases of high stability, on an average proposed model predicts 21% higher stress on blade root (cylinder 1 and 2) and 27% higher at the tower top and base in comparison to IEC GPLLJ and 15% and 30% lower in comparison to IEC Kaimal, respectively. Similarly, under unstable conditions, proposed model predicts similar loads on the blade root, 7% lower loads at the tower top and base in comparison to IEC GPLLJ and 30% higher loads for blade root and tower top and base in comparison to IEC Kaimal.

	Description	**Results CJR**	**Results GPLLJ**	**% increase GPLLJ-CJR**	**Results IEC**	**% increase IEC Kaimal-CJR**
14-04-2004	Max Blade tip deflection (m)	4.56	5.95	30.48	5.95	30.48
	Stress at cylinder 1 (MPa)	55.33	55.73	0.72	72.14	30.38
	Stress at cylinder 2 (MPa)	112.99	113.81	0.73	147.30	30.37

	Stress at tower base (MPa)	100.21	111.52	11.29	144.90	44.60
	Stress at tower top (MPa)	9.31	6.93	-25.56	10.82	16.22
02-07-2006	Max Blade tip deflection (m)	6.32	6.42	1.58	6.42	1.58
	Stress at cylinder 1 (MPa)	79.52	64.82	-18.49	84.12	5.78
	Stress at cylinder 2 (MPa)	162.39	132.36	-18.49	171.77	5.78
	Stress at tower base (MPa)	167.26	133.06	-20.45	172.69	3.25
	Stress at tower top (MPa)	14.83	10.56	-28.79	16.80	13.28
23-05-2012	Max Blade tip deflection (m)	4.37	6.15	40.73	6.15	40.73
	Stress at cylinder 1 (MPa)	61.14	46.30	-24.27	75.71	23.83
	Stress at cylinder 2 (MPa)	124.84	94.68	-24.16	154.60	23.84
	Stress at tower base (MPa)	121.08	96.60	-20.22	173.37	43.19
	Stress at tower top (MPa)	16.47	10.03	-39.10	26.08	58.35

Table 5.5: Consolidated results of stresses and tip deflection for cases studies identified.

The results presented here are considering a single realization of the wind fields, increase in realizations could point to a better conclusion for ultimate loading. Cheynet *et al.* proposes spectral model at 3 different heights further improvements in the proposed model framework could include 3 spectral equations instead of one spectral equation derived at a specific height. In this research however, to maintain simplicity for direct comparison between spectral models, only spectral equation for the hub height is taken. Combining all spectral equations into the synthetic turbulence model could deem an interesting method of approach to understand wind turbine loading.

Concluding, this project developed a model framework to analyse low-level jets on a wind turbine specific to a site with low computational costs. While the capabilities of the model have been successfully showcased, only a partial validation on a benchmark case has been carried out, refer: B.4. Therefore, going forward a full physical validation of the model for its accuracy for its target applications is recommended.

A

Appendix

A.1. Data analysis - wind ramp, trend plots

Presented in figures: A.1, A.2 and A.3 depict the wind ramp occurring through the day.

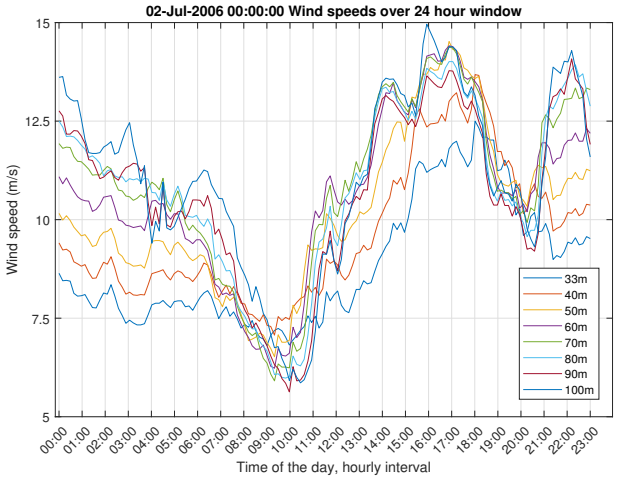

Figure A.1: Wind ramp for the day of 2^{nd} July 2006.

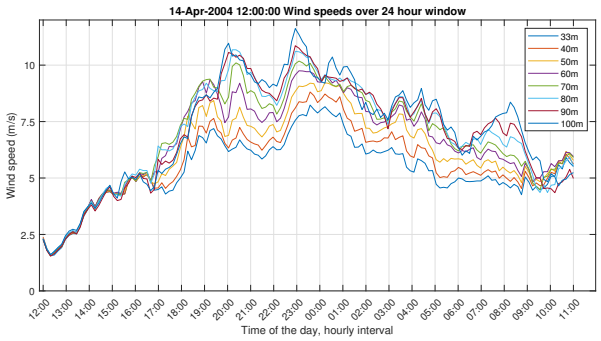

Figure A.2: Wind ramp for the day of 14^{th} April 2004.

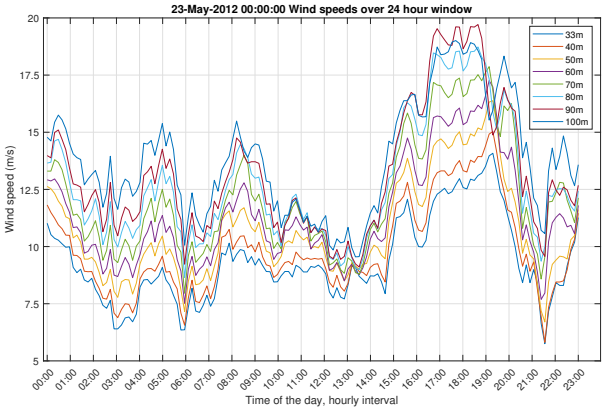

Figure A.3: Wind ramp for the day of 23^{rd} May 2012.

Histogram plotting occurrences of 95^{th} percentile threshold of shear exponent for the operating range of the wind turbine between 5m/s to 30m/s is presented in the figure: A.4. Months; March, April and May indicate the highest occurrence of wind shear exponent.

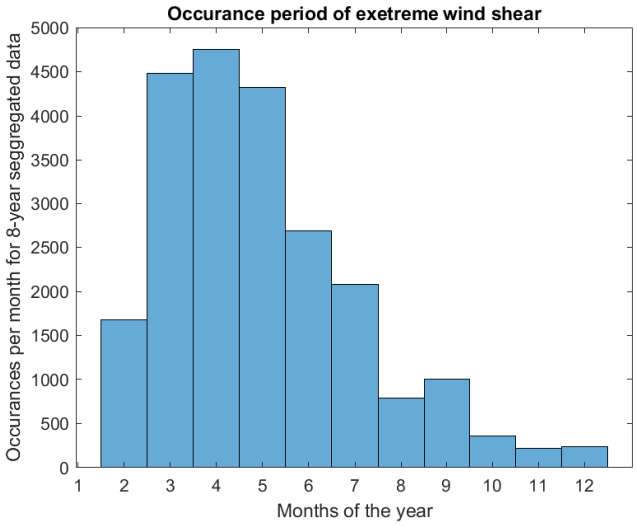

Figure A.4: Histogram plotting occurrences of 95^{th} percentile threshold of shear exponent for the wind range of 5m/s to 30m/s.

B

Appendix

B.1. WPS-setup

Presented in the tables: B.1 and B.2 are the inputs used for WRF pre-processing system, WPS.

&share	
wrf_core	'ARW',
max_dom	4,
start_date	'2012-05-23_00:00:00','2012-05-23_00:00:00','2012-05-23_00:00:00', '2012-05-23_00:00:00','2012-05-23_00:00:00',
end_date	'2012-05-24_00:00:00','2012-05-24_00:00:00','2012-05-24_00:00:00', '2012-05-24_00:00:00','2012-05-24_00:00:00',
interval_seconds	21600
io_form_geogrid	2,
/	
&geogrid	
parent_id	1, 1, 2, 3, 4,
parent_grid_ratio	1, 3, 3, 3, 2,
i_parent_start	1, 12, 98, 40, 67,
j_parent_start	1, 12, 80, 90, 95,
e_we	110, 211, 190, 274, 301,
e_sn	110, 247, 298, 346, 301,
geog_data_res	'10m','2m','30s','30s','30s',
dx	27000,
dy	27000,
map_proj	'lambert',
ref_lat	54.011,
ref_lon	6.607,
truelat1	30.0,
truelat2	60.0,
stand_lon	6.607,
geog_data_path	'/home/avemuri/Build_WRF_3.9.1.1/DATA/WPS_GEOG'
/	

Table B.1: Namelist.wps for one of the case study: 23rd May 2012, similar namelist is used for other case studies, with change in start-date and end-date.

The namelist.wps is divided into 4 stage (annotated with &...), which will be described here. &share - includes common denominators for WPS model such as maximum number of domains (max_dom) = 4, start and end date of the simulation - case study dependent, WRF solver - ARW, interval_seconds and

io_form_geogrid have not been changed. Geogrid - defining the domain's parent ID,and grid ratio (scaled based on dx and dy), coordinates and dimensions (i_parent, j_parent, e_we, e_sn), geographical map for projection, location of FINO - 1, truelat 1, truelat 2 and stand_lon confirm to Lambert projection. Terrestrial data used is also defined in this section of the namelist. &ungrib and &metgrid sections of this file provide options for the name of the output file.

&ungrib	
out_format	'WPS',
prefix	'FILE',
/	
&metgrid	
fg_name	'FILE'
io_form_metgrid	2,
/	

Table B.2: Namelist.wps for one of the case study: 23rd May 2012, similar namelist is used for other case studies, with change in start-date and end-date.

B.2. WRF-setup

Presented in tables: B.3 through B.8 are the inputs provided for namelist.input used for the setup of WRF. WRF namelist is divided into eight sections; &time_control - defining the running period of the model, restart capabilities of the model and modifications in output parameters, &domains - domain coordinates and dimensions are required to be the same as WPS domain's, pressure level or the vertical grid spacing is defined under eta_levels - these values have not been changed, &physics - physics scheme that will be considered for this model run are presented here, usage of physics packages instead of defining individual physics schemes sucha as one defined here is also an option in WRF version 4, &fdda - presents options for observational nudging - unused, &dynamics - further definitions on physics parameters, &bdy_control, &grib2 and &namelist_quilt are unchanged.

I/O variables have been modified in this model to extract certain relevant parameters from WRF model to be used as input to spectral model, using namelist.input option: myoutfields.txt. Defining in the simple format to add output variables as *+:h:0:ALT,RMOL,ZNT*. Here + is the addition of output variables to WRF model, ALT is the inverse air density, RMOL is the Obhukov length, and ZNT is the surface roughness length.

It must be noted that the namelists for WRF and WPS provided here are used for all case studies.

&time_control	
run_days	1,
run_hours	0,
run_minutes	0,
run_seconds	0,
start_year	2012, 2012, 2012, 2012, 2012,
start_month	05, 05, 05, 05, 05,
start_day	23, 23, 23, 23, 23,
start_hour	00, 00, 00, 00, 00,
start_minute	00, 00, 00, 00, 00,
start_second	00, 00, 00, 00, 00,
end_year	2012, 2012, 2012, 2012, 2012,
end_month	05, 05, 05, 05, 05,
end_day	24, 24, 24, 24, 24,
end_hour	00, 00, 00, 00, 00,
end_minute	00, 00, 00, 00, 00,
end_second	00, 00, 00, 00, 00,
interval_seconds	21600
input_from_file	.true.,.true.,.true.,.true.,.true.,
history_interval	60, 60, 60, 60, 10,
frames_per_outfile	10000, 10000, 10000, 10000, 10000,
restart	.false.,
restart_interval	50000,
io_form_history	2
io_form_restart	2
io_form_input	2
io_form_boundary	2
debug_level	0
iofields_filename	"myoutfields.txt", "myoutfields.txt", "myoutfields.txt", "myoutfields.txt", "myoutfields.txt"
ignore_iofields_warning	.true.,
/	

Table B.3: Namelist.Input for one of the case study: 23rd May 2012, same namelist is used for other case studies.

&domains	
time_step	180,
time_step_fract_num	0,
time_step_fract_den	1,
max_dom	4,
e_we	110, 211, 190, 274, 301,
e_sn	110, 247, 298, 346, 301,
e_vert	51, 51, 51, 51, 51,
p_top_requested	10000,
num_metgrid_levels	38,
num_metgrid_soil_levels	4,
dx	27000, 9000, 3000, 1000, 500,
dy	27000, 9000, 3000, 1000, 500,
grid_id	1, 2, 3, 4, 5,
parent_id	1, 1, 2, 3, 4,
i_parent_start	1, 12, 98, 40, 67,
j_parent_start	1, 12, 80, 90, 95,
parent_grid_ratio	1, 3, 3, 3, 2,
parent_time_step_ratio	1, 3, 3, 6, 3,
feedback	0,
smooth_option	0,
max_ts_level	51,
eta_levels	1.0000, 0.9980, 0.9955, 0.9925, 0.9890, 0.9850,
	0.9805, 0.9755, 0.9700, 0.9640, 0.9575, 0.9505,
	0.9430, 0.9350, 0.9265, 0.9170, 0.9060, 0.8930,
	0.8775, 0.8590, 0.8363, 0.8104, 0.7803, 0.7456,
	0.7059, 0.6615, 0.6126, 0.5594, 0.5041, 0.4479,
	0.3919, 0.3384, 0.2897, 0.2474, 0.2107, 0.1792,
	0.1523, 0.1293, 0.1093, 0.0917, 0.0763, 0.0629,
	0.0513, 0.0413, 0.0328, 0.0255, 0.0194, 0.0144,
	0.0104, 0.0071, 0.0000,
/	

Table B.4: Namelist.Input for one of the case study: 23rd May 2012, same namelist is used for other case studies.

&fdda	
grid_fdda	0, 0, 0, 0, 0,
gfdda_inname	"wrffdda_d<domain>"
gfdda_interval_m	360, 360, 360, 360,
gfdda_end_h	720, 720, 720, 720,
io_form_gfdda	2,
fgdt	0, 0, 0, 0,
if_zfac_uv	1, 1, 1, 1,
if_zfac_t	1, 1, 1, 1,
if_zfac_q	1, 1, 1, 1,
k_zfac_uv	23, 23, 23, 23,
k_zfac_t	23, 23, 23, 23,
k_zfac_q	23, 23, 23, 23,
guv	0.0003, 0.0003, 0.0003, 0.0003,
gt	0.0003, 0.0003, 0.0003, 0.0003,
gq	0.0003, 0.0003, 0.0003, 0.0003,
if_ramping	0,
dtramp_min	60.0,
/	

Table B.6: Namelist.Input for one of the case study: 23rd May 2012, same namelist is used for other case studies.

&physics	
mp_physics	4, 4, 4, 4, 4,
ra_lw_physics	4, 4, 4, 4, 4,
ra_sw_physics	4, 4, 4, 4, 4,
radt	27, 9, 3, 1, 0.5,
sf_sfclay_physics	1, 1, 1, 1, 1,
sf_surface_physics	2, 2, 2, 2, 2,
bl_pbl_physics	1, 1, 1, 1, 0,
bldt	0, 0, 0, 0, 0,
cu_physics	1, 1, 0, 0, 0,
cudt	0, 0, 5, 5, 5,
isfflx	1,
ifsnow	0,
icloud	1,
surface_input_source	1,
num_soil_layers	4,
sf_urban_physics	0,
maxiens	1,
maxens	3,
maxens2	3,
maxens3	16,
ensdim	144,
/	

Table B.5: Namelist.Input for one of the case study: 23rd May 2012, same namelist is used for other case studies.

&dynamics	
w_damping	0,
diff_opt	1, 1, 1, 1, 2,
km_opt	4, 4, 4, 4, 2,
diff_6th_opt	0, 0, 0, 0, 2,
diff_6th_factor	0.12, 0.12, 0.12, 0.12, 0.3,
base_temp	290
damp_opt	0,
zdamp	5000., 5000., 5000., 5000., 5000.,
dampcoef	0.2, 0.2, 0.2, 0.2, 0.2,
khdif	0, 0, 0, 0, 0,
kvdif	0, 0, 0, 0, 0,
non_hydrostatic	.true.,.true.,.true.,.true.,.true.,
moist_adv_opt	1, 1, 1, 1, 1,
scalar_adv_opt	1, 1, 1, 1, 1,

Table B.7: Namelist.Input for one of the case study: 23rd May 2012, same namelist is used for other case studies.

&bdy_control	
spec_bdy_width	5,
spec_zone	1,
relax_zone	4,
specified	.true.,.false.,.false.,.false.,.false.,
nested	.false.,.true.,.true.,.true.,.true.,
/	
&grib2	
/	
&namelist_quilt	
nio_tasks_per_group	0,
nio_groups	1,
/	

Table B.8: Namelist.Input for one of the case study: 23rd May 2012, same namelist is used for other case studies.

B.3. .bts format conversion

Presented below is the script used for converting a wind field into TurbSim format. Note: the code is taken from TurbSim module.

```
fid = fopen( ADFileName , 'w+' );
fwrite(fid, 7, 'int16'); % TurbSim format identifier, INT(2)
fwrite(fid, WindFileStruct.Nz, 'int32'); % the number of grid points vertically, INT(4)
fwrite(fid, WindFileStruct.Ny, 'int32'); % the number of grid points laterally, INT(4)
fwrite(fid, 0, 'int32'); % the number of tower points, INT(4)
fwrite(fid, WindFileStruct.N, 'int32'); % the number of time steps, INT(4)
fwrite(fid, WindFileStruct.dz, 'float32'); % grid spacing in vertical direction, REAL(4), in m
fwrite(fid, WindFileStruct.dy, 'float32'); % grid spacing in lateral direction, REAL(4), in m
fwrite(fid, WindFileStruct.dt, 'float32'); % grid spacing in delta time, REAL(4), in m/s
fwrite(fid, WindFileStruct.U0, 'float32'); % the mean wind speed at hub height, REAL(4), in m/s
fwrite(fid, WindFileStruct.HubHt, 'float32'); % height of the hub, REAL(4), in m
fwrite(fid, WindFileStruct.Zbottom, 'float32'); % height of the bottom of the grid, REAL(4), in m
fwrite(fid, 1000, 'float32'); % the U-component slope for scaling, REAL(4)
fwrite(fid, 0, 'float32'); % the U-component offset for scaling, REAL(4)
fwrite(fid, 1000, 'float32'); % the V-component slope for scaling, REAL(4)
fwrite(fid, 0, 'float32'); % the V-component offset for scaling, REAL(4)
fwrite(fid, 1000, 'float32'); % the W-component slope for scaling, REAL(4)
fwrite(fid, 0, 'float32'); % the W-component offset for scaling, REAL(4)
fwrite(fid, 1, 'int32'); % the number of characters in the description
string, max 200, INT(4)
for ii = 1:1
fwrite(fid, version(ii), 'int8'); % the ASCII integer representation of the character string
end
v = zeros(1,3);
cnt = 0;
for it = 1:WindFileStruct.N %time steps
for iz = 1:WindFileStruct.Nz %grid vertical
for iy = 1:WindFileStruct.Ny %grid horiz
for ii = 1:3 %no.of components
cnt = cnt + 1;
v(ii) = WindFileStruct.WF(it,iy,iz,ii)*1000;
end
fwrite(fid, v, 'int16');
end
end
end
fclose all;
```

B.4. Code validation

Presented in this section is a spectral comparison between code from mathwork [33] and TurbSim - NREL. It is presented in the figure: B.1. The spectra is observed to be similar to TurbSim.

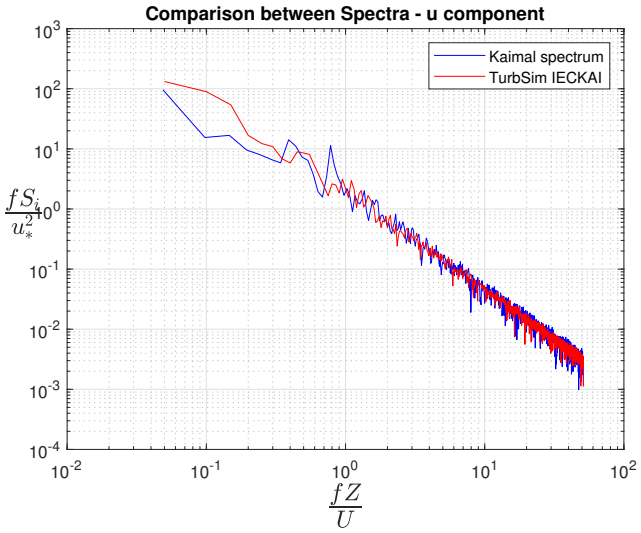

Figure B.1: Spectral comparison between Etienne Cheynet's mathworks code and TurbSim - NREL, using IEC Kaimal spectrum.

B.5. Coefficients for CJR model

Presented here are the coefficients used for modelling the equations: 2.25 and 2.26. Coefficients are provided by the author Etiene Cheynet[13]. Coefficients for u-component of the aforementioned spectral equations.

Equation	Stability	Height (m)	Coefficient					
			a_1^u	b_1^u	a_2^u	b_2^u	c_1^u	a_3^u $(1e-5)$
Equation: 2.25	[-2, -1)	81.5	206	73	4.2	14	-	0
		61.5	188	42	0.5	2	-	0
		41.5	355	57	0.6	2.3	-	0
	[-1, -0.5)	81.5	122	51	1.5	6.8	-	0
		61.5	155	50	0.8	3.8	-	0
		41.5	205	52	0.5	2.5	-	0
	[-0.5, -0.3)	81.5	141	64	1.6	8.9	-	0
		61.5	154	59	0.9	5.6	-	0
		41.5	218	68	0.8	5.2	-	0
	[-0.3, -0.1)	81.5	170	78	2.2	14	-	0
		61.5	175	73	1.4	10	-	0
		41.5	219	79	1.3	9.9	-	0
	[-0.1, 0.1)	81.5	189	111	9.6	40	-	0
		61.5	170	84	7.6	40	-	0
		41.5	195	84	7.5	40	-	0
Equation 2.26	[0.1, 0.3)	81.5	-	-	16	33	0.008	0
		61.5	-	-	18	36	0.006	0.007
		41.5	-	-	19	36	0.004	0.10
	[0.3, 0.5)	81.5	-	-	9.8	14	0.010	0.3
		61.5	-	-	11	13	0.008	0.5
		41.5	-	-	11	13	0.010	0.3
	[0.5, 1)	81.5	-	-	7.6	8.8	0.01	0.8
		61.5	-	-	7.4	7.6	0.02	0.3
		41.5	-	-	7.1	6.4	0.02	0.4
	[1, 2)	81.5	-	-	5	4.4	0.03	1.5
		61.5	-	-	5.8	5.1	0.04	1.5
		41.5	-	-	4	3.9	0.03	0.8

Table B.9: u-component velocity spectrum coefficients, obtained from fitting observations to equation: 2.25 and 2.26

Coefficients for v-component of the aforementioned spectral equations.

Equation	Stability	Height (m)	Coefficient					
			a_1^v	b_1^v	a_2^v	b_2^v	c_1^v	a_3^v $(1e-5)$
Equation: 2.25	[-2, -1)	81.5	374	144	2.8	9.5	-	0
		61.5	413	139	1.3	5.8	-	0
		41.5	337	130	0.7	5	-	0
	[-1, -0.5)	81.5	286	149	1.9	8	-	0
		61.5	221	122	1.1	6.6	-	0
		41.5	253	164	1	8.6	-	0
	[-0.5, -0.3)	81.5	306	185	1.9	8.5	-	0
		61.5	225	156	1	7.1	-	0
		41.5	308	225	0.6	6.2	-	0
	[-0.3, -0.1)	81.5	432	362	3.1	13	-	0
		61.5	351	318	1.9	12	-	0
		41.5	217	252	1	10	-	0
Equation 2.26	[-0.1, 0.1)	81.5	-	-	5.2	12	0.007	0.05
		61.5	-	-	5.8	15	0.007	0
		41.5	-	-	6.7	18	0.006	0
	[0.1, 0.3)	81.5	-	-	4.3	6	0.001	0.3
		61.5	-	-	4.6	6.3	0.001	0.3
		41.5	-	-	4.5	6.2	0	0.2
	[0.3, 0.5)	81.5	-	-	3.2	3.2	0.001	0.9
		61.5	-	-	3.2	2.9	0.001	0.8
		41.5	-	-	3.3	2.8	0.003	0.6
	[0.5, 1)	81.5	-	-	2.8	2.1	0.006	1.3
		61.5	-	-	2.7	1.9	0.01	1
		41.5	-	-	2.6	1.7	0.008	2
	[1, 2)	81.5	-	-	2.1	1.2	0.02	3.3
		61.5	-	-	2.4	1.4	0.03	1.9
		41.5	-	-	1.6	1	0.02	1.6

Table B.10: v-component velocity spectrum coefficients, obtained from fitting observations to equation: 2.25 and 2.26

Coefficients for w-component of the aforementioned spectral equation 2.25. The study found equation: 2.25 to be a better fit for w-component rather than equation: 2.26.

Equation	Stability	Height (m)	Coefficient			
			a_1^w	b_1^w	a_2^w	b_2^w
Equation: 2.25	[-2, -1)	81.5	21	10	0.5	2.3
		61.5	25	9.7	0.5	2.6
		41.5	27	10	0.6	2.4
	[-1, -0.5)	81.5	16	13	0.9	3
		61.5	19	13	0.7	2.6
		41.5	20	15	1	3.1
	[-0.5, -0.3)	81.5	14	18	1	3.3
		61.5	15	17	0.9	3.3
		41.5	14	15	0.8	2.8
	[-0.3, -0.1)	81.5	9.4	22	1.1	3.7
		61.5	10	21	1	3.7
		41.5	11	23	1.1	3.8
	[-0.1, 0.1)	81.5	2.9	16	1.4	3.7
		61.5	3.5	19	1.4	4.2
		41.5	3.1	19	1.5	4.4
	[0.1, 0.3)	81.5	0.03	1.2	1.5	2.6
		61.5	0.004	3.6	1.6	2.7
		41.5	0	0	1.6	2.8
	[0.3, 0.5)	81.5	0	0	1.2	1.4
		61.5	0	0	1.1	1.3
		41.5	0	0	1.1	1.3
	[0.5, 1)	81.5	0.02	0.3	1	1
		61.5	0.01	0.4	0.9	0.9
		41.5	0.05	0.5	0.9	0.9
	[1, 2)	81.5	1.2	18	0.6	0.5
		61.5	0.01	0.09	0.8	0.8
		41.5	0.4	2.2	0.4	0.4

Table B.11: w-component velocity spectrum coefficients, obtained from fitting observations to equation 2.25.

C

Appendix

C.1. WRF contours and hodographs

Presented in this appendix are the results and comparison of WRF with wetterzentrale's[39] re-analysis archives and hodographs for understanding the movement of fluid particles in a low level jet. These results have been used as a preliminary way to identify an LLJ. Further visual investigation observing satellite images is also explored using NASA web view[56].

C.2. Case study 1 - 02-July-2006

For the Case - 2^{nd} July 2006, figure: C.1 presents the comparison of re-analysis archives and WRF simulation.

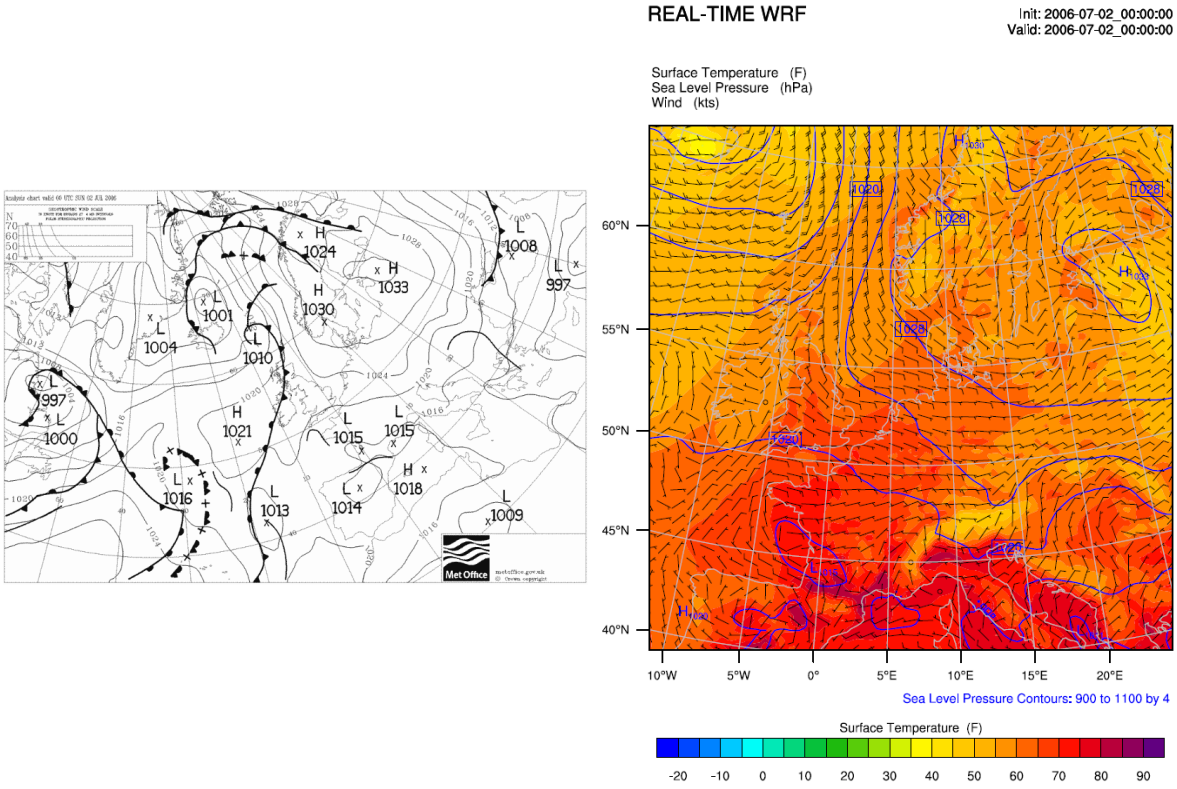

Figure C.1: Comparison of re-analysis archives and simulated WRF for the case 2^{nd} July 2006, starting from the left, re-analysis archives plot, and WRF simulations plots for the same time(right), barbs represent magnitude of wind speeds. Each line on the plot represents isobars with pressure in millibar annotated on the line.

The results are plotted for the hour 00:00 and are found to be similar, indicating a good WRF simulation. The re-analysis archives are limited to the hour 00:00, therefore further investigation with this data-set is not possible. However, from the re-analysis archive plot a warm front from north of United Kingdom is observed to pass over Europe, this could be a possible cause of the low level jet.

A hodograph is a plot used to understand the movement of a fluid particle over time. In order to understand the movement of fluid particles during a low level jet, hodographs are plotted here at near-hub height 100m in figure: C.2. Starting from left, the plot presents the movement of fluid particle through the day on 2^{nd} July 2006, plot on the right presents hodograph of a fluid particle during the identified LLJ. A clear rotation of the fluid particle during the day and during the LLJ is observed. It has been observed in literature that rotation of the fluid can be associated with an LLJ.

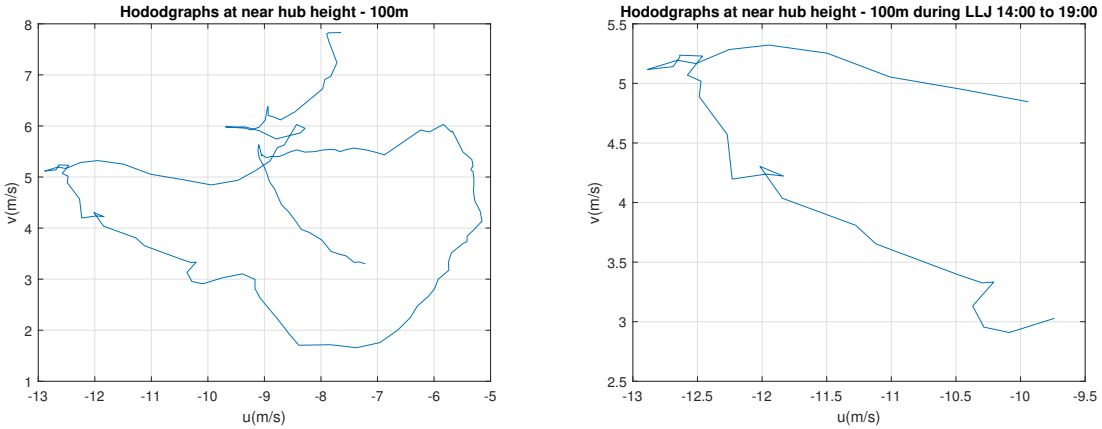

Figure C.2: From left, hodograph at near hub height - 100m for the day and hodograph during low level jet occurring between 14:00 and 19:00.

C.3. Case study 2 - 23-May-2012

For the Case - 23rd May 2012, figure: C.3 presents the comparison of re-analysis archives and WRF simulation.

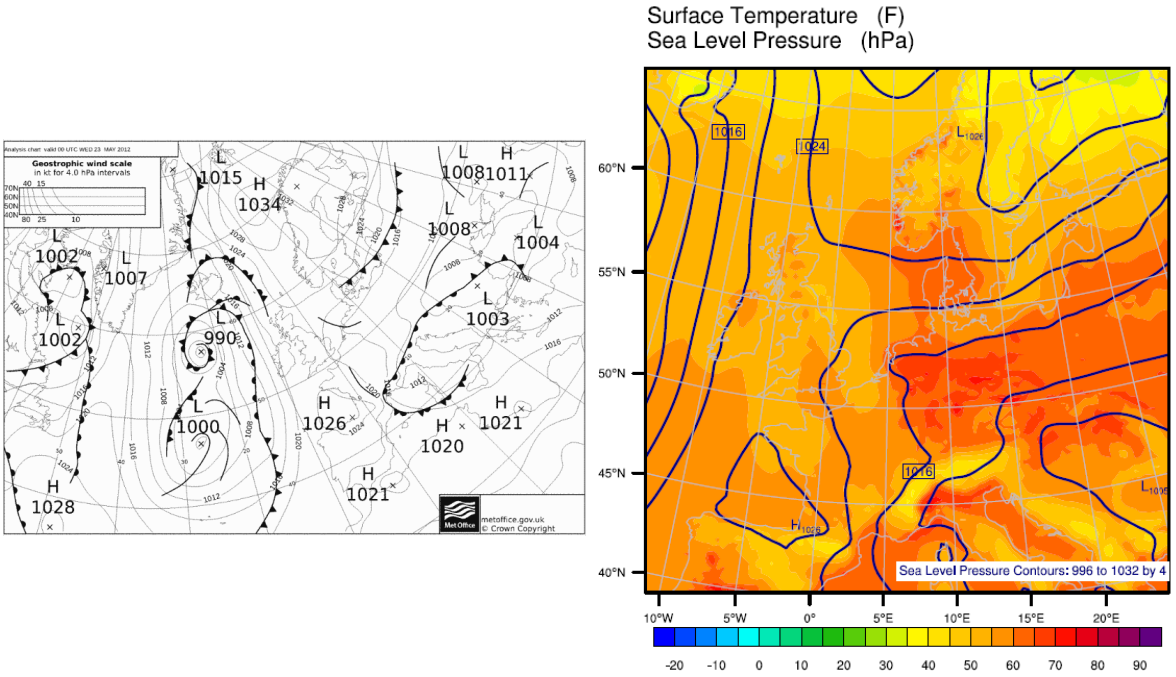

Figure C.3: Comparison of re-analysis archives and simulated WRF for the case 23rd May 2012, starting from the left, re-analysis archives plot, right, WRF simulation for domain 1, barbs represent magnitude of wind speeds. Each line on the plot represents isobars with pressure in millibar annotated on the line. Plots presented are for the same time: 00:00

The results are plotted for the hour 00:00. This case is an interesting phenomena. The re-analysis archives although limited to the hour 00:00, do not show any signs of a low level jet, yet the phenomena is re-created by WRF. Judging from the temperature plotted in figure: C.3 (right) the jet could possibly be a warm front.

To better understand this event, hodographs are plotted. Presented in figure: C.4. Starting from left, the plot presents the movement of fluid particle through the day on 23rd July 2006, plot on the right presents hodograph of a fluid particle during the identified LLJ event. No clear rotation of the fluid particle is observed, although a low level is identified through both data analysis and WRF. Further study into this particular would be quite interesting.

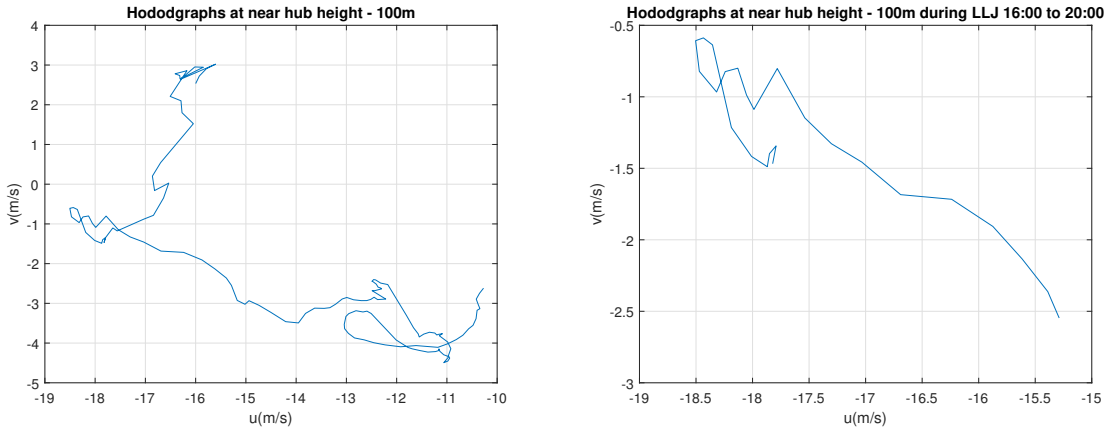

Figure C.4: From left, hodograph at near hub height - 100m for the day and hodograph during low level jet occurring between 16:00 and 20:00.

C.4. Case study 3 - 14-April-2004

For the Case - 14^{th} April 2004, figure: C.5 presents the comparison of re-analysis archives and WRF simulation.

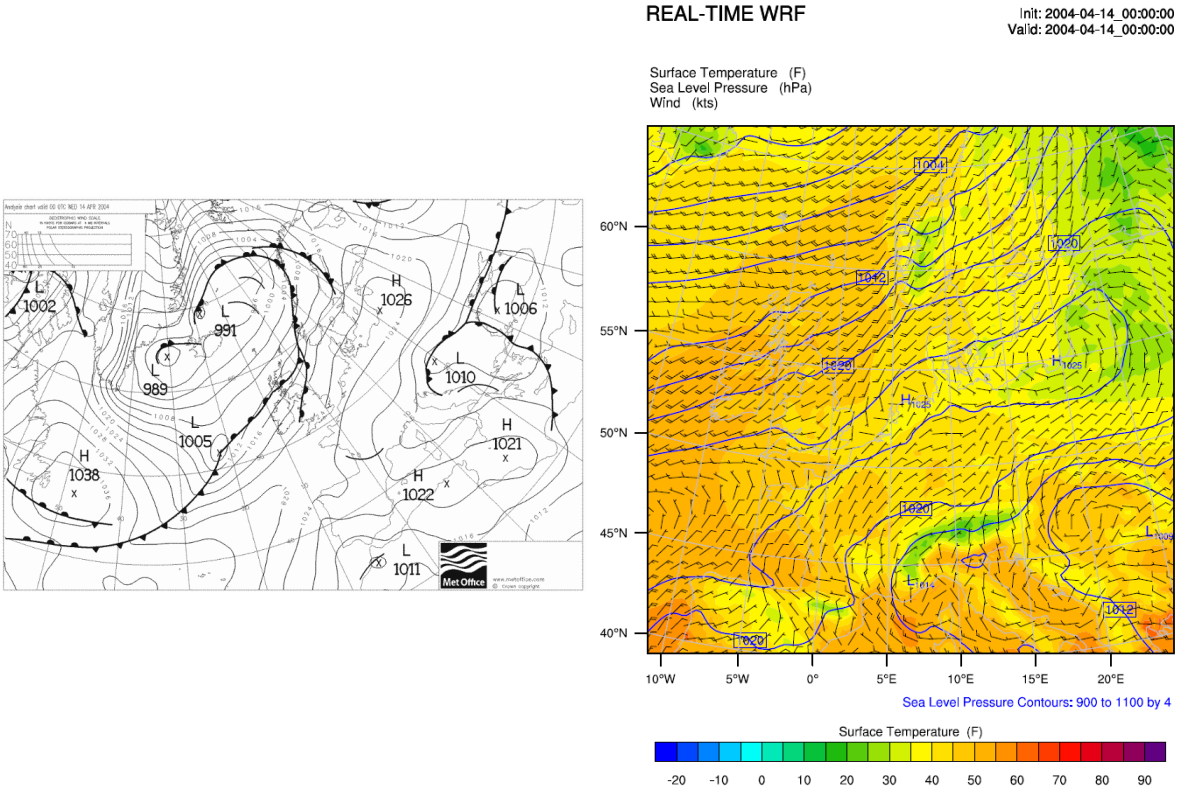

Figure C.5: Comparison of re-analysis archives and simulated WRF for the case 14^{th} April 2004, starting from the left, re-analysis archives plot, right, WRF simulation for domain 1, barbs represent magnitude of wind speeds. Each line on the plot represents isobars with pressure in millibar annotated on the line. Plots presented are for the same time: 00:00

The results are plotted for the hour 00:00. WRF simulates the high pressure region very well with 1mbar difference. We observe a cold front indicated from the re-analysis archive plot in figure: C.5 (left).

To better understand the event, hodographs are plotted. Presented in figure: C.6. Starting from left, the plot presents the movement of fluid particle through the day on 14^{th} April 2004, plot on the right presents hodograph of a fluid particle during the identified LLJ event. A clear rotation of particles during the entire day is observed from the plot on the left, however no clear rotation of the fluid particle is observed during the LLJ event. As data analysis represents an LLJ this case is carried forward for loading analysis.

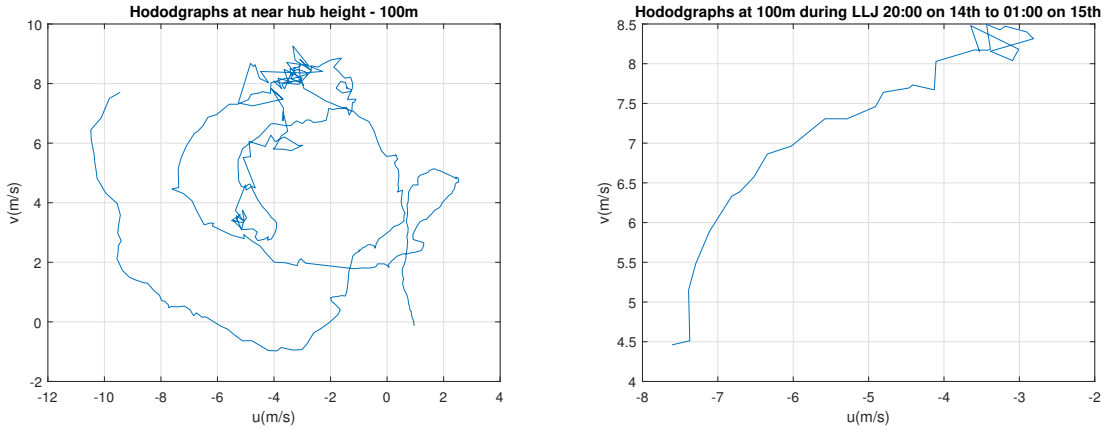

Figure C.6: From left, hodograph at near hub height - 100m for the day and hodograph during low level jet occurring between 20:00 on the 14^{th} and 01:00 on the 15^{th}.

Bibliography

[1] Wind Europe. Offshore wind in europe - key trends and statistics 2018. *Wind Europe*, 2019.

[2] ECN. Cost modelling of floating wind farms. *ECN-E–15- 078*, 2016.

[3] TennT. North sea wind power hub. *Connecting wind energy*, 2017. Available at https://www.tennet.eu/our-key-tasks/innovations/north-sea-wind-power-hub/,.

[4] J C Kaimal, JCJ Wyngaard, Y Izumi, and Coté. Spectral characteristics of surface-layer turbulence. *Quarterly Journal of the Royal Meteorological Society*, 98(417):563–589, 1972.

[5] Theodore Von Karman. Progress in the statistical theory of turbulence. *Proceedings of the National Academy of Sciences of the United States of America*, 34(11):530, 1948.

[6] Jakob Mann. The spatial structure of neutral atmospheric surface-layer turbulence. *Journal of fluid mechanics*, 273:141–168, 1994.

[7] Neil Davis Kelley and Bonnie J Jonkman. Overview of the turbsim stochastic inflow turbulence simulator. Technical report, National Renewable Energy Lab.(NREL), Golden, CO (United States), 2005.

[8] Princeton. Parameterizations of the abl in atmospheric models. *Course-work*, 2011. Available at http://efm.princeton.edu/ABL_Parametrization.htm,.

[9] Ameya Sathe, Jakob Mann, Thanasis Barlas, WAAM Bierbooms, and GJW Van Bussel. Influence of atmospheric stability on wind turbine loads. *Wind Energy*, 16(7):1013–1032, 2013.

[10] Jinkyoo Park, Lance Manuel, and Sukanta Basu. Toward isolation of salient features in stable boundary layer wind fields that influence loads on wind turbines. *Energies*, 8(4):2977–3012, 2015.

[11] Bert Blocken. 50 years of computational wind engineering: past, present and future. *Journal of Wind Engineering and Industrial Aerodynamics*, 129:69–102, 2014.

[12] Jason M Jonkman, Marshall L Buhl Jr, et al. Fast user's guide. *National Renewable Energy Laboratory, Golden, CO, Technical Report No. NREL/EL-500-38230*, 2005.

[13] Etienne Cheynet, Jasna B Jakobsen, and Joachim Reuder. Velocity spectra and coherence estimates in the marine atmospheric boundary layer. *Boundary-layer meteorology*, 169(3):429–460, 2018.

[14] Federal Ministry for Economic Affairs BMWi (Bundesministerium fuer Wirtschaft und Energie, Energy), and project executing organization) the PTJ (Projekttraeger Juelich. Fino-1 research met-mast. *"FINO-1"*, 2002.

[15] International Electrotechnical Commission et al. Wind turbines: Part 3: Design requirements for offshore wind turbines; 2009, 2009.

[16] Jacob Mattingley. Wind field modelling. *National Renewable Energy Laboratory*, 2017. Available at http://www.ict-aeolus.eu/SimWindFarm/model-windfield.html,.

[17] AS Monin and AM Obukhov. Basic laws of turbulent mixing in the surface layer of the atmosphere. *Contrib. Geophys. Inst. Acad. Sci. USSR*, 151(163):e187, 1954.

[18] Jinkyoo Park, S Basu, and L Manuel. Large-eddy simulation of stable boundary layer turbulence and estimation of associated wind turbine loads. *Wind Energy*, 17(3):359–384, 2014.

[19] Ming Xue. Low level jets. *National Renewable Energy Laboratory*, 2009. Available at http://twister.ou.edu/MM2005/Chapter2.3.pdf,.

[20] Peter C Kalverla, Gert-Jan Steeneveld, Reinder J Ronda, and Albert AM Holtslag. An observational climatology of anomalous wind events at offshore meteomast ijmuiden (north sea). *Journal of Wind Engineering and Industrial Aerodynamics*, 165:86–99, 2017.

[21] Alfred K Blackadar. Boundary layer wind maxima and their significance for the growth of nocturnal inversions. *Bulletin of the American Meteorological Society*, 38(5):283–290, 1957.

[22] Jürgen Malcher and Helmut Kraus. Low-level jet phenomena described by an integrated dynamical pbl model. *Boundary-Layer Meteorology*, 27(4):327–343, 1983.

[23] Martin Dörenkämper, Björn Witha, Gerald Steinfeld, Detlev Heinemann, and Martin Kühn. The impact of stable atmospheric boundary layers on wind-turbine wakes within offshore wind farms. *Journal of Wind Engineering and Industrial Aerodynamics*, 144:146–153, 2015.

[24] Anthony J Kettle. Unexpected vertical wind speed profiles in the boundary layer over the southern north sea. *Journal of Wind Engineering and Industrial Aerodynamics*, 134:149–162, 2014.

[25] Alfredo Peña, Sven-Erik Gryning, and Charlotte B Hasager. Measurements and modelling of the wind speed profile in the marine atmospheric boundary layer. *Boundary-layer meteorology*, 129(3):479–495, 2008.

[26] Isaac Van der Hoven. Power spectrum of horizontal wind speed in the frequency range from 0.0007 to 900 cycles per hour. *Journal of meteorology*, 14(2):160–164, 1957.

[27] Eugene Khutoryansky. Fourier transform, fourier series, and frequency spectrum. *"YouTube"*, 2015. Available at https://www.youtube.com/watch?v=r18Gi8lSkfM/,.

[28] Peter Welch. The use of fast fourier transform for the estimation of power spectra: a method based on time averaging over short, modified periodograms. *IEEE Transactions on audio and electroacoustics*, 15 (2):70–73, 1967.

[29] Henry W Tieleman. Universality of velocity spectra. *Journal of Wind Engineering and Industrial Aerodynamics*, 56(1):55–69, 1995.

[30] Jagadish Chandran Kaimal and John J Finnigan. *Atmospheric boundary layer flows: their structure and measurement*. Oxford university press, 1994.

[31] JP Pérez Beaupuits, A Otárola, FT Rantakyrö, RC Rivera, SJE Radford, and LÅ Nyman. Analysis of wind data gathered at chajnantor. *ALMA Memo 497, National Radio Astronomy Observatory*, 2004.

[32] JCj Kaimal. Turbulenece spectra, length scales and structure parameters in the stable surface layer. *Boundary-Layer Meteorology*, 4(1-4):289–309, 1973.

[33] E. Cheynet. Wind field simulation. *Mathworks*, 2019. Available at https://nl.mathworks.com/matlabcentral/fileexchange/68632-wind-field-simulation-the-fast-version,.

[34] Philippe Drobinski, Pierre Carlotti, Jean-Luc Redelsperger, Valery Masson, Robert M Banta, and Rob K Newsom. Numerical and experimental investigation of the neutral atmospheric surface layer. *Journal of the atmospheric sciences*, 64(1):137–156, 2007.

[35] BA Kader and AM Yaglom. Spectra and correlation functions of surface layer atmospheric turbulence in unstable thermal stratification. In *Turbulence and Coherent Structures*, pages 387–412. Springer, 1991.

[36] Thomas Neumann and Klaus Nolopp. Three years operation of far offshore measurements at fino1. *DEWI Mag*, 30:42–46, 2007.

[37] A Westerhellweg, T Neumann, and V Riedel. Fino1 mast correction. *Dewi magazin*, 40:60–66, 2012.

[38] Peter Baas, FC Bosveld, H Klein Baltink, and AAM Holtslag. A climatology of nocturnal low-level jets at cabauw. *Journal of Applied Meteorology and Climatology*, 48(8):1627–1642, 2009.

[39] Wetterzentrale. Wetterzentrale, germany. *Wetterzentrale*, 2019. Available at http://www.wetterzentrale.de/de/reanalysis.php?var=45&map=1&model=bra,.

[40] William C Skamarock, Joseph B Klemp, Jimy Dudhia, David O Gill, Dale M Barker, Michael G Duda, Xiang-Yu Huang, Wei Wang, and Jordan G Powers. A description of the advanced research wrf version 3, ncar technical note. *National Center for Atmospheric Research, Boulder, Colorado, USA*, 2008.

[41] Earth system research and laboratory. Wrf domain wizard for wps and namelist.input. *US Department of Commerce, NOAA research*, 2013. Available at https://esrl.noaa.gov/gsd/wrfportal/DomainWizard.html,.

[42] UCAR. Wrf terrestrial data. *WRF V3 Geographical Static Data Downloads*, 2018. Available at http://www2.mmm.ucar.edu/wrf/users/download/get_sources_wps_geog_V3.html,.

[43] DP Dee, SM Uppala, AJ Simmons, P Berrisford, P Poli, S Kobayashi, U Andrae, MA Balmaseda, G Balsamo, P Bauer, et al. The era-interim reanalysis: configuration and performance of the data assimilation system, qj roy. meteor. soc., 137, 553–597, 2011.

[44] UCAR. Integrated data viewer (idv). *UCAR community programmes*, 2019. Available at https://www.unidata.ucar.edu/software/idv/,.

[45] UCAR. Ncar command language (ncl). *WRF-ARW Online tutorial*, 2019. Available at http://www2.mmm.ucar.edu/wrf/OnLineTutorial/Graphics/NCL/index.php,.

[46] UCAR. Vapor - visualization and analysis platform for ocean, atmosphere, and solar researchers. *UCAR*, 2019. Available at https://www.vapor.ucar.edu/,.

[47] NASA. Panoply - national aeronautics and space administration. *NASA*, 2019. Available at https://www.giss.nasa.gov/tools/panoply/download/,.

[48] WC Skamarock and JB Klemp. Coauthors, 2008: A description of the advanced research wrf version 3. ncar tech. Technical report, Note NCAR/TN-4751STR, 113 pp., doi: 10.5065/D68S4MVH, 2005.

[49] UCAR. Weather, reaserach and forecasting (wrf) compiling steps. *UCAR*, 2018. Available at http://www2.mmm.ucar.edu/wrf/OnLineTutorial/compilation_tutorial.php,.

[50] Earth system research and laboratory. Namelist options for namelist.wps and namelist.input. *US Department of Commerce, NOAA research*, 2018. Available at https://esrl.noaa.gov/gsd/wrfportal/namelist_input_options.html,.

[51] Raj K Rai, Harish Gopalan, and Jonathan W Naughton. Effects of spatial and temporal resolution of the turbulent inflow on wind turbine performance estimation. *Wind Energy*, 19(7):1341–1354, 2016.

[52] Chungwook Sim, Sukanta Basu, and Lance Manuel. On space-time resolution of inflow representations for wind turbine loads analysis. *Energies*, 5(7):2071–2092, 2012.

[53] Jason Jonkman, Sandy Butterfield, Walter Musial, and George Scott. Definition of a 5-mw reference wind turbine for offshore system development. Technical report, National Renewable Energy Lab.(NREL), Golden, CO (United States), 2009.

[54] Bonnie Jonkman and Jason Jonkman. Fast v8 - linux user guide. *National Renewable Energy Laboratory*, 2016. Available at https://wind.nrel.gov/nwtc/docs/README_FAST8.pdf,.

[55] Annette Westerhellweg, Beatriz Cañadillas, Friederike Kinder, and Tom Neumann. Wake measurements at alpha ventus–dependency on stability and turbulence intensity. In *Journal of Physics: Conference Series*. IOP Publishing, 2014.

[56] NASA. Eosdis world view. *NASA*, 2019. Available at https://worldview.earthdata.nasa.gov/?p=geographic&l=VIIRS_SNPP_CorrectedReflectance_TrueColor(hidden),MODIS_Aqua_CorrectedReflectance_TrueColor(hidden),MODIS_Terra_CorrectedReflectance_TrueColor,Reference_Labels(hidden),Reference_Features(hidden),Coastlines&t=2012-05-23-T00%3A00%3A00Z&z=3&v=-7.048805871660591,48.21994407847865,16.96291287833941,59.94455345347865,.